Winds of change: flooding, drying and flow on the Wadden Sea's intertidal flats

An analysis of wind effects based on measurements and simulation results for the area between Ameland and Holwerd

Master Thesis
B.A. Krans

TUDelft

Rijkswaterstaat
Ministerie van Infrastructuur en Waterstaat

Nelen &
Schuurmans

Winds of change: flooding, drying and flow on the Wadden Sea's intertidal flats

An analysis of wind effects based on measurements and simulation results for the area between Ameland and Holwerd

by

B.A. Krans

to obtain the degree of Master of Science

at the Delft University of Technology,

to be defended publicly on Wednesday 16 July, 2025 at 13:00.

Main Supervisor:	B.C. Van Prooijen - TU Delft
Secondary Supervisor:	D.S. van Maren - TU Delft | Deltares
Daily supervisor:	R.J.A. van Weerdenburg - TU Delft | Deltares
Company Supervisor:	J.J. de Vries - Rijkswaterstaat
Company Supervisor:	N.D. Volp - Nelen & Schuurmans | UTwente
Duration:	Nov, 2024 - July, 2025
MSc. Programme:	Civil Engineering, TU Delft

Cover: Wadden Sea intertidal area at Het Rif, taken by Berend Krans in 2022.

TUDelft

Preface

 This document presents my MSc thesis in Civil Engineering, with a specialisation in Hydraulic Engineering. The thesis focuses on wind-driven currents on the intertidal area of the Wadden Sea, specifically between Ameland and Holwerd. The aim of the research is to gain a better understanding of how varying wind conditions influence hydrodynamics and to highlight the associated implications. This thesis is written as part of my MSc graduation at TU Delft, in close collaboration with Rijkswaterstaat and Nelen & Schuurmans. Special thanks go to Roy, Nici, Olof, Jurre and Bram for their valuable feedback and support throughout this research.

B.A. Krans
Delft, July 2025

Summary

The Wadden Sea is a dynamic coastal ecosystem characterised by broad intertidal flats that are exposed at low tide and submerged at high tide. Exposure time is an essential input parameter for ecotope mapping; the classification of ecological zones based on abiotic factors.

While the interplay of wind, tides, and sediment dynamics has been studied, there remains limited understanding of detailed exposure times, areas and flow patterns under varying wind conditions, particularly in shallow intertidal zones of the Wadden Sea.

This study quantifies how variations in wind direction and magnitude affect exposure characteristics and flow patterns on the Pinke Wad, located between Ameland and Holwerd. A 3Di-calibrated subgrid model, which is well suited for very shallow areas, is used to simulate twelve wind scenarios in addition to a base case without wind. The effects on one tidal cycle are analysed.

The scenarios result in different hydrodynamic responses on flooding and drying. Easterlies cause a non-linear increase in mean exposure time, from 3.67 h in the baseline to 5.51 h under an East-9 storm ($\approx$ 23 m s^{-1}). By contrast, westerly and northerly winds shorten exposure almost linearly for the simulated scenarios: the mean exposure time decreased to 0.95 h (North-9) and 0.77 h (West-9), with exposed area decreasing by 70–82%. A northerly wind of 6 Beaufort decreased exposure on higher flats by up to 49% ($\sim$6 h), whereas an easterly of the same force increased it by 20% (2.5 h). Residual currents responded accordingly, easterly winds reversed the net flow westward from Beaufort 3 onwards. Westerly winds generated the strongest eastward residual currents. Northerly winds also induced westward flow starting from Beaufort 3, though with smaller directional shifts. Wind-driven changes in exposure time and changing flow patterns have clear implications for ecotope mapping, because there is a large variability over time.

The results highlight the substantial and spatially important role of wind in changing hydrodynamics on the Wadden Sea's intertidal flats. By linking variations in wind speed and direction to changes in residual flow and exposure patterns, the findings provide a better understanding of hydrodynamic-ecological interactions. The use of a (well-calibrated) hydrodynamic subgrid model may offer a promising way forward for calculating exposure times as input for ecotope mapping compared to the current method, which relies on interpolation on water levels between gauge stations.

Contents

Nomenclature

Abbreviation & Index

Abbreviation	Definition
3Di	Subgrid hydrodynamic modelling software by Nelen & Schuurmans
AF	Amplification factor
AQD	Aquadopp Profiler (acoustic current-meter)
Bathymetry	Topography of the seabed
Bft	Beaufort wind-force scale
DEM	Digital Elevation Map
DCSM	Dutch Continental Shelf Model
ECMWF	European Centre for Medium-Range Weather Forecasts
ERA5	ECMWF Reanalysis version 5
Gauge station	Water-level measuring station
HW slack	High-water slack (slack tide at high water)
KNMI	Koninklijk Nederlands Meteorologisch Instituut (Royal Netherlands Meteorological Institute)
KRW	Kaderrichtlijn Water
LiDAR	Light Detection and Ranging
LW, HW	Low water, High water
MSL	Mean Sea Level
NAP	Normaal Amsterdams Peil (Dutch ordnance datum)
RWS	Rijkswaterstaat
RMSE	Root Mean Square Error
Set-up	increase of water level
Set-down	decrease of water level
Spin-up effect	Numerical wiggles produced by a model due to mismatch between initial and boundary conditions
TR	Tidal range
WL	Water level

<div style="text-align: right">

1

</div>

<div style="text-align: right">

Introduction

</div>

1.1. World Heritage Wadden Sea

The Wadden Sea (Figure 1.1a), designated a UNESCO World Heritage Site in 2009, is the largest contiguous wetland on Earth, spanning approximately 10,000 km² and supporting over 10,000 species of flora and fauna, including millions of migratory birds annually (Reise et al., 2010; "UNESCO", 2009; "Waddenvereniging", n.d.). Its intertidal zones are part of extensive mudflats (Figure 1.1b) and sandflats, which sustain rich benthic and microbial communities, providing vital food sources for migratory birds and making the region an important ecological hotspot (Heip et al., 1995; Horn et al., 2020; Laursen et al., 2024). These flats deliver critical ecosystem services, such as coastal protection, nutrient cycling and water quality improvement (Hope et al., 2020; Horn et al., 2020).

(a) Overview of the Dutch, German, and Danish Wadden Sea (Ricklefs et al., 2022).

(b) Aerial photograph of the Wadden Sea's mud flats (Waddenvereniging, 2022).
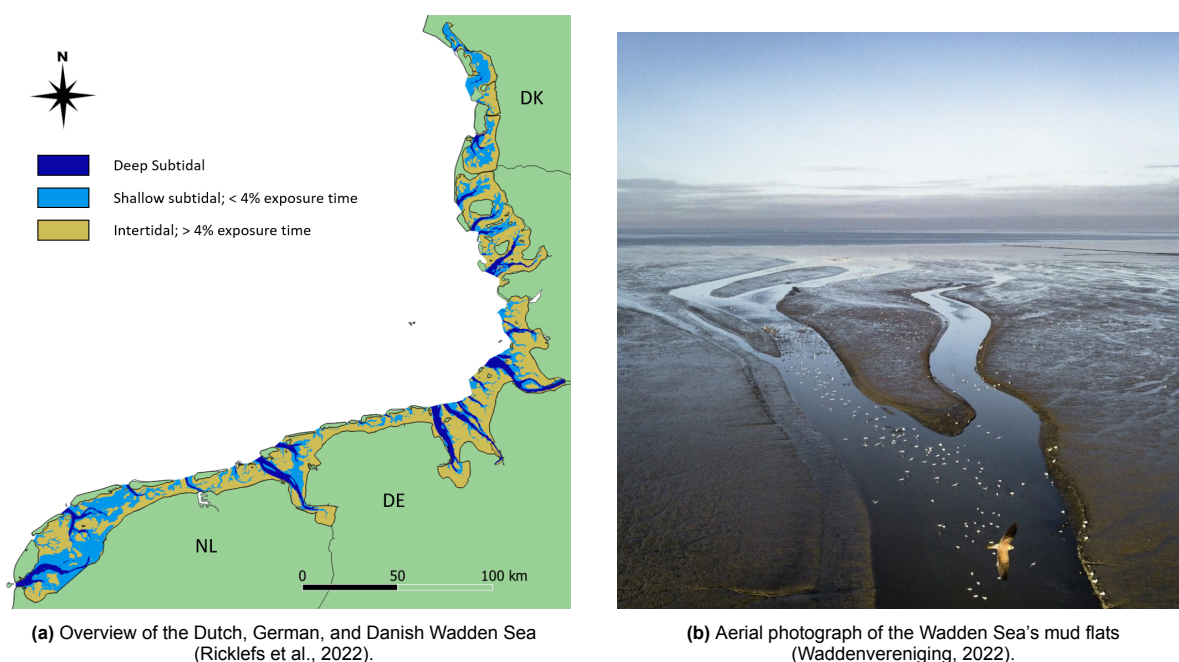
Figure 1.1: Map and aerial photograph of the Wadden Sea.

A way to quantify and visualise the ecological value of the Wadden Sea is through ecotope mapping. Ecotope mapping is a method used to spatially classify and visualise different landscape units within brackish and saltwater environments based on key abiotic (non-living) environmental factors. These ecotopes represent areas that are likely to support distinct ecological communities (Baptist et al., 2019;

<div style="text-align: center">

1

</div>

Paree et al., 2017). The resulting maps serve as tools for environmental monitoring, habitat assessment, policy reporting, and management decisions regarding ecosystems like the Wadden Sea (Paree et al., 2017). The main abiotic parameters considered in ecotope mapping are bed elevation, exposure time (as derived from water levels), maximum flow velocity, bottom wave-orbital-velocity during representative conditions, mean annual high-water salinity, and salinity variability at high water. Since these variables are governed by physical processes, ecotope mapping is directly related to the hydrodynamics.

Hydrodynamics in the Wadden Sea include the combined effects of tides, waves, and wind-driven currents. These processes determine water levels and, therefore, the duration for which intertidal flats are exposed (Duran-Matute et al., 2014; Wang et al., 2012). Annual fluctuations in water level along the Dutch Wadden Sea have been driven largely by storm-induced wind set-up and set-down, making wind and storm statistics a key source of interannual variability at the coast (Deltares, n.d.). Models have suggested that future westerly storms may become more frequent, increasing the likelihood of extreme water levels (Sterl et al., 2015). Even if storms do not intensify, a higher mean water level alone is likely to enlarge surge impacts, especially in areas where flats and marshes cannot accrete quickly enough to keep pace with sea level rise, potentially leading to "drowning" of intertidal flats (Oost et al., 2017; Van Goor et al., 2003).

Exposure time, a key variable in the current ecotope mapping method, is currently estimated using the tool InterTides, which linearly interpolates water levels between gauge stations (Van Weerdernburg R & Hanssen J, 2023). InterTides ignores local bed elevation and small-scale wind effects, and assumes that each basin behaves as a simple interpolation between gauges (van Weerdenburg, 2021). In reality, the tidal wave travels along the coast and basins fill and empty mainly through their inlets (Nauw et al., 2017). The interpolation approach can therefore misrepresent exposure on individual flats.

Recent studies have shown how strongly wind can alter local currents and water levels. Field and modelling work has demonstrated that wind can distort or even reverse tidal currents on shallow flats (Colosimo et al., 2020; Duran-Matute et al., 2014). A numerical study that applied a steady wind of 15 m/s has revealed marked changes in flow speed, basin exchange, and exposure time, driven by depth-dependent wind shear (Boorsma, 2024). This highlights the important role of wind in modifying water levels and flow velocities.

1.2. Research problem

Various aspects of wind-driven currents in coastal environments have been investigated (Boorsma, 2024; Colosimo et al., 2023; Duran-Matute et al., 2014). Most of these studies, such as Boorsma (2024), have primarily focused on storm events. However, the effects of wind conditions that vary in both direction and magnitude are poorly understood. Wind can have significant influence on exposure times and flow patterns, which are directly correlated to ecological conditions. While field measurements are crucial, they are spatially sparse and cannot fully resolve basin-scale dynamics across the complex, shallow, and topographically variable intertidal flats of the Wadden Sea. Hydrodynamic modelling is therefore necessary for spatially continuous, process-based simulation of water levels and currents for different wind scenarios, particularly where direct measurements are unavailable.

Traditional process-based hydrodynamic models such as Delft3D or D-Flow Flexible Mesh represent each computational element with a single elevation value, requiring grid refinement to capture small-scale bathymetric features like tidal creeks or local levees. This leads to increased computational cost and tighter time-step constraints (Volp et al., 2013). Moreover, flooding and drying processes in these models rely on empirical thresholds, which can introduce mass-balance errors and numerical instability (Casulli, 2009; Deltares, 2024). Sub-grid modelling techniques, by contrast, allow high-resolution bathymetry and roughness to be embedded in coarser computational grids, using pre-calculated volume-elevation relationships and semi-implicit solvers that inherently conserve mass and guarantee positive water depths without requiring dry-cell thresholds (Casulli, 2009; Stelling, 2022). These methods are not only more stable and accurate under dynamic flooding conditions, but also significantly faster enabling large-scale, high-resolution simulations of intertidal flats where flow patterns and exposure times are highly sensitive to wind variability (Stelling, 2022; Volp et al., 2013).

1.3. Research aim and questions

This research addresses the need for a model that captures the spatial and temporal variability of wind effects on flooding and drying in the Wadden Sea. It aims to quantify these dynamics using a 2D depth-averaged sub-grid model under varying wind magnitudes and directions. The research objective can be formulated through the following main question and three sub-questions:

How do varying wind conditions influence the hydrodynamics on the intertidal flats in the Wadden Sea?

1. Which hydrodynamic parameters are essential for calibrating and validating a hydrodynamic model?
2. To what extent are flow patterns, exposure times and areas significantly affected by variations in wind speed and direction spatially and temporally?
3. What are the implications of varying wind conditions in terms of ecotope mapping?

To answer these questions, the following steps are taken:

- Calibrate and validate a subgrid hydrodynamic model on measurements on the intertidal area, to adequately model temporal and spatial variability between Ameland and Holwerd, different from the measurement locations.
- Quantify the effects of varying wind direction and magnitude on intertidal exposure durations, exposure areas, and flow patterns in the Wadden Sea, as influenced by varying wind conditions.

1.4. Research method

In this research, we focus on a specific area of the Wadden Sea: the intertidal flat between Ameland and Holwerd. This specific area was selected because measurement data from this region are used to calibrate the model and to analyse hydrodynamics at the basin scale. For this research, the 3Di hydrodynamic model has been chosen, because it is well-suited to deal with the flooding and drying of very shallow areas, because it uses a subgrid modelling technique. This method enables the integration of higher-resolution data while performing hydrodynamic calculations on a coarser computational grid, in combination with a solver that deals with flooding and drying automatically. While models like Delft3D are well established, exploring a less commonly used alternative such as 3Di may offer advantages for computing fine-scale exposure dynamics, using less computational time. It should be noted that this study does not include a direct comparison between 3Di and other modelling software.

Prior to applying the model, measurement data collected by Aquadopp Profiler instruments (AQDs) on the intertidal flats during the winter of 2023 (21 November to 19 December) have been analysed. This period is referred to in this thesis as the research period. The analysis focuses on identifying key hydrodynamic characteristics and highlighting data gaps that the model could help address. These measurements are used to answer sub-question 1.

In addition, an existing 3Di model of the Wadden Sea is used. This model is calibrated and validated using the above-mentioned measurements in combination with water level measurements from Rijkswaterstaat gauge stations. Calibration and validation are based on six performance criteria: the differences in absolute water level, low water levels, high water levels, tidal range, ebb duration, and flood duration.

The model is first calibrated using different grid refinements, followed by adjustments to bottom roughness under still wind conditions. Subsequently, the wind drag coefficient is calibrated for both near-calm and strong wind conditions. Validation is carried out using a period with intermediate wind speeds from a different direction than that of the strong wind period.

Once validated, the model is used to simulate a base case scenario without wind, as well as twelve different wind scenarios. For each scenario, exposure times, exposed areas, and water levels in the intertidal zone are analysed to assess the influence of wind, thereby addressing sub-question 2. The outcomes of this analysis also contribute to answering sub-question 3, as ecotope mapping is influenced by exposure times and flow velocities.

1.5. Research structure

This MSc. thesis document starts with an introduction providing the research context and its relevance, research problem, research questions, and method. Chapter 2 describes the study area, with emphasis on hydrodynamic and meteorological processes relevant to the Wadden Sea and the AQD measurement locations. It also explains how local water levels deviate. Chapter 3 contains an analysis of wind speeds and water level deviations at Nes and the AQD locations for certain wind speeds. Chapter 4 contains background information on the model, its setup and considerations, and the calibration and validation of the model. It also discusses the applied wind scenarios. Chapter 5 describes the results relating to exposure times, exposure areas and flow patterns. Chapter 6 discusses and evaluates the data analysis and model considerations. It also highlights the most notable results. Chapter 7 draws conclusions, and Chapter 8 concludes with recommendations.

Chapter	Content
Chapter 1: Introduction	Provides the research context and its relevance, the research problem, research questions, and method.
Chapter 2: Study area	Describes the study area and explains hydrodynamic and meteorological processes relevant to the Wadden Sea and the AQD measurement locations.
Chapter 3: Wind and water level analysis	Analyses wind speeds and water level deviations at Nes and the AQD locations for selected wind conditions.
Chapter 4: Model description	Provides background on the model, including model configuration, calibration, validation, and applied wind scenarios.
Chapter 5: Results	Presents results on exposure times, exposed areas, and flow patterns.
Chapter 6: Discussion	Discusses and evaluates the data analysis, model considerations, and highlights key findings.
Chapter 7: Conclusions	Draws overall conclusions based on the research.
Chapter 8: Recommendations	Provides recommendations for future work and practical applications.

2

Study area

2.1. Wadden Sea

The Wadden Sea (Figure 2.1) is a complex inlet system connected to the North Sea, with elements such as barrier islands, tidal inlets, intertidal flats (Figure 2.2), salt marshes, and ebb-tidal and flood-tidal deltas (Bosboom & Stive, 2023). Tidal inlets, the water passages between barrier islands, are essential to sediment transport and hydrodynamic processes in this coastal environment. These inlets facilitate the exchange of water, sediments, and nutrients between the open ocean and the back-barrier estuaries or lagoons. The ebb and flood tidal phases drive this exchange, significantly influencing inlet morphology, sediment deposition, and erosion patterns. During flood tides, water and sediments are transported landward, while ebb tides primarily export sediments seaward, creating dynamic equilibrium conditions. These processes are critical for maintaining the stability and ecological function of tidal inlets and associated barrier systems.

Figure 2.1: The Wadden Sea with its bathymetry.

Intertidal flats, are expansive, low-lying areas of sediment. They are exposed during low tide and submerged during high tide, forming a dynamic interface between marine and terrestrial environments. These flats are primarily composed of sand, silt, and clay, with their sedimentary characteristics shaped by tidal currents, wave action, and sediment supply. Intertidal flats serve as important habitats for a wide range of organisms, including benthic invertebrates (Figure 2.3a), microphytobenthos, and migratory birds (Figure 2.3b), forming the foundation of complex food webs (Reise et al., 2010).

(a) Intertidal area around Ameland ("Waddenvereniging", n.d.).

(b) German Wadden island Neuwerk and the surrounding intertidal flats (Ralf Roletschek, Wikipedia under CC BY-SA 3.0).

Figure 2.2: Photographs of intertidal flats near Ameland and Neuwerk.

The alternating cycles of drying and flooding on these flats govern key ecological processes such as nutrient cycling, primary production, and sediment stabilisation, making them hotspots of biological activity (Christianen et al., 2017). Their geomorphology is highly sensitive to environmental changes, such as sea-level rise and human interventions, which can alter tidal regimes and sediment dynamics, potentially threatening their ecological functions (Wang et al., 2012). Intertidal flats are vital ecosystems due to their combined ecological and geomorphological significance, providing services like coastal protection, carbon sequestration, and supporting biodiversity (Chen & Lee, 2022).

(a) Examples of invertebrates. Top left: polychaete worm, top right: blue mussel (Mytilus edulis), bottom left: common cockle (Cerastoderma edule), bottom right: common shore crab (Carcinus maenas).

(b) Migratory birds (Postma, 2025).

Figure 2.3: Invertebrates and migratory birds at the Wadden Sea.

2.2. Hydrodynamic processes

2.2.1. Tides

Tides are periodic fluctuations in sea level caused by the gravitational forces of the Moon and the Sun, as well as the Earth's rotation. The primary driver of tides is the Moon's gravitational pull, which creates two bulges on opposite sides of the Earth, one due to gravitational attraction and the other due to centrifugal forces from the Earth–Moon system's motion (French, 2008). The Sun also exerts a gravitational force that influences tidal amplitudes, leading to spring tides (higher high tides and lower low tides) when the Sun and Moon are aligned, and neap tides (reduced tidal range) when they are at right angles relative to the Earth (Yin et al., 2016).

Tidal movements are the primary drivers of water flow in intertidal zones, causing regular flooding and exposure of these areas. Tidal asymmetry, characterised by differences in the duration and intensity of

ebb and flood tides, significantly affects sediment transport and deposition. This asymmetry can lead to net sediment transport in a particular direction, influencing the morphology of intertidal flats. Friedrichs and Aubrey (1988) discuss how tidal asymmetries contribute to sediment dynamics in shallow estuarine environments.

Tides can be classified into three main types based on their periodicity: diurnal tides, where only one high and one low tide occur per day; semidiurnal tides, characterised by two nearly equal high and low tides each day; and mixed tides, which exhibit significant differences in height between successive high and low tides. These variations give rise to daily inequality, a phenomenon where two successive high tides or low tides within a day differ in magnitude due to the Moon's declination relative to Earth's equatorial plane (Bosboom & Stive, 2023).

Tidal asymmetry results from nonlinear interactions among tidal constituents, driven mainly by nonlinear terms in hydrodynamic equations, including advection and bottom friction. These processes deform tidal waves as they propagate through shallow and constricted areas, generating overtides such as M_4 and M_6. This deformation creates differences in the duration and intensity of flood versus ebb tides, significantly affecting sediment transport and shaping estuarine morphology. In shallow coastal basins, tidal asymmetry may lead either to ebb-dominance, characterised by stronger ebb currents that promote sediment export, or flood-dominance, which enhances sediment deposition and estuarine infilling (Nidzieko & Ralston, 2012). Shallow-water harmonics like the M_4 constituent amplify tidal asymmetry by altering the phase relationships and timing within tidal cycles (Gong et al., 2016).

The combination of tidal asymmetry and daily inequality plays a crucial role in sediment dynamics and coastal morphology. For example, in mixed tidal regimes, diurnal inequality affects sediment resuspension and transport, influencing the evolution of tidal flats and estuarine channels over time (Lu et al., 2015). Understanding these processes is essential for predicting changes in coastal landscapes, designing flood defence systems, and managing sedimentation in navigational channels.

2.2.2. Wind

Wind generates surface stress on the water, creating wind-driven flows that can dominate in shallow intertidal areas where tidal velocities are relatively low. Studies have shown that wind-induced flows can override tidal flows, particularly during low tidal velocities, and even reverse flow directions (Colosimo et al., 2020). De Vet (2020) highlight how wind stress can create substantial cross-shore and alongshore currents, particularly during storm conditions, significantly influencing sediment resuspension and redistribution. This mechanism is most evident when wind is aligned with or opposes tidal currents, amplifying or diminishing their effects, respectively.

The impact of wind is further modulated by local bathymetry and geomorphology. Research by de Vet et al. (2018), van Weerdenburg et al. (2021), and Colosimo et al. (2020) emphasizes that shallow areas with intricate channels, such as those in the Wadden Sea, exhibit pronounced sensitivity to wind forcing. In these regions, even moderate winds can cause localised flow accelerations or reversals, leading to highly variable sediment transport pathways. Beyond these localised effects, wind also plays a crucial role in shaping residual circulation across entire tidal basins. Duran-Matute et al. (2016) demonstrate that prevailing winds can drive net water transport through the Wadden Sea's multiple-inlet system, potentially opposing or enhancing tidal flows. Similarly, van Weerdenburg et al. (2021) show that wind-driven exchange flows across tidal divides can generate compensating flows through main inlet channels, thereby exerting a strong influence on sediment exchange between basins and the open sea.

A specific manifestation of wind's influence on basin-scale hydrodynamics is wind set-up and set-down, which are hydrostatic responses to persistent surface wind stress in shallow, semi-enclosed water bodies. Classical theory shows that the resulting free-surface slope ($\Delta\eta/\Delta x$) is inversely proportional to water depth and directly proportional to the square of the wind speed and the effective fetch (Bosboom & Stive, 2023). Wind set-up refers to the rise in mean water level at the coast when onshore winds push surface waters landward. This leads to a pile-up of water, held in equilibrium by a barotropic pressure gradient that balances the wind stress ($\rho g h \frac{d\eta}{dx} \approx \tau_{\text{wind}}$). Conversely, when offshore winds prevail, surface waters are driven seaward, lowering the water level, a process known as set-down.

Colosimo et al. (2023) demonstrated that basin-scale wind-driven water level set-down significantly

influences the accretion of intertidal flats. Specifically, water level set-down prolongs the aerial exposure period, allowing the sediment bed to consolidate further, potentially resulting in over-consolidation. This process enhances shear strength, reducing susceptibility to erosion. This study found that eastern wind-induced set-down generally increased both the total exposure duration and exposed area within the studied domain. This suggests that easterly winds may lead to over-consolidation.

2.2.3. Ecology

The ecological functioning of the Wadden Sea is characterised by its hydrodynamics, which control the alternation of drying (exposure) and flooding (submergence) on the intertidal flats. Exposure triggers sediment desiccation, oxidation and consolidation, creating sharp gradients in moisture, salinity and oxygen that shape benthic habitats (Jansen et al., 2009; Wang et al., 2012). During inundation, tidal and wind-driven currents resuspend fine particles, import nutrients, and stimulate primary production by microphytobenthos (benthic microalgae), thereby fuelling benthic food webs that sustain fish and millions of migratory shorebirds (Christianen et al., 2017; Laursen et al., 2024).

To support habitat mapping into habitat units, Rijkswaterstaat produces an annual *zoute ecotopenkaart*. The latest methodology (2023) overlays six high-resolution base layers to delineate ecotopes within the Dutch Wadden Sea (Rijkswaterstaat, 2023a):

- **Bed elevation**: 20 m × 20 m raster from single-beam soundings and LiDAR;
- **Drying duration (DVD)** using the InterTides model;
- **Mean low-water surface (GLW)** to distinguish deep and shallow sublittoral;
- **Geomorphology** interpreted from 2023 orthophotos and sediment surveys;
- **Hydrodynamics**: 99th-percentile depth-averaged velocities from a 100 m Delft3D-FM cut-out of DCSM-FM, and bottom orbital velocities from the SWAN-Kuststrook wave model;
- **Salinity** and its standard deviation from a 3-D Delft3D-FM run, further refined using vegetation data (VEGWAD).

Ecotopes are classified hierarchically according to the Zoute Ecotopen Stelsel (ZES.1) (Paree et al., 2017). For intertidal flats, the exposure-duration layer first distinguishes the "littoral" (intertidal) from the "sublittoral" zone. The littoral is then subdivided into four zones based on the fraction of time a location is exposed (Table 2.1). Within the sublittoral, dynamic classes are differentiated based on hydrodynamic energy using combined thresholds in maximum flow velocity (V_{MAX}) and wave-orbital velocity (U_{BOT}). The 2023 revision further introduces a middle-dynamic class for the sublittoral (next to low- and high-dynamic), refines sediment-based subclasses (e.g., coarse-sand units), and expands marsh zones with new freshwater categories such as "Zoet kwelder/schor" and "Zoet pionier" (Rijkswaterstaat, 2023a). Figure 2.4 represents an example of an ecotope map of the Ameland Inlet.

Table 2.1: Drying-duration classes for the littoral zone (Rijkswaterstaat, 2023a)

| Exposure duration fraction (%)	Littoral class
4–25	Low littoral
25–40	Mid littoral
40–85	High littoral
85–100	Supralittoral
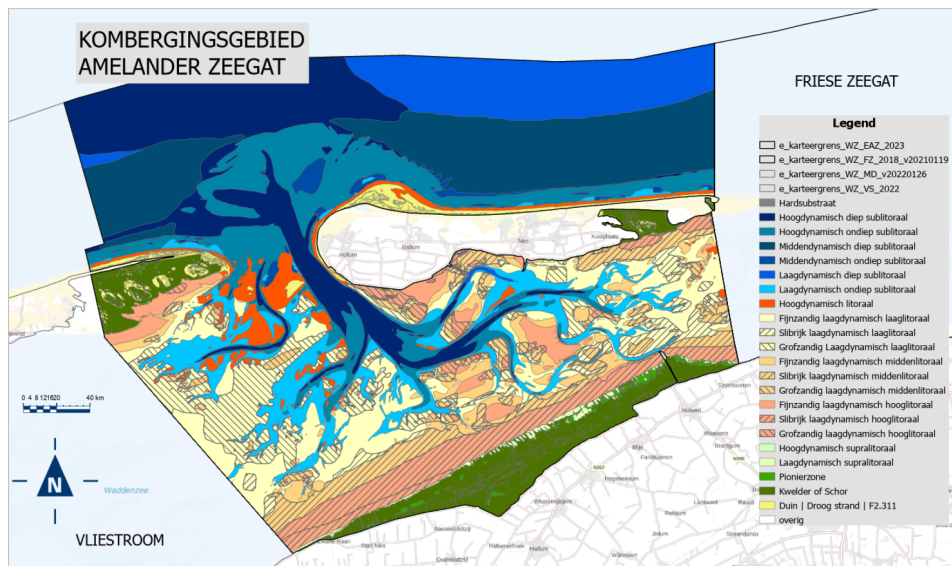
Figure 2.4: Ecotope map of Ameland Inlet 2023 (Rijkswaterstaat, 2023a).

Beyond classification, the ecological implications of these drying and flooding dynamics extend to productivity and connectivity in the Wadden Sea ecosystem. Tidal and wind-driven processes promote nutrient exchange between sediments and the water column, fuelling benthic primary production that supports invertebrates, fish, and migratory birds (Christianen et al., 2017). The predictability of tidal exposure is especially important for foraging birds that rely on benthic prey during low tides (Reise et al., 2010).

2.3. Ameland Basin

This study focuses on the Ameland Basin and a small part of the Pinkegat Basin. Water spreads across intertidal flats and shallow channels before encountering the tidal divide. This divide marks a boundary with minimal water exchange, delineating the influence of different tidal systems. Measurements are conducted in the intertidal areas of Pinkewad and Holwerd, which are part of this complex system and form the focus of this research. The measurement locations, depicted in Figure 2.5 are selected to span both sides of the tidal divide to monitor currents and water levels. These dynamic hydrodynamic characteristics offer valuable insights drawn from the measurement data.
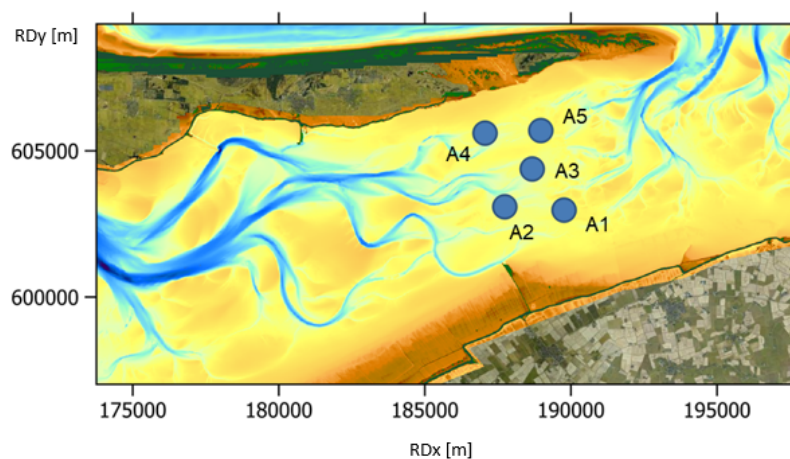

Figure 2.5: Overview of the study area. Measurement locations in blue around the tidal divide, with Ameland located north of these sites.

The astronomical tide at Nes, depicted in Figure 2.6, is the water level of the tidal signal, without meteorological influences. The tidal wave that influences this region originates in the Southern Ocean near 65°S. While it reaches northern locations such as Scotland in under a day, the situation changes significantly as the tide enters the shallow North Sea. Here, the tidal wave slows considerably, and as a consequence, the spring and neap tides (indicated with red and blue arrows in Figure 2.6) at Nes occur approximately two days after the corresponding lunar configurations (Bosboom & Stive, 2023). This delay is due to both the long travel distance and the reduced propagation speed caused by friction in shallow waters.
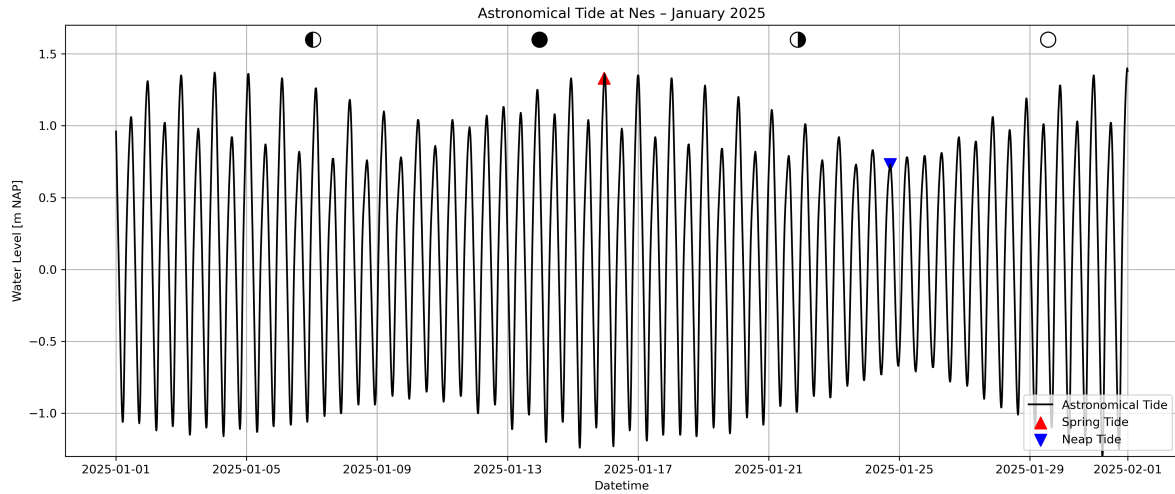

Figure 2.6: Astronomical tide at Nes in January 2025 spring tide approximately 2 days after new/full moon. Data from https://waterinfo.rws.nl.

In addition to the astronomical tide, the measured water levels at Nes reveal that local hydrodynamic effects, such as wind forcing and pressure variations, can significantly modify the expected tidal signal (French, 2008). Figure 2.7 shows both the astronomical and measured water levels, while Figure 2.8 visualises their difference, along with average daily wind speed and direction. From this figures follows that wind can have a substantial influence on water levels. For example, between 23 and 25 November, a pronounced wind set-up occurs during periods of westerly and north-westerly winds.
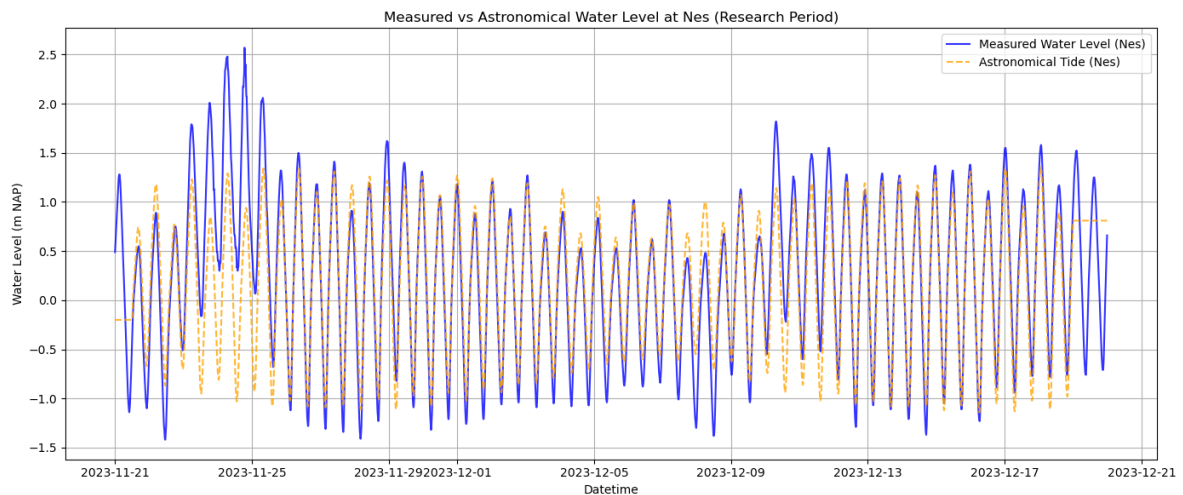
Figure 2.7: Measured water level (blue) and astronomical tide (yellow) at Nes during the research period.
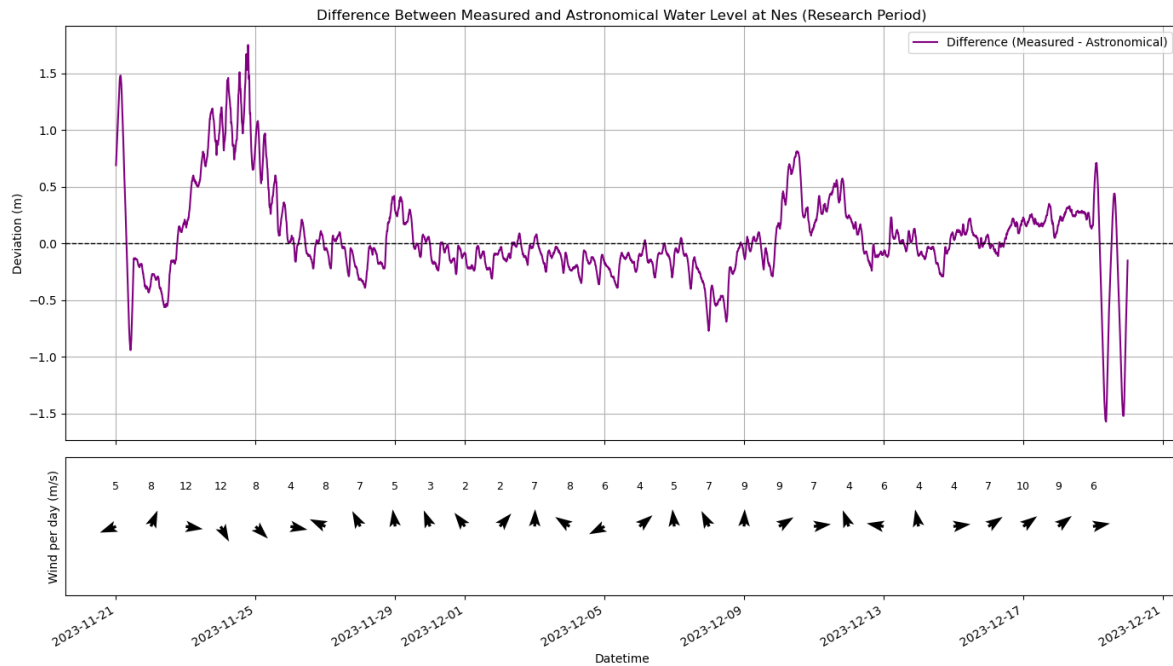
Figure 2.8: Difference between measured and astronomical water level at Nes during the research period, with wind directions (arrows) and speeds (m/s) averaged per day.

2.3.1. Flow on the intertidal flats

The intertidal flats between Ameland and Holwerd are primarily influenced by tidal flows from two main tidal inlets: the Frisian Inlet to the east and the Ameland Inlet to the west.

These inlets create complex hydrodynamics characterised by reversing tidal currents and varying flow directions. Tidal flow mainly passes through well-defined tidal channels, including the artificially maintained ferry route between Holwerd and Ameland (van Rijn, 2017). Peak tidal currents in these channels often reach velocities around 1 m/s during spring tides (van Rijn, 2017). In contrast, flow velocities decrease substantially over the adjacent extensive mudflats, particularly near the tidal divide on Pinkewad. This reduction promotes sediment deposition and supports the maintenance of the intertidal morphology (Pearson, 2022).

Numerical modelling studies reveal persistent residual circulation patterns that are strongly influenced by wind. For example, strong south-westerly winds generate eastward residual flows across Pinkewad, balanced by ebb-directed currents exiting through the Ameland Inlet (Duran-Matute et al., 2014; van Weerdenburg et al., 2021).

Furthermore, the flooding and drying process at the AQD measurement locations is observed. Location A1 typically fills via the Ameland Inlet but also occasionally receives inflow from the Frisian Inlet. Drainage occurs through both inlets. At A2, situated west of the main tidal flats, flow patterns are complex due to a small southern channel that introduces flood tide from multiple directions. Drainage mainly flows northwards. A3 lies east of the tidal divide and is mostly influenced by the Frisian Inlet, although some variation occurs depending on tidal conditions. A5, further east, consistently experiences inflow and outflow solely through the Frisian Inlet.

3

Data analysis

To better understand deviations in water levels under varying wind conditions, a data analysis is performed using measurements from Aquadopp Profiler instruments (AQDs) and fixed gauge stations. The analysis focuses on multiple AQD measurement locations between Ameland and Holwerd, as well as the gauge station at Nes, covering both the winter research campaign period and the full year of 2023. These observations are essential not only for interpreting local hydrodynamic behaviour, but also for calibrating and validating the numerical model on water level.

3.1. Data overview

The dataset from the AQDs used for this analysis consists of water levels collected during a field campaign conducted between 21 November and 19 December 2023. The AQDs measured water levels every two minutes. To ensure comparability with the output of the 3Di model, the raw data was resampled to 10-minute intervals.

In addition to the AQD campaign data, water level records from fixed gauge stations operated by Rijkswaterstaat were included. These long-term stations provide an essential reference, especially for the broader temporal analysis conducted for the full year 2023. Figure 3.1 represents the RWS gauge stations and the locations of the AQDs used for model calibration.

For the wind data, measurements of KNMI station Hoorn Terschelling (251) are used, see Figure 3.1. This data is obtained from the Royal Netherlands Meteorological Institute (KNMI), which operates a nationwide network of weather stations. The closest station to the research area, Terschelling, provides hourly wind measurements, including wind speed and direction, at a standard height of 10 metres above ground level. The data is quality-controlled and publicly accessible, making it a reliable source for atmospheric input in hydrodynamic modelling. The overview of the measurement data can be found in Table 3.1.
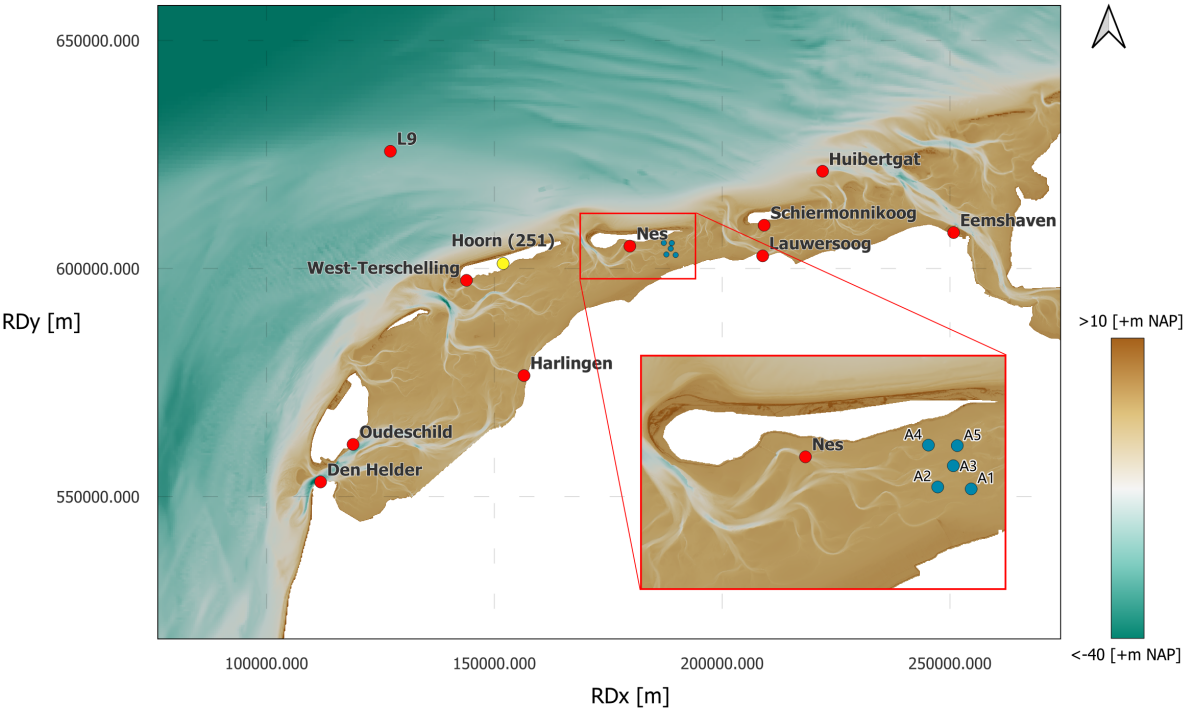
Figure 3.1: Gauge stations Rijkswaterstaat and AQD locations A1-A5 as blue dots. KNMI station Hoorn (251) depicted with a yellow dot.

| Characteristic	AQDs A1–A5	Wind data Terschelling
Location	Placed in bed on intertidal area; fixed positions	Fixed weather station on Terschelling
Measurement Height	A few centimetres above the bed	10 metres above ground level
Measured Parameters	Horizontal flow velocity (m/s), flow direction (°), water level	Wind speed (m/s), wind direction (°, rounded to 10°)
Sensor Type	Pressure-based sensors (corrected using atmospheric pressure)	Standard meteorological instruments (KNMI-certified)
Sampling Interval	Every 2 minutes	Every 1 hour
Data Processing	Depth-averaged and resampled to 10-minute intervals to match model input	Linearly interpolated to match model input frequency

Table 3.1: Overview of measurement data used for model calibration and validation.

3.2. Wind and water level deviation

To assess wind-induced water level deviations mentioned in 2.3, the above wind data are analysed. Figure 3.2 shows wind directions and speeds for the research period, typical annual and historical conditions. Comparing these periods allows verification of whether the wind conditions during the research period are representative of typical annual conditions. It can be concluded that the research period aligns well with the annual and historical wind patterns. However, during the research period, winds from the SSW and SW occurred more frequently compared to the annual and historical data. All

plots indicate a predominant west-to-south-westerly wind regime, with detailed frequency data per direction available in Appendix B. These prevailing winds may substantially affect tidal residual currents and water-level variability, which needs to be further investigated. The water level deviations are calculated as the difference between the measured water level (including wind effects) and the predicted astronomical tide.
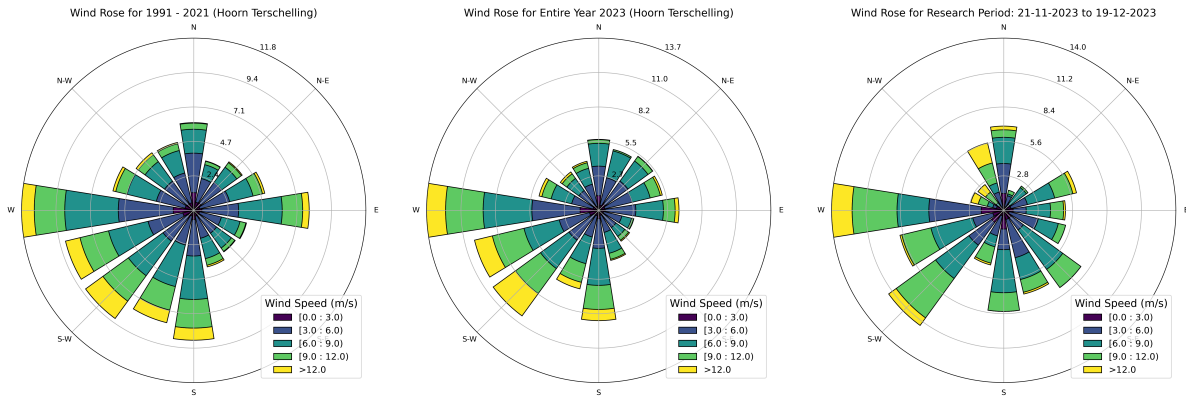
Figure 3.2: Wind roses for 1991–2021, 2023, and the research period. Data source: KNMI (https://knmi.nl).

While strong southwesterly winds can contribute to water level set-up along the Dutch coast, their impact depends on the interplay between tidal phase and wind persistence. However, northwesterly winds, rather than southwesterly winds, are typically the most effective in increasing water levels in the Dutch and German Wadden Sea, as they push water from the North Sea into the Wadden Sea basin (Colosimo et al., 2023). Conversely, easterly or northeasterly winds drive water offshore, often leading to a decrease in local water levels due to wind-induced water level set-down. Figure 3.3 demonstrates these wind-induced mean water-level variations at Nes for the research period and the year 2023. Wind speeds are depicted radially, with higher speeds further from the centre, while colour indicates deviations in water level, ranging from negative (blue, indicating water level set-down) to positive (red, indicating water level set-up). This highlights significant set-ups from southwest-to-north winds and set-downs from south-to-northeast winds.
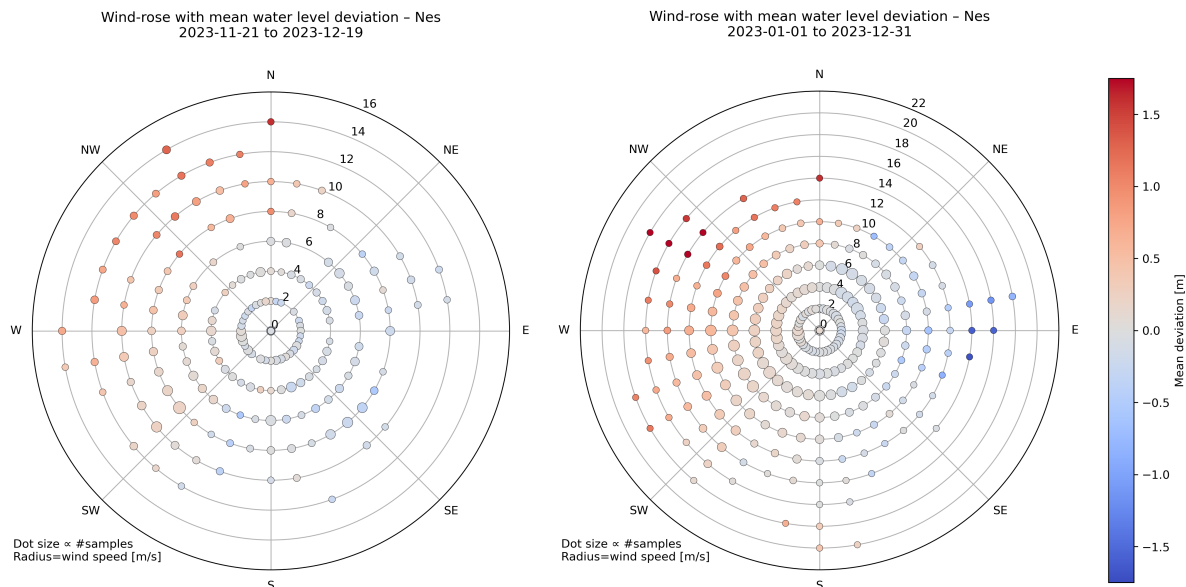
Figure 3.3: Mean water level deviations at Nes during the research period (left) and in 2023 (right). The radial axis represents wind speed (m/s), while colour indicates the water level deviation. Dot size reflects the number of samples.

The water level deviation at the measuring locations A1-A5 is also analysed. Figure 3.4 shows wind roses for locations A1 to A5 during the research period. Predominantly, stronger winds are observed coming from the northwest, west, and southwest directions, correlating mostly with positive water-level deviations (set-up). In contrast, slightly weaker winds from southwest to northeast directions typically correspond to negative water-level deviations (set-down). This pattern consistently appears across locations A1 through A5, suggesting a clear relationship between wind direction, strength, and water-level responses within the study area.

Wind Roses for A1-A5 during research period.
Wind Speed in Radius, Deviation in Color (mean deviation per bin) dot size ∝ #samples
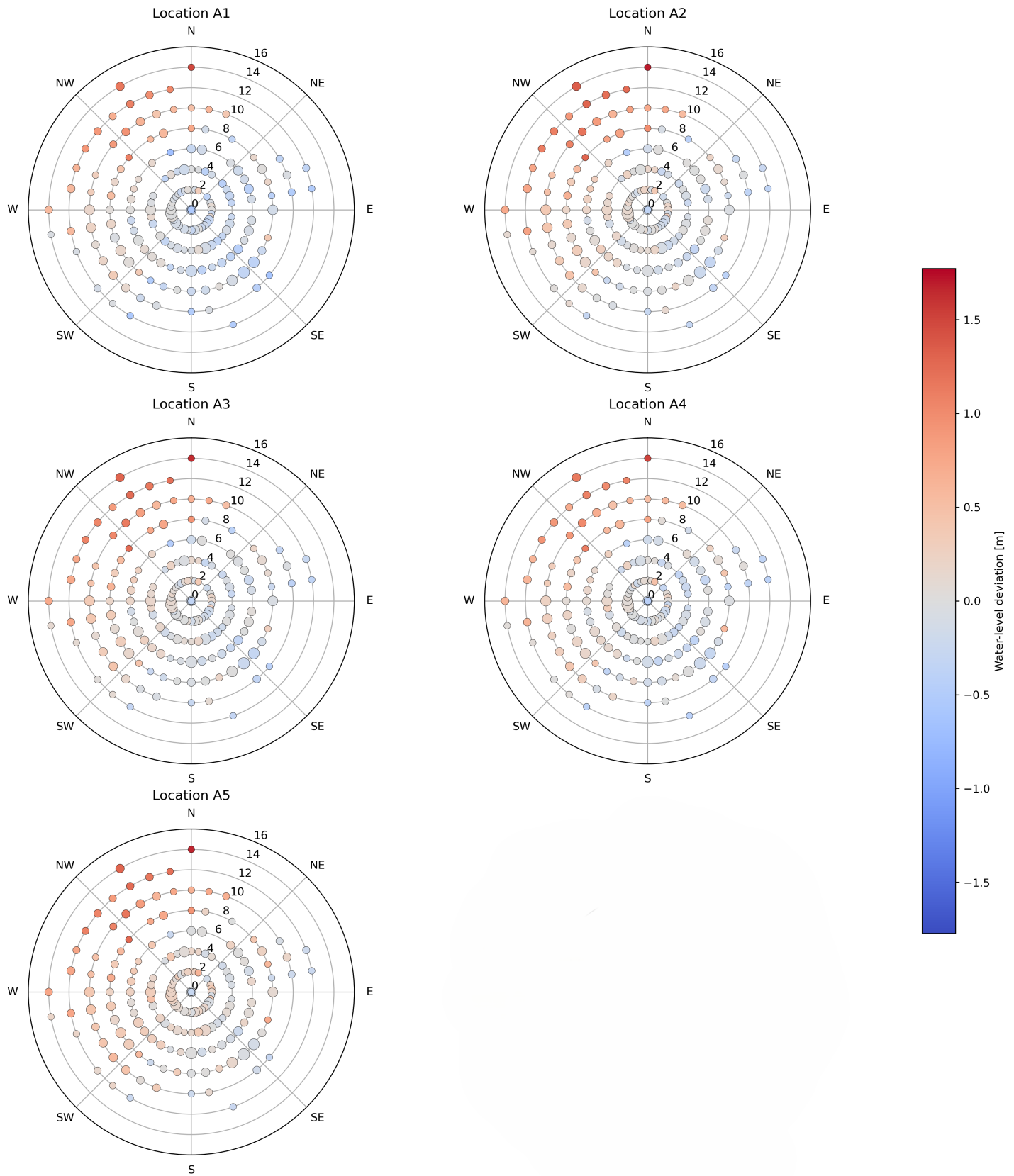
Figure 3.4: Wind rose with mean water level deviation (measured minus astronomical tide) for measurement locations A1-A5 during the research period.

Model description

4.1. Process-based numerical modelling

Hydrodynamic numerical modelling is a pivotal tool for simulating and understanding the behaviour of water systems, particularly in estuarine and coastal environments. These models solve the fundamental physics governing water movement, enabling the investigation of complex interactions between hydrodynamic processes. Examples of widely used hydrodynamic models include Delft3D, 3Di, Telemac, and Mike FM. Each model offers specific advantages and disadvantages (Table A.1), based on the physical processes represented, numerical schemes employed, and computational frameworks (de Vet et al., 2020; Gräwe et al., 2016; Sehili et al., 2014).

These models have demonstrated their capability to simulate scenarios such as tidal flows, storm surges, and sediment transport in diverse settings, from natural estuaries to engineered systems (Yin et al., 2016). Hydrodynamic models are often used to analyse the implications of sea-level rise, storm events, and anthropogenic interventions like dredging or flood defence infrastructure (French, 2008). The integration of high-resolution bathymetry and detailed boundary conditions allows these models to capture critical processes, including wave–current interactions, sediment suspension, and deposition dynamics.

By providing reliable predictions and detailed insights, hydrodynamic models are essential in decision-making processes for coastal zone management, flood risk assessment, and ecosystem conservation. Their ability to balance computational efficiency with accuracy in representing natural systems underpins their utility in both research and practical applications (Gräwe et al., 2016; Sehili et al., 2014).

4.1.1. Subgrid modelling

Subgrid modelling is a technique used to improve the accuracy of hydrodynamic simulations by incorporating high-resolution raster data (e.g. bathymetry, friction, infiltration) into coarser computational grids. This approach allows for the representation of small-scale topographic features within larger grid cells, thereby enhancing spatial detail without significantly increasing computational cost. It is particularly useful in shallow water environments, where local variations in bed elevation can strongly influence flow patterns. In this research the used high-resolution raster-data is confined to the bathymetric data (bottom topography).

A major advancement in this area was presented by Casulli (2009), who introduced a semi-implicit numerical method for solving the shallow water equations. In contrast to fully explicit methods, which rely solely on information from the current time step and often require very small time increments for stability, the semi-implicit method treats some terms, such as pressure gradients and free surface elevation, implicitly. Other terms, like advection, are handled explicitly. This combined approach increases numerical stability and efficiency, enabling the use of larger time steps while maintaining accuracy. As a result, the method also allows incorporation of detailed subgrid-scale bathymetry within each computational cell (Sehili et al., 2014).
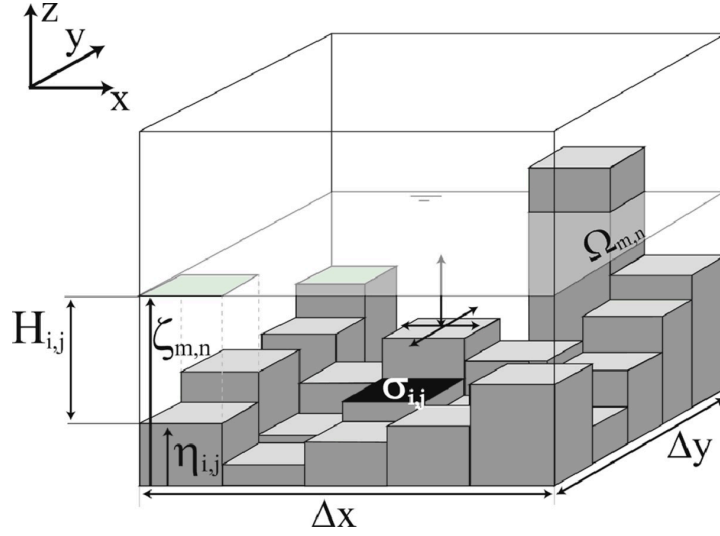
Figure 4.1: Subgrid cell (N. Volp, 2017).

Building on this framework, Volp et al. (2013) developed a two-dimensional, depth-averaged hydrody-namic model that integrates all raster-based subgrid data. This model accounts for the influence of fine-scale terrain features on flow, even when those features are smaller than the computational grid size (Volp et al., 2016). The approach has since been extended to include morphodynamic processes, which allows for the simulation of sediment transport and changes in bed elevation with high spatial resolution (N. Volp, 2017).

By embedding fine-scale bathymetry within a computationally efficient grid structure, subgrid modelling enables researchers and engineers to simulate complex hydrodynamic processes with a high degree of accuracy. This makes it an especially valuable tool for modelling flow and sediment dynamics in environments such as estuaries, tidal flats, and floodplains (Bates, 2000; Sehili et al., 2014).

4.1.2. Wind forcing in 3Di

In addition to tidal and bathymetric influences, wind forcing plays a crucial role in driving water move-ment, particularly in shallow coastal and estuarine systems. Incorporating wind forcing into the shallow water momentum equations allows for simulation of wind-induced set-up and set-down, which are im-portant in wind-driven hydrodynamics. Water is pushed in the wind direction, leading to elevated water levels (set-up) on the downwind side and reduced levels (set-down) on the upwind side. This concept is illustrated in Figure 4.2 and should be discussed in the results section where water surface gradients or residual flows are analysed.

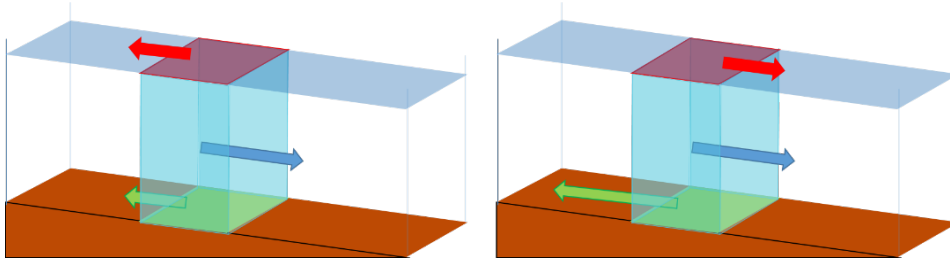**Figure 4.2:** Force balance with gravity (blue), friction (green), and wind (red). The left panel shows neutral balance, while the right illustrates set-up and set-down due to wind stress (Nelen & Schuurmans, 2024).

In 1D, wind forcing appears in the momentum balance equation as:

$$\frac{d(Hu)}{dt} = -gH\frac{\partial \zeta}{\partial x} - \frac{\tau_{\text{friction}}}{\rho} + \frac{\tau_w}{\rho} \tag{4.1}$$

- H = water depth
- u = flow velocity
- ζ = water level
- τ_{friction} = bottom friction shear stress
- ρ = water density

For 2D modelling, the wind-induced momentum is represented by the coupled system:

$$\frac{du}{dt} + g\frac{\partial \zeta}{\partial x} = -\frac{|u|u}{H_f} + \frac{\rho_{\text{air}}}{\rho_{\text{water}}}\nabla\iint_{\Omega^x}\chi^2 C_d\left(\frac{U_{\text{wind}}^x}{\chi} - u\right)^2 d\Omega^x \tag{4.2}$$

$$\frac{dv}{dt} + g\frac{\partial \zeta}{\partial y} = -\frac{|v|v}{H_f} + \frac{\rho_{\text{air}}}{\rho_{\text{water}}}\nabla\iint_{\Omega^y}\chi^2 C_d\left(\frac{U_{\text{wind}}^y}{\chi} - v\right)^2 d\Omega^y \tag{4.3}$$

- u, v = water velocities in x- and y-directions
- $U_{\text{wind}}^{x,y}$ = wind velocities in x- and y-directions
- H_f = water depth
- C_d = drag coefficient
- χ = limiting factor for shallow flows
- $\rho_{\text{air}}, \rho_{\text{water}}$ = air and water densities

These formulations ensure that wind forcing is dynamically integrated into the hydrodynamic model, reflecting both spatial flow variation and atmospheric influences with appropriate stability controls.

4.2. 3Di model configuration

For a 3Di model, a description of the bathymetry is required in combination with a roughness coefficient. To define model scenarios, forcing needs to be delivered using boundary conditions and wind fields. These wind fields can be applied from data in time series or spatially uniform with magnitude and direction.

An existing model, made by Boorsma (2024), is used. The boundary conditions will be replaced by 2D-boundary conditions based on insights from the research of K. Korporaal (2024). Further research and possible adjustments to the boundary conditions will be done in the setup of the model.

4.2.1. Model domain and DEM

The model domain defines the geographical extent of the numerical model and is essential to accurately represent the physical system under investigation. The bed levels within this domain are described using a Digital Elevation Map (DEM), which provides the spatial distribution of bathymetry and topography. The DEM is used to schematise the bathymetry of the Dutch Wadden Sea and Ems-Dollard region within the model.

For this thesis, an existing DEM developed by Boorsma (2024) is used, which builds upon the Vaklodingen dataset (Rijkswaterstaat, 2023b) and offshore bathymetric data from the KRW Slib model (Vroom et al., 2020). The Vaklodingen dataset provides high-resolution (20 m × 20 m) bathymetric measurements of the Wadden Sea and Ems-Dollard, collected in a 6-year measurement cycle. The most recent available data from 2017 to 2022 have been used to construct the DEM. Missing data points in this dataset are supplemented either through linear interpolation for single missing pixels or by using older bathymetric data from around 1990 for larger gaps. In regions where this leads to unrealistic bed level gradients, additional smoothing is applied. Furthermore, morphological features absent in older data, e.g. newly developed channels, are manually incorporated. To facilitate the use of provided boundary conditions, the model domain has been extended offshore. Here, bathymetric data from the KRW Slib model are used, with varying resolutions (200 m to 800 m), and interpolated to match the 20 m × 20 m resolution of the nearshore DEM. In addition, no-data areas on the Wadden Islands are manually adjusted to ensure that the computational grid does not intersect landmasses. This prevents

the model from generating unrealistic flow paths across the islands and reduces the number of computational grid cells, thereby lowering computational costs. An alternative method to prevent unrealistic flow across the islands is to apply grid refinements at a scale smaller than the width of the elevated parts of Ameland, effectively blocking any possible flow.
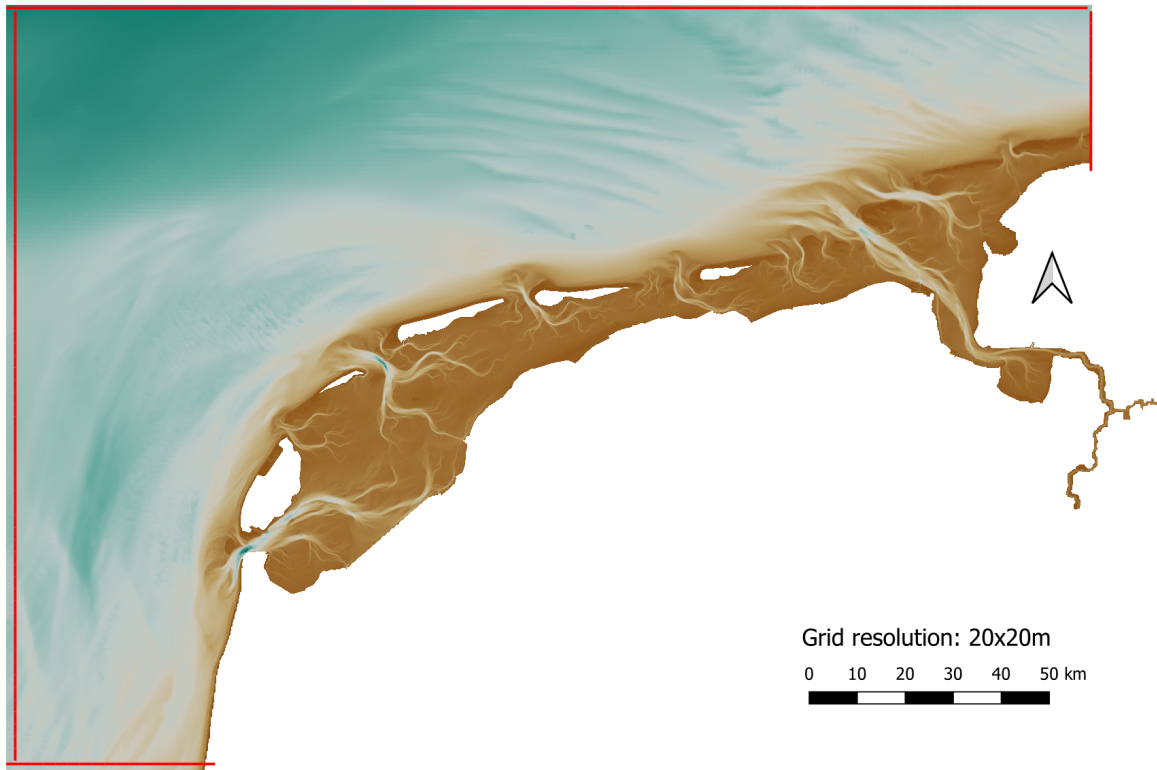

Figure 4.3: Model domain with boundary conditions in red. Time series with water levels were assigned to these boundaries. Grid resolution of the DEM is 20×20m.

4.2.2. Computational grid

The computational grid forms the spatial framework of the hydrodynamic model and plays a crucial role in balancing the trade-off between computational efficiency and the accurate representation of physical processes. In a grid-based model, the domain is divided into cells, with the model calculating water levels, velocities, and other variables at the nodes located in the centre of each cell. A finer grid resolution allows for a more detailed representation of small-scale processes, such as flow over intertidal flats or through narrow channels or where contraction occurs around the inlets. However, increasing grid resolution also leads to a higher number of computational cells, significantly increasing computational time and memory requirements.

A varying grid resolution has been applied across the model domain. In the offshore North Sea area, where detailed flow features are less critical for the research objectives, a coarser grid resolution of 2560 m × 2560 m has been applied. In contrast, within the more dynamic and morphologically complex Wadden Sea area, a finer resolution of 640 m × 640 m has been chosen to better capture the hydrodynamics of the intertidal flats and channels. This is more elaborated in Section 4.3.2.

The transition between different grid resolutions is handled using the quadtree grid structure implemented in 3Di (Stelling, 2012). In this method, cells can only border cells that are half or double their size, ensuring stable transitions between coarse and fine resolutions. As a result, intermediate cell sizes of 1280 m × 1280 m are applied in specific areas to facilitate a smooth connection between the coarse North Sea grid and the finer Wadden Sea grid, see Figure 4.4. Additionally, a fixed subgrid resolution of 20 m × 20 m is applied throughout the whole model domain.
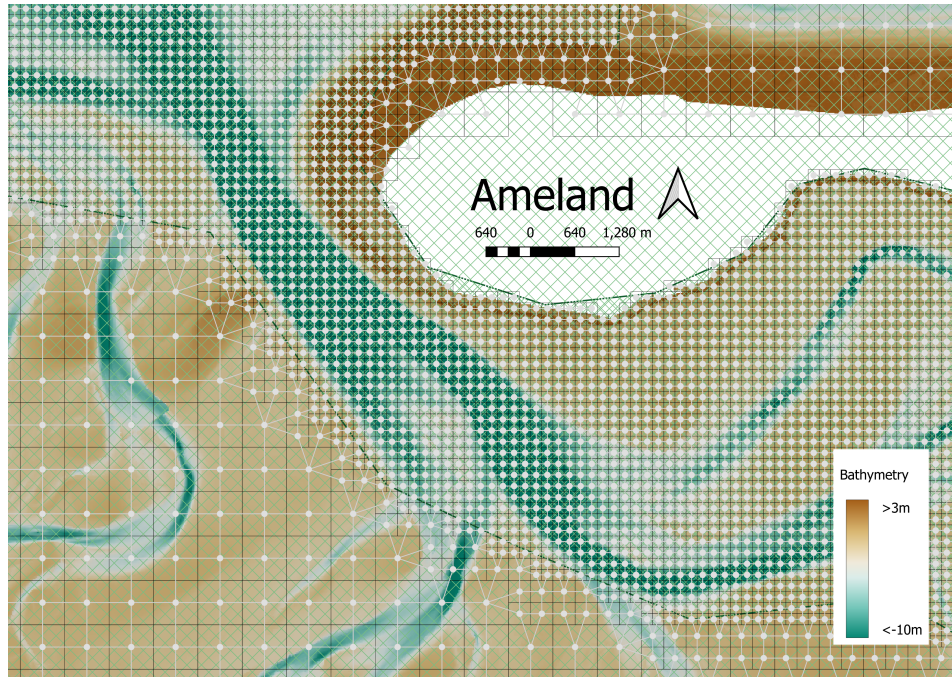
Figure 4.4: Quadtree grid structure of the 3Di model around Ameland. Computational nodes in the centre of the rectangulars, and the associated flow lines from the nodes.

During the calibration phase of this study, further scenario-dependent grid refinements will be applied in specific regions of interest to improve model accuracy. These refinements and their implementation will be discussed in detail in the calibration chapter.

4.2.3. Boundary conditions

Boundary conditions are essential in hydrodynamic modelling, as they define the external forcing at the edges of the model domain. These typically consist of water levels, flow velocities, or discharge rates and strongly influence the accuracy of internal flow simulations. In this study, water level boundaries were applied along the offshore edges of the model to incorporate tidal and meteorological influences, based on the Dutch Continental Shelf Model (DCSM) developed by Deltares (Zijl et al., 2018). This approach, where a smaller-scale model inherits its boundary conditions from a larger-scale model, is referred to as model nesting and is commonly applied in numerical modelling to ensure consistency between different spatial scales.

The DCSM boundary conditions include both tidal signals and meteorological forcing. The meteorological input for the DCSM-model is based on ERA5, the fifth-generation global atmospheric reanalysis dataset provided by ECMWF (Deltares, 2022). In the 3Di model, these were implemented as time series of water levels mapped to boundary nodes corresponding to DCSM output locations.

To validate the applied boundaries, modelled water levels from the DCSM were compared to observed levels at several gauge stations within the domain. Root mean square error (RMSE) values were computed for the period 1 October 2023 to 2 February 2024. These were found to be within the accuracy range reported by Deltares (2022) for 2013–2017, supporting the reliability of the boundary conditions used in this study.

Station	RMSE (m)
Den Helder	0.1308
Den Oever buiten	0.1775
Eemshaven	0.1393
Harlingen	0.1303
Huibertgat	0.1460
Lauwersoog	0.1268
Oudeschild	0.1136
Schiermonnikoog	0.1261
West-Terschelling	0.1496
Nes	0.1288

Table 4.1: RMSE between DCSM-model outputs and RWS measurements for the period 2023-10-01 to 2024-02-02. Stations depicted in Figure 3.1

The RMSE values presented in Table 4.1 are derived from a calibrated DCSM-model simulation using Delft3D, with spatially varying roughness values applied across the domain.

For this study, the boundary conditions are also examined for anomalies in water level time series. A noticeable double peak ("agger" in Dutch) has been identified along the southern and western boundaries, extending up to a latitude near North Texel. This double peak gradually diminishes or disappears further north along the location of the chosen boundary condition. To investigate this, water levels at a northern boundary point further north (BC-West-45) are compared with those from the K14-alpha measurement platform, located perpendicular to but outside the model domain. The comparison, shown in Appendix C, resulted in a root mean square error (RMSE) of 0.118m for the period from 30 November to 14 December 2023. Over a longer time series, from 1 October to 31 December 2023, the RMSE was 0.135m. The model slightly underestimates high water levels and marginally overestimates the low water troughs.

The double peak may be caused by the interaction of two amphidromic tidal systems. However, determining the exact origin falls outside the scope of this research. The effect is clearly visible in the 3Di-modelled water levels at Den Helder, which do not correspond well with the observed data from the Den Helder gauge station. An example time series illustrating this discrepancy at Den Helder is provided in Figure 4.5.
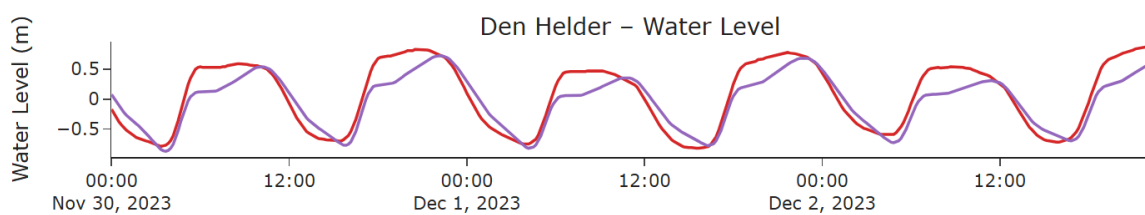
Figure 4.5: Water level at Den Helder. The modelled data is shown in purple, the measured data in red.

4.2.4. Initial conditions
Initial conditions define the starting state of the model and are important to ensure a realistic development of the simulated processes over time. A 2D initial water level file used in the 3Di model made by Boorsma (2024) is used. The aggregation method used to read the raster is set to Minimum (Min), which assigns the minimum value of the variable within the aggregation interval to the computational

cells. This approach ensures that the initial water level does not exceed the values specified in the raster, supporting a stable and realistic model start-up.

Because the initial water levels are not fully consistent with the boundary conditions, the model exhibits a spin-up effect, characterised by transient oscillations or "wiggles" in water levels, as it adjusts to a dynamic equilibrium. To minimise the influence of these initial imbalances on the results, the simulation is started two days earlier than the analysis period. Only the data from the windless period after this spin-up phase are used for evaluation, ensuring that the analysed outputs reflect a stable and physically consistent model state. The spin-up effect is also visualised in Figure 4.12.

4.2.5. Roughness and wind forcing

Bottom roughness is a key parameter in hydrodynamic modelling, as it represents the resistance of the bed acting on the flow. This resistance, known as frictional resistance or bed shear stress, arises from the interaction between the moving water and the roughness elements on the bed surface, such as sediment grains, vegetation, or man-made structures. It acts to slow down the flow and dissipate energy, playing a crucial role in shaping velocity profiles and flow distribution.

In the 2D domain of the model, bottom friction is dynamically calculated using the local flow depth at each subgrid pixel within the momentum domain. In 3Di, two commonly used formulations for bottom shear stress can be applied: the Manning formulation and the Chézy formulation. These express the bed shear stress τ_b, which enters the momentum equations as a frictional resistance term.

The bottom shear stress using the Chézy formulation is expressed as:

$$\tau_b = \rho\,g\,\frac{u^2}{C^2} \tag{4.4}$$

where:

- τ_b = bottom shear stress [N/m^2]
- ρ = water density [kg/m^3]
- g = gravitational acceleration [m/s^2]
- u = depth-averaged flow velocity [m/s]
- C = Chézy coefficient [m$^{1/2}$/s]

Alternatively, the Manning formulation is expressed as:

$$\tau_b = \rho\,g\,n^2\,\frac{u^2}{h^{1/3}} \tag{4.5}$$

where:

- n = Manning roughness coefficient [s/m$^{1/3}$]
- h = local water depth [m]

In the momentum equations, the frictional acceleration term is given by $\tau_b/(\rho h)$, resulting in:

$$\frac{\tau_b}{\rho h} = \begin{cases} g\dfrac{u^2}{C^2 h} & \text{(Chézy)} \\ gn^2\dfrac{u^2}{h^{4/3}} & \text{(Manning)} \end{cases}$$

As a starting point, initial roughness values are adopted from previous modelling studies by Boorsma (2024). A Chézy coefficient of $C = 100$ m$^{1/2}$/s is used for the deeper North Sea area, representing a relatively smooth bed, and a Chézy coefficient of $C = 85$ m$^{1/2}$/s is applied within the Wadden Sea area, reflecting higher bottom friction in the shallower regions.

These roughness values will be calibrated in the existing model to improve the agreement between simulated and observed water levels. Calibration is necessary because bottom friction strongly influences the propagation of tides, flow velocities, and especially the tidal range. A smoother bed, represented by a higher Chézy value, typically increases the tidal range within the model, while a rougher bed dampens tidal amplitudes.

Wind forcing is an important forcing in hydrodynamic modelling, as it directly influences surface water movement and residual flows. The wind time series from KNMI, provided at a reference height, are used as input to the model and converted to surface wind speeds using a logarithmic wind profile. These corrected wind speeds are then used to calculate the spatially uniform wind shear stress applied across the model domain, driving surface water movement through the hydrodynamic equations.

The vertical wind profile is corrected using a logarithmic law to convert the reference wind speed at height z to the effective wind speed at the water surface. This profile is given by:

$$u_{\text{wind}}(z, t) = \frac{u_*}{\kappa} \log\left(\frac{z}{z_0}\right)$$

(4.6)

- $u_{\text{wind}}(z, t)$ = wind speed at height z
- u_* = friction velocity (resistance speed)
- κ = von Kármán constant
- z_0 = surface roughness length

The wind drag coefficient relates the wind speed measured at 10 m above the surface to the wind stress exerted on the water body. It is used to calculate the wind shear stress that the wind applies to a body of water, which in turn drives surface currents and can influence waves, tides, and circulation patterns.

Wind stress acting on the water surface is a key term in the momentum equations and is calculated in 1D using the formula:

$$\tau_w = -\rho_a C_d L \left| u_{\text{wind}} \right| u_{\text{wind}}''$$

(4.7)

- τ_w = wind shear stress
- ρ_a = air density
- C_d = drag coefficient of the wind
- L = local wind shielding factor
- $\left| u_{\text{wind}} \right|$ = wind speed magnitude
- u_{wind}'' = wind speed in the direction of the channel

In 2D, the wind stress is integrated over the model domain Ω with a stability correction factor χ to prevent overestimation of wind forcing in thin water layers:

$$\tau_w = \rho_{\text{air}} \iint_\Omega \chi^2 C_d L \left(\frac{u_{\text{wind}}}{\chi} - u\right) \left(\frac{u_{\text{wind}}''}{\chi} - u\right) d\Omega$$

(4.8)

This formulation accounts for the relative velocity between wind and water and stabilizes the simulation when flow speeds approach critical values.

4.3. Model assessment
4.3.1. Performance criteria
The quality of the model calibration is assessed using several performance indicators. For each indicator, the Root Mean Square Error (RMSE) is calculated between the modelled results and the observed data.

The RMSE is defined as:

$$RMSE = \sqrt{\frac{1}{n} \sum_{i=1}^{n} \left(x_i^{\text{model}} - x_i^{\text{obs}} \right)^2} \tag{4.9}$$

Where:

- x_i^{model}: modelled value at time step i
- x_i^{obs}: observed (measured) value at time step i
- n: total number of time steps

This equation is applied to compute the RMSE for the following performance indicators for different time series at different locations. Figure 4.6 visualises the indicators:

- Absolute water level (m). Depicted with a orange dotted line.
- Peaks and troughs of water level (m): the difference between the modelled and observed low water and high water levels per tidal cycle. Depicted with a green arrow (LW) and a yellow arrow (HW).
- Tidal range (m): the difference between high and low water for each tidal cycle. Depicted with a black arrow.
- Flood and ebb duration (hours): the time duration of rising and falling tides
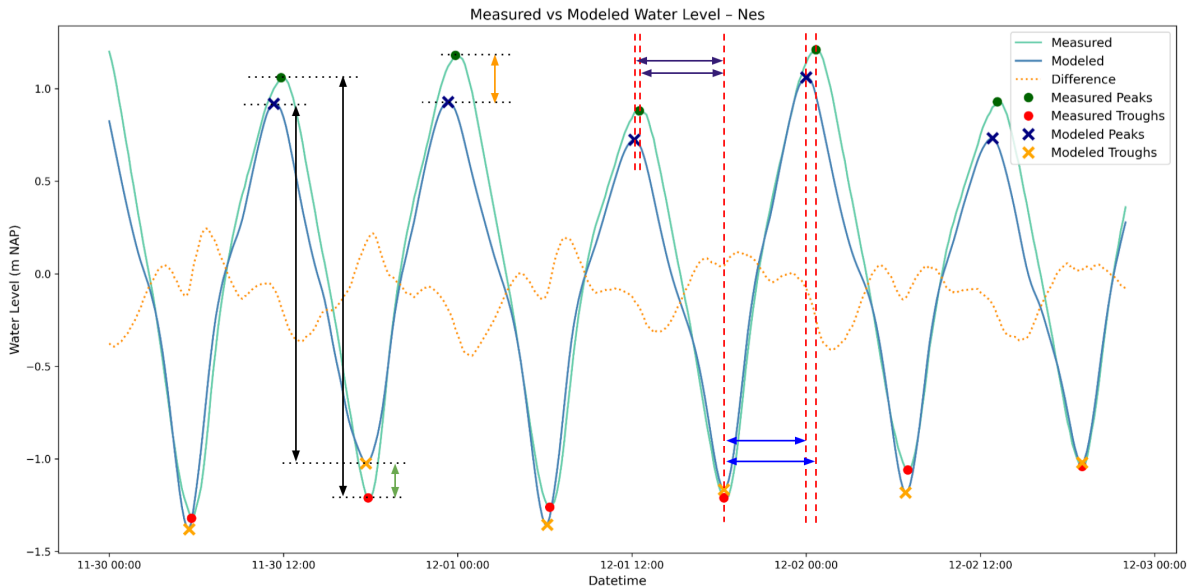
Figure 4.6: Performance criteria: water level difference (orange dotted), tidal range (black arrows), low water (green arrow) difference & high water difference (yellow arrow), ebb duration (dark blue arrows) & flood duration (blue arrows).

Table 4.2 presents an overview of the performance criteria evaluated at the various locations. For the RWS gauge stations, data are available for all performance metrics, because a full Low-High water signal can be measured. In contrast, for the additional measurement locations, only high water levels are

assessed. This limitation arises because low water levels at AQD locations are influenced by bed exposure during low tide, rendering the determination of actual low water levels unreliable. Consequently, tidal range, ebb duration, and flood duration cannot be accurately computed at these locations. This table is used for both model calibration and validation to compare model performance.

Table 4.2: RMSE Table per measurement location for the windstill period, non-calibrated.

Station	WL (m)	HW (m)	LW (m)	TR (m)	Ebb dur. (h)	Flood dur. (h)
A1	–	0.23	–	–	–	–
A2	–	0.37	–	–	–	–
A3	–	0.35	–	–	–	–
A4	–	0.25	–	–	–	–
A5	–	0.40	–	–	–	–
Den Helder	0.29	0.25	0.12	0.30	0.85	0.85
Eemshaven	0.27	0.44	0.16	0.58	0.54	0.51
Harlingen	0.31	0.34	0.33	0.20	0.59	0.56
Huibertgat	0.28	0.42	0.15	0.61	0.38	0.34
L9 platform	0.19	0.25	0.07	0.23	0.19	0.19
Lauwersoog	0.29	0.42	0.19	0.31	0.50	0.48
Nes	0.28	0.35	0.18	0.31	0.44	0.42
Oudeschild	0.24	0.21	0.17	0.26	0.58	0.56
Schiermonnikoog	0.28	0.39	0.17	0.49	0.41	0.40
West-Terschelling	0.23	0.28	0.16	0.22	0.34	0.36
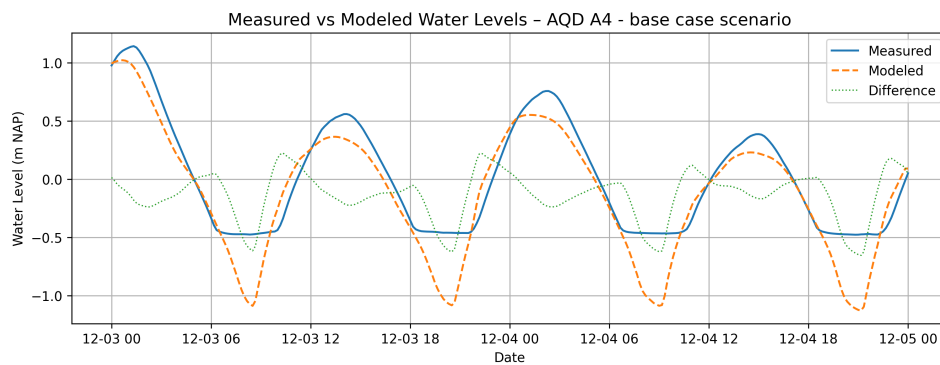
Figure 4.7: Water level for AQD at location A4, showing discrepancies for low water i.e. the bed level.

4.3.2. Model calibration

The model calibration is carried out in a structured, chronological approach, consisting of three main steps. Each step focuses on adjusting specific model parameters to improve the agreement between modelled results and measured data for the deployed measurement locations A1–A5 during the research period and the fixed gauge stations from Rijkswaterstaat mentioned in Chapter 3. The calibration is done on water level time series.

1. Grid Refinement

In the first step, grid refinements are applied to improve the spatial resolution of the model in key locations. This is mainly done in:

- contraction areas around inlets,
- tidal channels,
- and the intertidal area of specific interest, e.g. gauge stations and measurement locations A1-A5.

These refinements allow for a better representation of local flow patterns, which is essential for accurate modelling of tidal propagation and water levels.

Different grid refinements are applied, and the model is run with a uniform Chézy roughness value of 85 $m^{1/2}$/s during the windless period from 30 November to 2 December 2023.

In this study, it was found that applying 2–4 times finer grid refinements across the entire Wadden Sea area did not significantly improve the accuracy of water levels at the calibration locations. Additionally, a refinement is applied off the Dutch west coast to examine whether bathymetry plays a role in producing the double-peaked water levels observed at the boundary conditions. Refining the grid by one or more scales results in differences of only one or a few centimetres in water levels at certain locations, while most calibration points show negligible changes.

Based on this comparison of refinement configurations, the final grid setup is defined as follows (see Figure 4.8): the Wadden Sea basin is assigned a resolution of 640×640 m, the tidal inlets and channels connecting the Wadden Sea to the North Sea are refined to 160×160 m, and the AQD locations are further refined to 40×40 m.
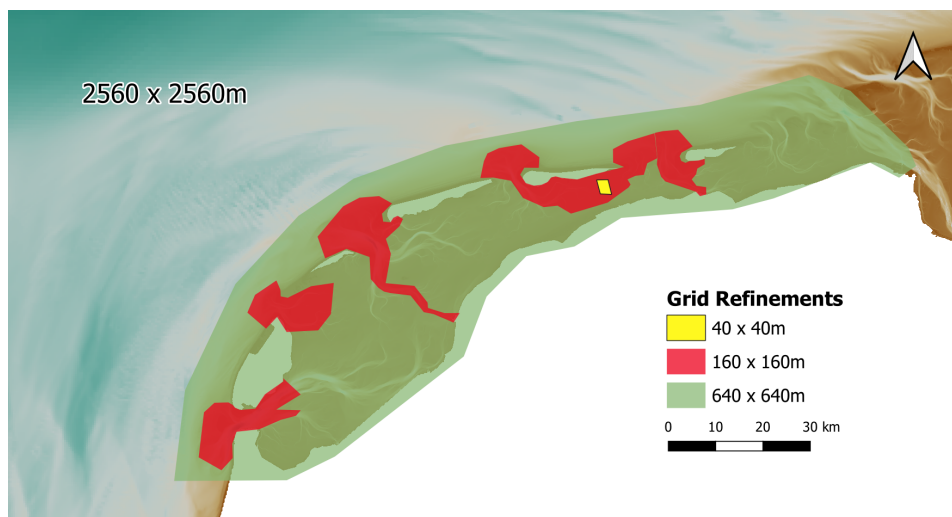
Figure 4.8: Placed grid refinements. Yellow: 40x40m, red: 160x160m, green: 640x640m.

2. Roughness Coefficient Adjustment

In the second step, the roughness coefficients (Manning and Chézy values) are adjusted. Chézy values ranging from 50 $m^{1/2}$/s to 120 $m^{1/2}$/s are initially modelled. Subsequently, a spatial distinction between the western and eastern Wadden Sea is introduced. This distinction is based on the DCSM-model (Zijl et al., 2018) and the work of Boorsma (2024). A Chézy value of 85 $m^{1/2}$/s for the western Wadden and 120 $m^{1/2}$/s for the eastern Wadden yields the lowest RMSE.

In addition, roughness is also investigated using Manning coefficients instead of Chézy, to assess potential improvements in model performance. Manning takes into account the hydraulic radius and is also used in the Dutch Continental Shelf Model (DCSM) (Zijl et al., 2018). Manning values from 0.010 to 0.020 $s/m^{1/3}$ are simulated in incremental steps. The results are comparable to those obtained with Chézy under hydraulically smooth conditions. A Manning value of 0.015 $s/m^{1/3}$ for the western Wadden and 0.010 $s/m^{1/3}$ for the remainder of the model domain slightly outperforms the Chézy configuration.

It should be noted that achieving very smooth hydraulic conditions (Chézy 120 $m^{1/2}$/s and Manning 0.010 $s/m^{1/3}$) across the entire model domain improves the representation of peaks in the intertidal area. However, this also results in greater deviations for other performance criteria at the calibration

measurement locations, such as ebb and flood duration. Therefore, selecting the final roughness values requires balancing the model performance at the RWS gauge stations and the Aquadopp Profiler (AQD) locations on the intertidal flats.

The following results are obtained using the chosen Manning roughness values and applied grid refinements, listed in Table 4.3. Table 4.4 gives a summary of Tables 4.2 and 4.3 on grid refinements and roughness. Besides the total average and median of the RMSE results table, a distinction is made between the gauge stations in the western and the eastern Wadden, since different roughness values are used and the focus of this research is on the Pinke Wad, located in the eastern Wadden.

Table 4.3: RMSE Table per measurement location for the windstill period, calibrated on grid refinements and roughness.

Station	WL (m)	HW (m)	LW (m)	TR (m)	Ebb dur. (h)	Flood dur. (h)
A1	–	0.08	–	–	–	–
A2	–	0.18	–	–	–	–
A3	–	0.19	–	–	–	–
A4	–	0.08	–	–	–	–
A5	–	0.25	–	–	–	–
Den Helder	0.24	0.13	0.08	0.08	1.08	1.21
Eemshaven	0.22	0.31	0.07	0.29	0.64	0.62
Harlingen	0.15	0.12	0.23	0.14	0.70	0.60
Huibertgat	0.25	0.34	0.16	0.51	0.13	0.27
L9 platform	0.17	0.23	0.05	0.28	0.13	0.18
Lauwersoog	0.22	0.26	0.06	0.23	0.15	0.25
Nes	0.17	0.15	0.07	0.11	0.35	0.32
Oudeschild	0.17	0.06	0.16	0.16	0.53	0.63
Schiermonnikoog	0.22	0.26	0.05	0.26	0.29	0.18
West-Terschelling	0.12	0.11	0.05	0.12	0.20	0.13

Table 4.4: RMSE Comparison summary between non-calibrated (Table 4.2) and calibrated model (Table 4.3) on grid refinements and roughness.

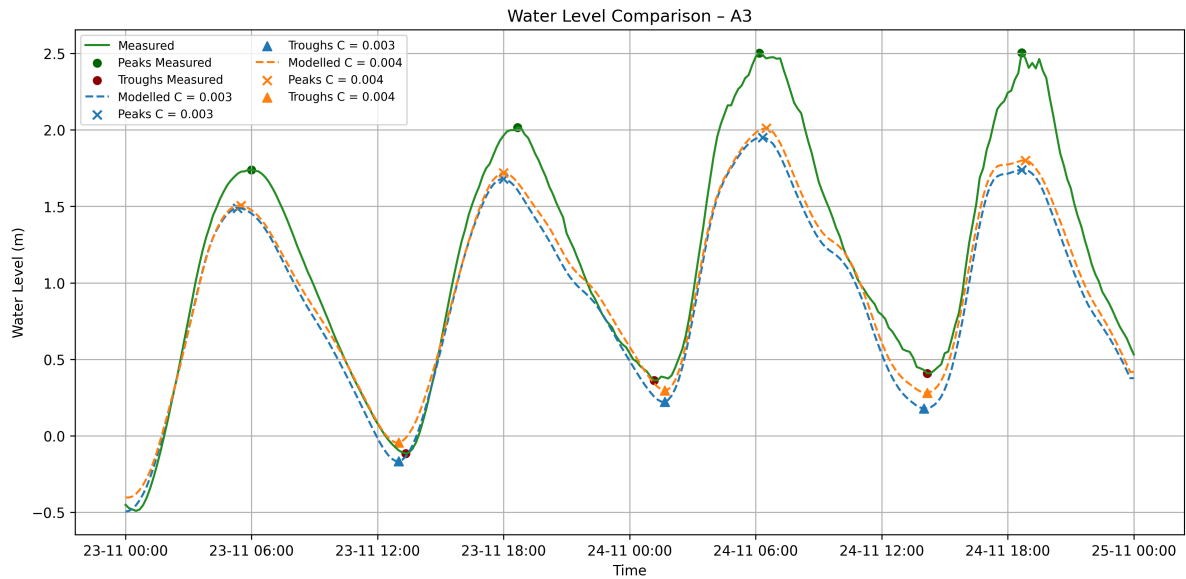| Metric	RMSE Non-Calibrated	RMSE Calibrated	△RMSE
Total average	0.34	0.25	0.09
Total median	0.31	0.18	0.13
Western Wadden average	0.36	0.30	0.06
Western Wadden median	0.29	0.15	0.14
Eastern Wadden average	0.35	0.20	0.15
Eastern Wadden median	0.37	0.22	0.15

3. Wind Drag Coefficient Calibration

Two distinct periods are selected to calibrate the wind drag coefficient. Initially, to isolate the model's baseline behaviour without substantial wind influence, the calibration focuses on a windstill period from 30 November to 2 December 2023. Model simulations are conducted with wind drag coefficients ranging from 0.001 to 0.01. The lowest RMSE is achieved at a coefficient of 0.003 for the windstill period.

Table 4.5 summarises these results, showing the change in RMSE compared to the non-calibrated model (default wind drag value 0.005 in 3Di) for the windstill period.

Table 4.5: Wind drag coefficient comparison: windstill period

Metric	Non-Calibrated	Calibrated	△ RMSE
Total average	0.267	0.256	0.011
Total median	0.211	0.209	0.002
Western Wadden average	0.290	0.284	0.006
Western Wadden median	0.156	0.157	-0.001
Eastern Wadden average	0.231	0.216	0.015
Eastern Wadden median	0.249	0.215	0.034

The calibration subsequently focuses on a period characterised by strong winds and significant water level setup, from 23 to 25 November 2023. During this period, accurately modelling high water peaks poses a challenge. Nonetheless, a wind drag coefficient of 0.004 minimises the average RMSE for the strong wind period and improves the representation of low water levels and timing on intertidal flats slightly compared to a drag coefficient of 0.003 (see Figure 4.9). Consequently, a wind drag coefficient of **0.004** is selected and applied to all further scenario simulations. Table 4.6 provides detailed RMSE values and change in RMSE for this strong wind period.

Figure 4.9: Water level at location A3 using wind drag coefficients of 0.003 and 0.004 during the strong wind period.

Table 4.6: RMSE for Wind drag coefficient comparison: strong wind period

| Metric	Non-Calibrated	Calibrated	△ RMSE
Total average	0.33	0.29	0.04
Total median	0.26	0.24	0.02
Western Wadden average	0.26	0.26	0.00
Western Wadden median	0.19	0.21	-0.02
Eastern Wadden average	0.38	0.30	0.08
Eastern Wadden median	0.28	0.29	-0.01

4.3.3. Model validation

The validation is performed using data from a period with intermediate wind from a different direction than the strong wind calibration phase. An average value of 8 m/s from 3 December 2023 to 5 December is chosen, with wind direction varying from south-west to east. This results in the following RMSE table:

Table 4.7: Root Mean Square Errors (RMSE) for water levels, tidal ranges, and tidal durations at various stations

Station	WL (m)	HW (m)	LW (m)	TR (m)	Ebb dur. (h)	Flood dur. (h)
A1	–	0.22	–	–	–	–
A2	–	0.39	–	–	–	–
A3	–	0.35	–	–	–	–
A4	–	0.19	–	–	–	–
A5	–	0.36	–	–	–	–
Den Helder	0.21	0.26	0.06	0.27	0.33	0.17
Eemshaven	0.25	0.43	0.13	0.65	0.56	0.65
Harlingen	0.24	0.32	0.23	0.11	0.29	0.41
Huibertgat	0.24	0.34	0.08	0.39	0.30	0.43
L9 platform	0.18	0.22	0.05	0.21	0.32	0.29
Lauwersoog	0.25	0.39	0.10	0.30	0.56	0.65
Nes	0.24	0.32	0.12	0.24	0.68	0.67
Oudeschild	0.16	0.20	0.09	0.13	0.65	0.35
Schiermonnikoog	0.22	0.33	0.05	0.30	1.08	1.07
West-Terschelling	0.18	0.22	0.10	0.16	0.29	0.22

The total average RMSE value is 0.31, with notable deviations observed at both the AQD locations and the RWS gauge stations. Low water levels are captured very well, whereas high water levels show significant deviation.

As part of the model validation, it is also useful to examine water level gradients between different locations. This provides insight into both the timing of water level changes and the magnitude of spatial differences. Figure 4.10 presents two plots showing the gradients between Nes and Lauwersoog, and between Schiermonnikoog and Lauwersoog. An increase in the asymmetry can be observed for the modelled water level of Lauwersoog and Schiermonnikoog.
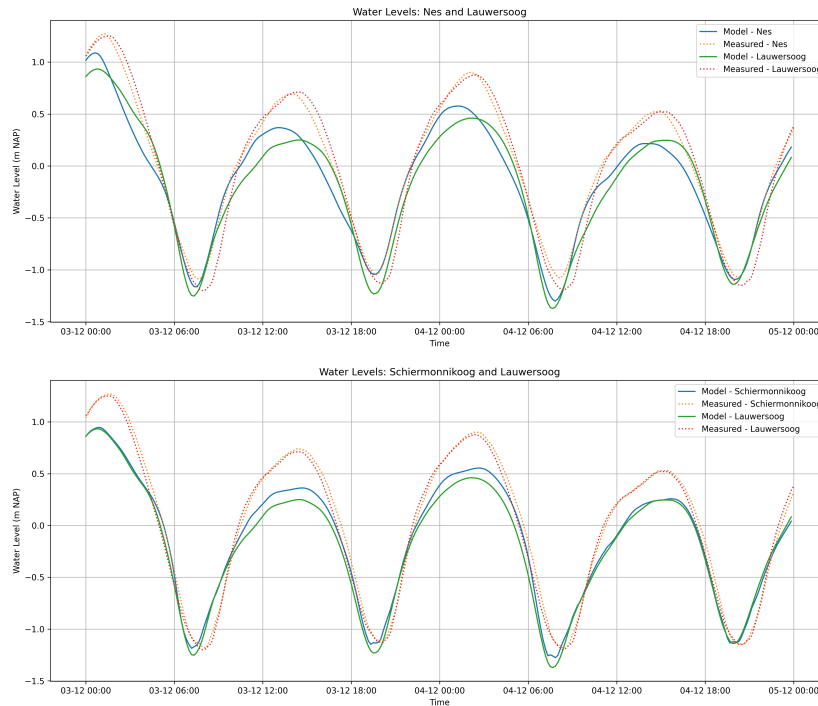
Figure 4.10: Water level gradients between Nes and Lauwersoog (top) and Schiermonnikoog and Lauwersoog (bottom).

Figure 4.10 shows the modelled and measured water levels at Nes, Schiermonnikoog, and Lauwersoog. The low-water troughs are generally well captured by the model. In contrast, the high-water peaks are consistently underestimated, as also observed during calibration. This leads to RMSE values that are 4–12 cm higher than those from the DCSM-model.

The spatial water level gradients between Schiermonnikoog and Lauwersoog, and between Nes and Lauwersoog, reveal systematic deviations. During high tide, the measured water levels at the islands and Lauwersoog are nearly equal, while the model underestimates the island levels, creating a difference in shape between "Model - Nes" and "Model Lauwersoog", compared to the measured signals. At low tide, the model reproduces the gradient correctly but slightly overestimates its magnitude.

4.4. Scenarios

To assess the hydrodynamic response of the system to varying wind conditions, a base-case scenario without wind and twelve wind-forcing scenarios are simulated, as detailed in Table 4.8. Based on prior data analysis, winds from the north, west, and east were identified as having the most significant influence on water level variations, these three directions were therefore selected for the simulations. To represent the range of occurring wind strength, four wind speeds were chosen to span conditions from moderate breezes (1 Bft) to very strong winds (9 Bft), covering both typical and storm-like scenarios.

Each simulation applies a spatially uniform (invariant) wind field across the model domain, varying only in magnitude and direction. The wind directions considered are North, East, and West, each modelled at four different wind speeds corresponding to 1, 3, 6, and 9 Beaufort (converted to 1, 4, 12, and 23 m/s, respectively). These scenarios are imposed on a windstill period to isolate the effects of wind forcing. Otherwise, existing wind effects are already embedded in the boundary condition water levels. For consistency and comparability, the analysis focuses on the final tidal cycle of each simulation, by which time the modelled system has fully adjusted to the applied wind forcing.

Table 4.8: List of the base case scenario and the 12 wind simulations with direction. Beaufort scale magnitude (converted to m/s), average wind simulated, and alias.

Simulation #	Direction	Magnitude (Bft / m/s)	Wind Simulated [m/s]	Alias
0	-	0 (no-wind)	0	Base-0
1	North	1 Bft / 0–1.5 m/s	1	North-1
2	North	3 Bft / 3.4–5.4 m/s	4	North-3
3	North	6 Bft / 10.8–13.8 m/s	12	North-6
4	North	9 Bft / 20.8–24.4 m/s	23	North-9
5	East	1 Bft / 0–1.5 m/s	1	East-1
6	East	3 Bft / 3.4–5.4 m/s	4	East-3
7	East	6 Bft / 10.8–13.8 m/s	12	East-6
8	East	9 Bft / 20.8–24.4 m/s	23	East-9
9	West	1 Bft / 0–1.5 m/s	1	West-1
10	West	3 Bft / 3.4–5.4 m/s	4	West-3
11	West	6 Bft / 10.8–13.8 m/s	12	West-6
12	West	9 Bft / 20.8–24.4 m/s	23	West-9

To understand the frequency of these wind scenarios, the wind data analysis from Chapter 3 is filtered by direction and magnitude to match the described model scenarios. The results are shown in Figure 4.11 for the year 2023 and the historical period 1991–2021. It can be observed that wind speeds corresponding to 9 Bft did not occur from any of the simulated directions in either period, although one 9 Bft event from the south was recorded in 2023. The inclusion of 9 Bft scenarios aims to assess extreme, though rare, wind conditions.

(a) Year 2023

(b) Historical period 1991-2021.
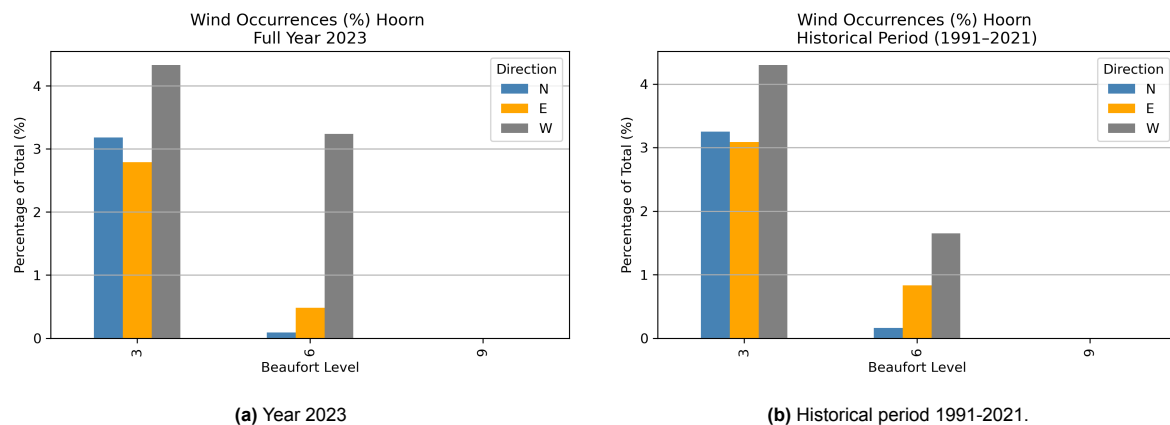
Figure 4.11: Wind occurrences (%) at Hoorn by direction and Beaufort level.

The simulations last for 4 days and 22 hours, commencing on 28 November 2023 and concluding at 22:00 on 2 December 2023. This duration is chosen to eliminate the spin-up effect and to focus on a period of near-calm wind conditions. The existing wind forcing is not removed from the boundary water level time series. Spring tide at Nes occurs on 30 November. The last full tidal cycle (high water to high water) within the simulation period, beginning two days after the spring tide, is selected for the analysis of the model scenarios. This period is chosen based on data analysis, which has shown the smallest deviation between the measured water level at Nes and the astronomical tide for this simulation period. The mean deviation over the selected tidal cycle is –0.071 m.

Analysis has indicated that water levels do not continue to increase over successive tidal cycles during the scenario runs. This is illustrated in Figure 4.12, which shows the modelled water levels in the channel at Nes for various scenarios. The spin-up period is shown in grey, while the analysed tidal cycle is highlighted in green. The figure demonstrates that there is no increasing water level gradient attributable to the spatially uniform wind applied across different magnitudes and directions. It was also analysed that for the plotted scenarios the differences in low water levels between wind scenarios are more pronounced than those in high water levels, particularly under conditions of increasing wind setup, when the tidal range becomes smaller at higher wind speeds. Notably, the variation in daily inequality appears to be larger than the difference between spring tide and the analysed tidal cycle.
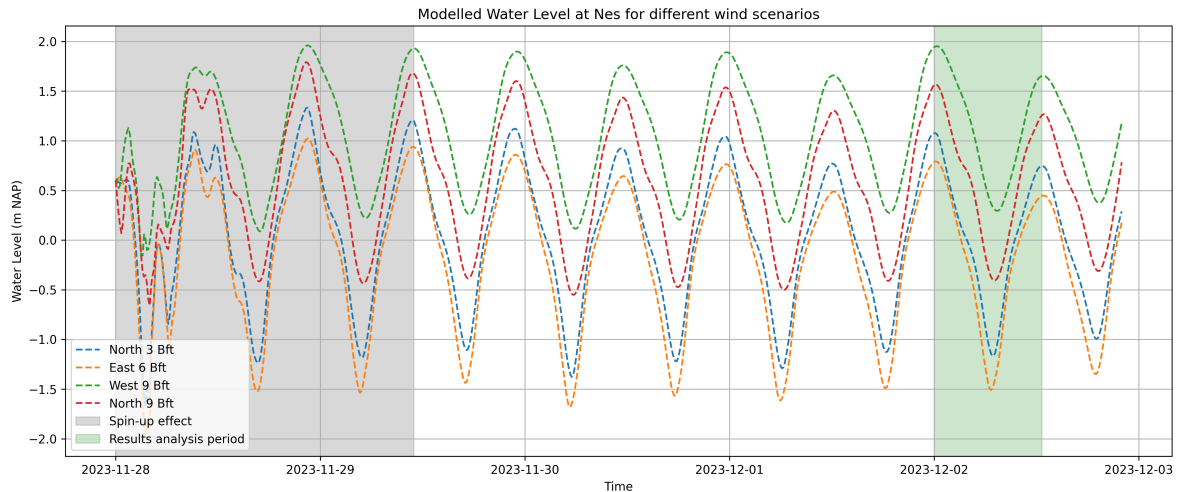
Figure 4.12: Modelled water levels for different scenarios at Nes. The spin-up effect in grey and the tidal cycle for analysis visualised in green.

4.4.1. Postprocessing 3Di results
For each scenario, the exposure time, exposure area, and flow patterns are visualised using the output data from 3Di. Exposure times are shown for one tidal cycle, both in absolute terms and as differences relative to the base-case scenario. The 1st and 99th percentiles are used to filter out extreme values for the visualisation of the exposure maps.

Flow patterns are depicted using quiver plots, which are spatially averaged at each time step. To compute the residual currents, temporal averaging over one tidal cycle has been applied at fixed locations (Nes and A1–A5). These six locations are selected for consistency and to enable comparison with measurement data in future research. Finally, residual currents are visualised on the Pinke Wad to provide clearer insight into the spatial hydrodynamic response of the system to wind forcing. The results of these analyses are presented and discussed in Chapter 5.
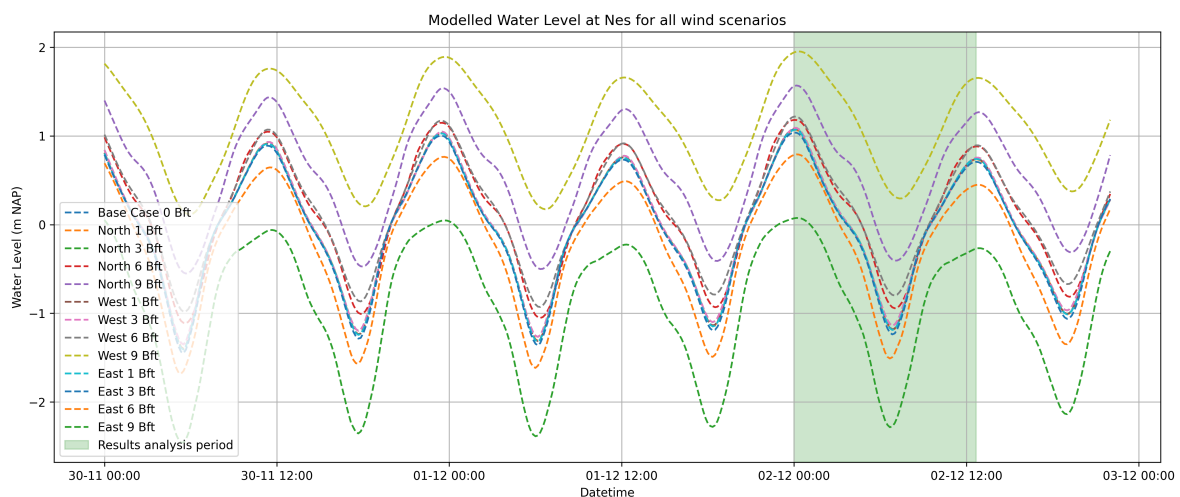
Results

This chapter addresses the main research question: **How do varying wind conditions influence the hydrodynamics on the intertidal flats in the Wadden Sea?** The results are structured in three parts: it starts with an examination of water level variations, continues with an evaluation of exposure times and exposed areas, and concludes with an assessment of flow patterns and residual currents.
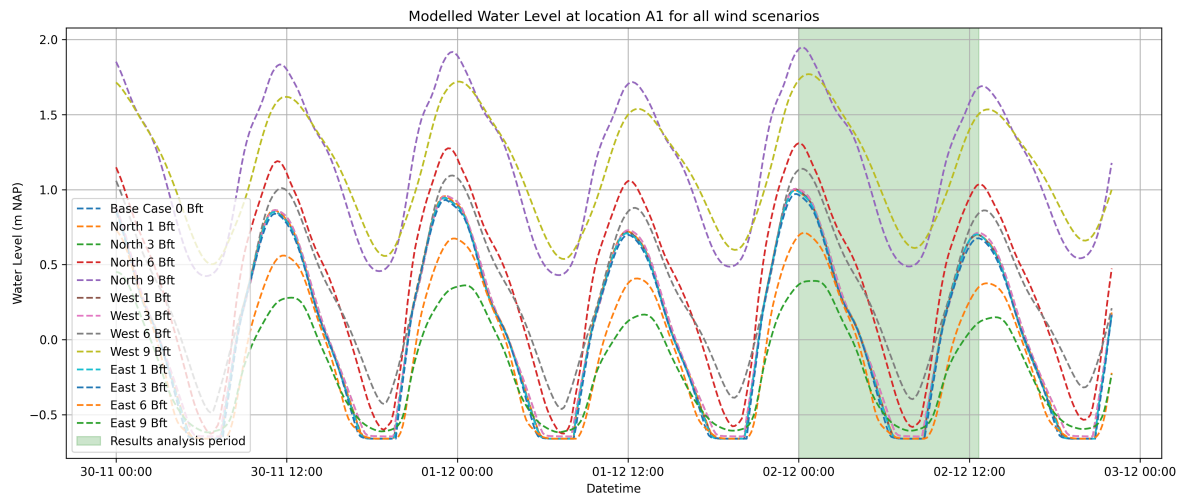
5.1. Results on water levels

First, the water levels are examined at Nes (Figure 5.1) and at the measurement locations to assess the effect of wind in both the channel and on the intertidal flats. At Nes, the 1- and 3- Beaufort scenarios align closely with the base case. Furthermore, the North-6 and West-6 scenarios also coincide, both showing a small set-up. In contrast, East-6 exhibits a set-down. In the East-9 scenario, the shape of the modelled water level curve changes noticeably. West-9 shows a larger set-up than North-9.

On the intertidal flats (Figure 5.2), at location A1, both set-up and set-down effects are more pronounced. At this location, the influence of the 9-Beaufort north wind is greater than that of the west wind. This pattern is reversed at the other measurement locations, A2 through A5, where the 9 Beaufort west wind causes a greater set-up than the north wind, consistent with the results observed in the channel at Nes. Under winds from the north and west, at both 6 and 9 Beaufort, the locations remain inundated for the entire tidal cycle.

**Figure 5.1:** Modelled water levels for all scenarios at Nes.

Figure 5.2: Modelled water levels for all scenarios at AQD location A1.

5.2. Results on exposure times

This section first presents the exposure times and highlights the base case and extreme cases of the modelled scenarios. It then examines the differences in exposure times under various wind conditions. The analysis distinguishes between the broader intertidal area of the Pinkewad, located south of Ameland, and more detailed observations at the measurement locations to offer insight at both large and small spatial scales. Exposure time and differences are evaluated over a single tidal cycle, from high water to the following high water. Only the most notable scenarios have been included in the main text; results for all wind scenarios are provided in Appendix D.

5.2.1. Base case and strong wind scenarios

The base case, representing conditions without applied wind, is shown in Figure 5.3 and provides a reference for comparison. In this figure, the darkest red areas indicate locations that are fully exposed throughout the tidal cycle, whereas the white areas remain submerged. Tidal channels are clearly visible as areas that stay wet. Around the tidal divide, where instruments were placed, a complex pattern of flow emerges due to interactions between the Ameland and Frisian inlets. A closer view of this region provides further insight.
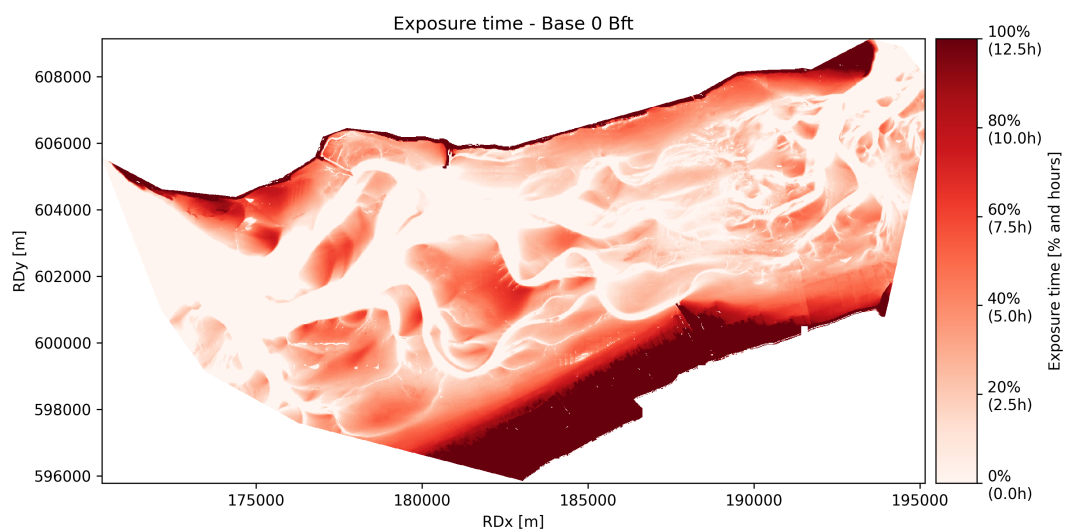

Figure 5.3: Exposure time base case scenario for 1 tidal cycle.

The most significant increases in water level are found in the scenarios with westerly and northerly winds at 9 Beaufort. As illustrated in Figure 5.4 for the westerly wind case, extensive parts of the intertidal zone remain submerged. Notably, the salt marshes between RDx=180000m and RDx=190000m, towards the bottom of the figure, are also partially submerged due to the elevated water level compared to the base case.
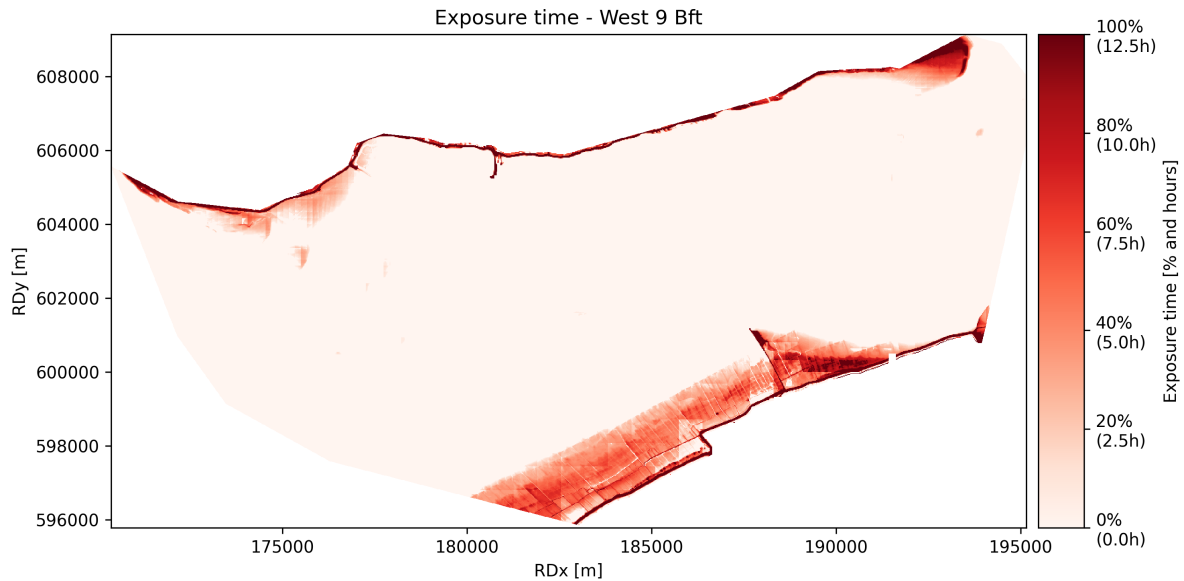

Figure 5.4: Exposure times for scenario West-9 for 1 tidal cycle.

East-9 Bft leads to very low water levels, a set-down for the majority of the map. This is shown in Figure 5.5. Around the tidal divide, the intertidal area is less exposed, whereas the south and west show an increase in the exposure times. The salt marshes, located at the bottom of Figure 5.5 in dark red, show an extension of the fully exposed area northwards. What is also notable is that the intertidal areas between the channels on the western side of the domain remain almost fully exposed, for example the area between the channels at RDx=182000m and RDy=601000m.
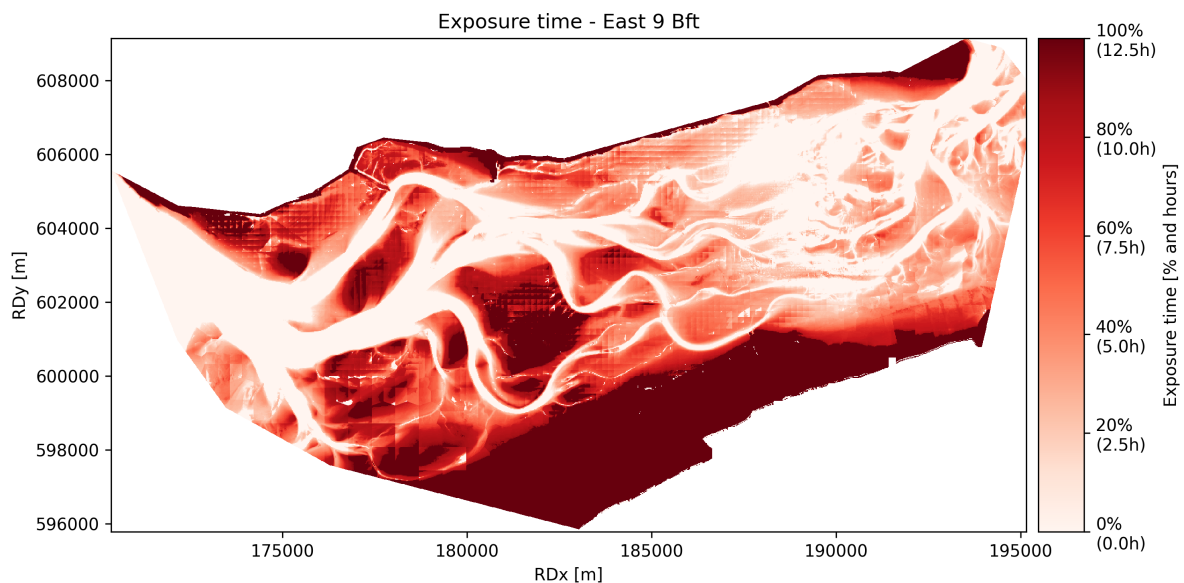
Figure 5.5: Exposure times for the East-9 wind scenario over one tidal cycle.

In scenarios with winds from the north, east, and west at 1 or 3 Beaufort, only minimal spatial variation in exposure time is observed over a tidal cycle. These differences will be discussed in more detail in the following section. In contrast, wind scenarios with 6 or 9 Beaufort result in significant deviations from the base case. The northerly wind at 6 Beaufort, shown in Figure 5.6, leads to a widespread decrease in exposure time across the entire domain and has a greater impact than the equivalent westerly wind. Interestingly, certain locations directly south of Ameland show increased exposure time, likely due to the sheltering effect of the island.
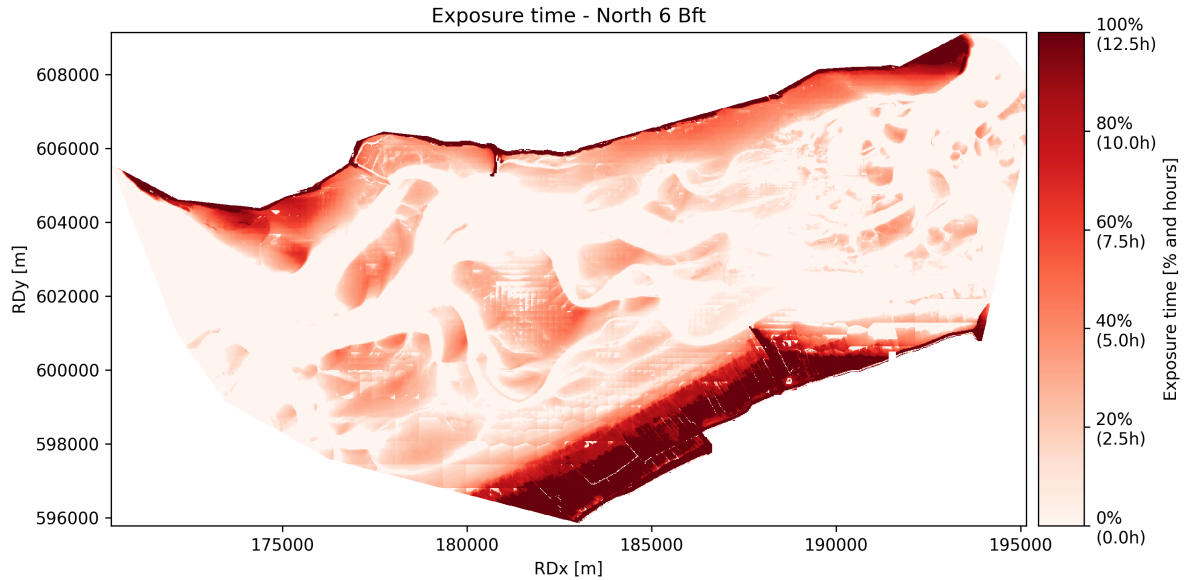

Figure 5.6: Exposure times for the North-6 wind scenario over one tidal cycle.

## 5.2.2. Quantification of exposure time differences

To better understand the effect of wind, differences in exposure time between the base case and the wind scenarios are quantified. At 1 Beaufort, wind caused minimal changes. Northerly and easterly winds resulted in a maximum difference of approximately ±3%, or ±0.3 hours, while the westerly wind produced only around 1% (0.2 hours) change. In most areas, exposure time remained unchanged.

At 3 Beaufort, greater variation was observed. The easterly wind scenario resulted in a maximum difference of 4%, while westerly and northerly winds caused differences of 7% and 8%, respectively. In the case of a westerly wind at 3 Beaufort (see Figure 5.7), changes in exposure time were spread more uniformly across the area. The northerly wind scenario, however, caused more localised effects, particularly in the south near the Frisian coast, where water appeared to accumulate. This is also visible in Figure 5.8.
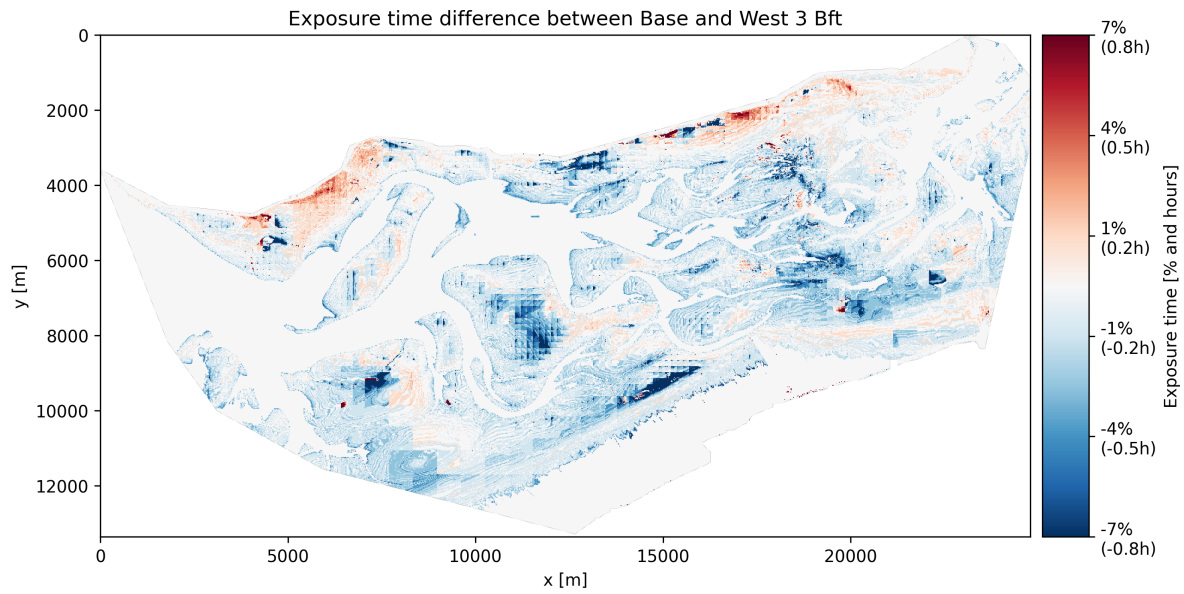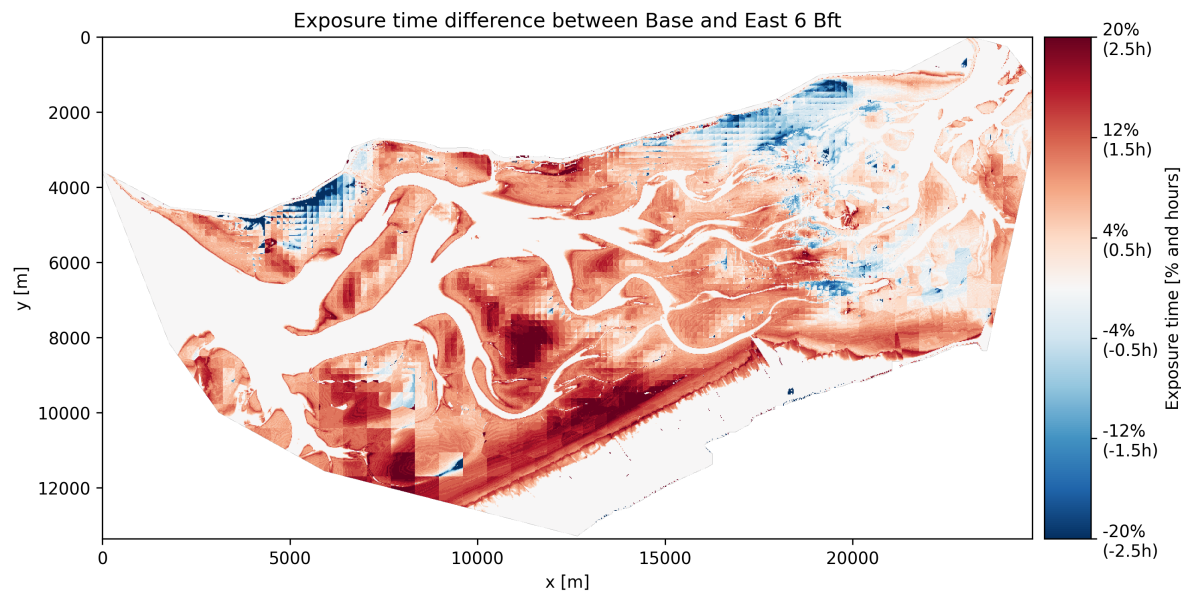
Figure 5.7: Exposure time differences for scenario West-3 compared to the base case without wind for 1 tidal cycle.
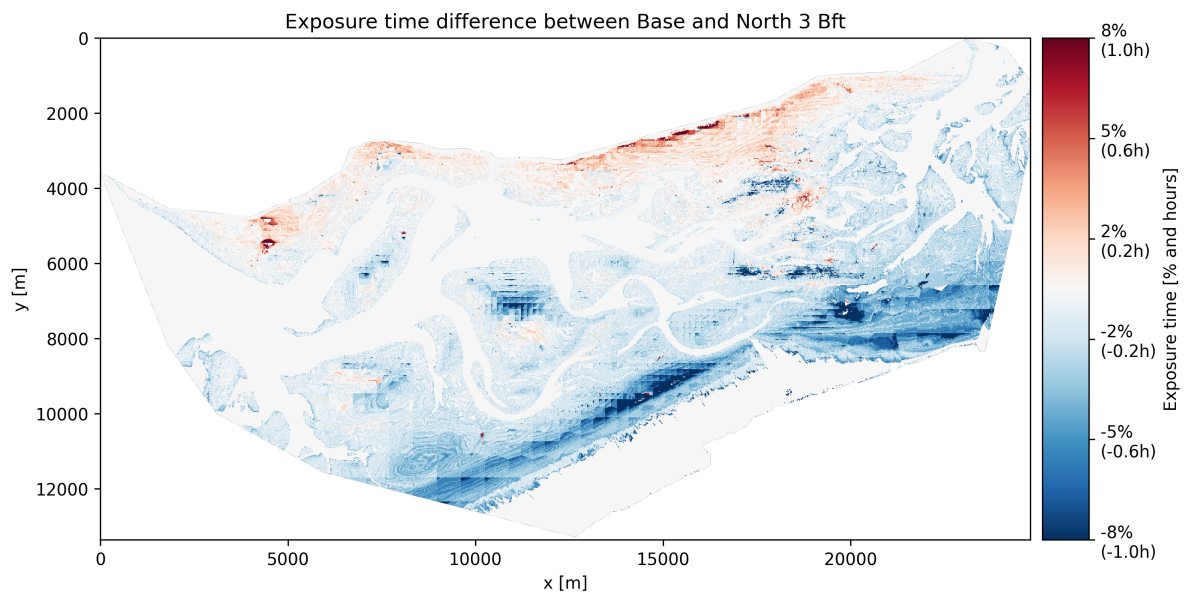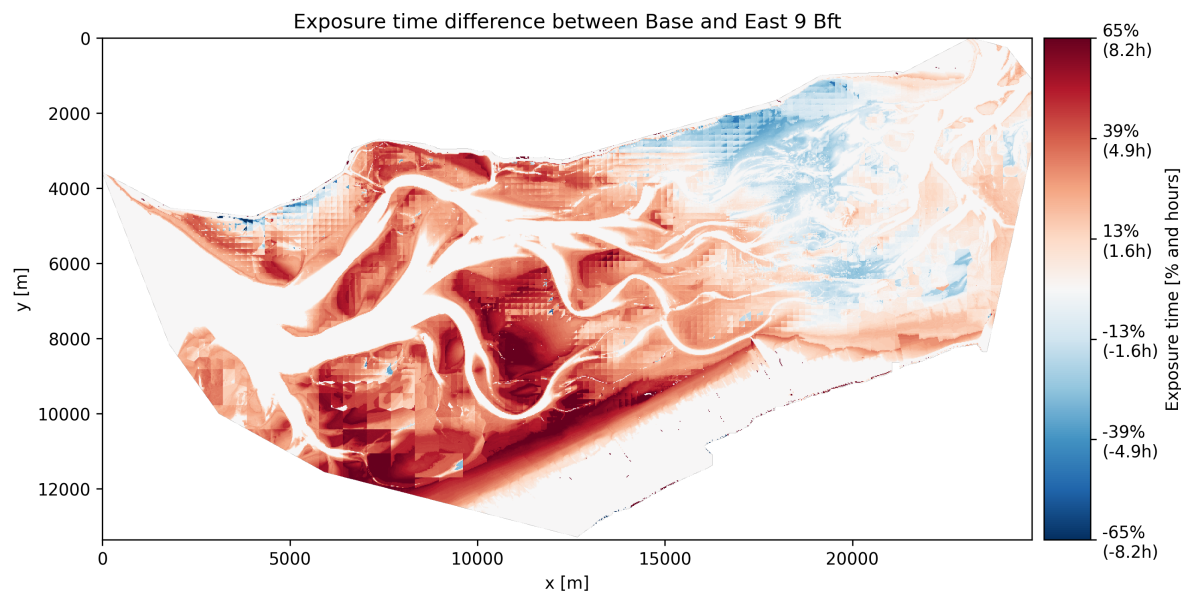

Figure 5.8: Exposure time differences for scenario North-3 compared to the base case without wind for 1 tidal cycle.

The most substantial changes in exposure time have been found in scenarios with wind speeds of 6 or 9 Beaufort, with differences ranging from 20% to 49% at 6 Beaufort. A particularly notable case is the easterly wind at 6 Beaufort (Figure 5.9). As expected, most of the area has experienced an increase in exposure time due to the opposing wind, which restricts inflow and accelerates outflow. Surprisingly, certain zones near the tidal divide have shown decreased exposure (blue areas in the figure). This pattern becomes even more pronounced in the scenario with easterly wind at 9 Beaufort, as seen in Figure 5.10, where the areas with reduced exposure expand further.

Figure 5.9: Exposure time differences for scenario East-6 compared to the base case scenario without wind for 1 tidal cycle.

Figure 5.10: Exposure time differences for scenario East-9 compared to the base case scenario without wind for 1 tidal cycle.

5.2.3. Exposure time at measurement locations

Figure 5.11 provides a closer view of the exposure time around the tidal divide, where the five measurement locations A1 to A5 are situated. These visualisations show the spatial variation in exposure under different wind conditions, particularly highlighting the influence of easterly winds. The corresponding quantitative values are summarised in Table 5.1, showing absolute exposure time in hours for each location under all simulated scenarios.

(a) Base Case (0 Bft)   **(b)** East Wind (6 Bft)   **(c)** East Wind (9 Bft)
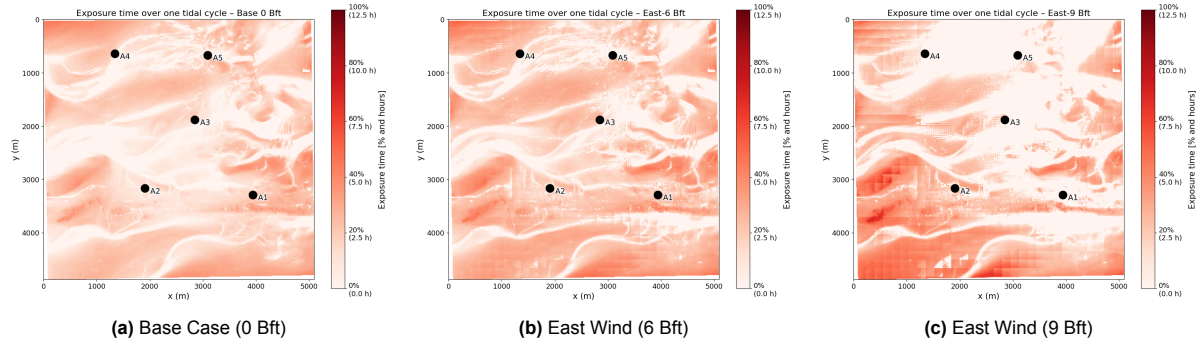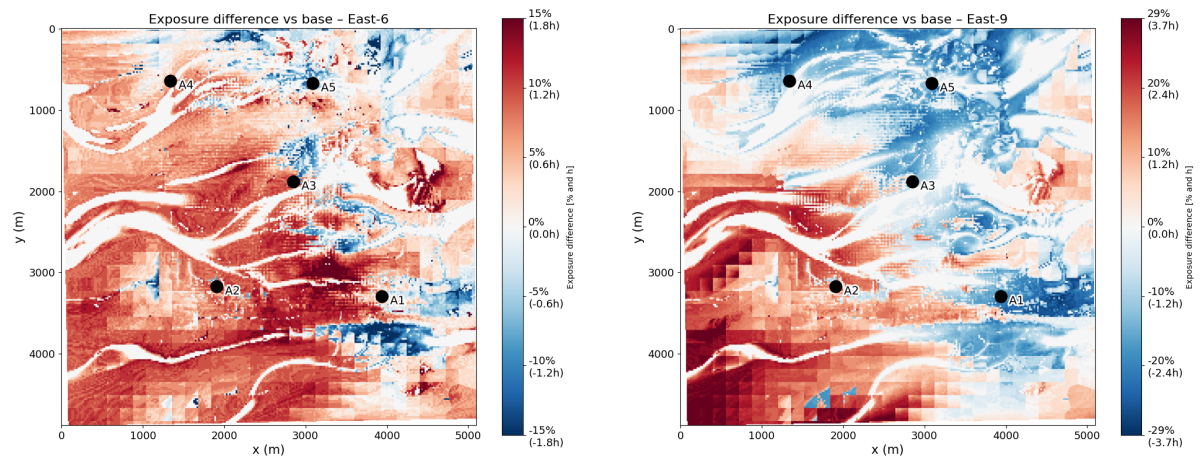
Figure 5.11: Exposure time over one tidal cycle for Base, East-6, and East-9 scenarios.

Table 5.1: Absolute Exposure Time [h] at measurement locations. Green: exposure time increase, red: exposure time decrease compared to the base case.

Scenario	A1	A2	A3	A4	A5
Base 0	**2.33**	**0.00**	**1.33**	**0.00**	**0.83**
East-1	2.33	0.00	1.50	0.00	1.00
East-3	2.50	0.00	1.67	0.00	1.00
East-6	2.50	0.00	2.67	0.00	0.00
East-9	0.00	0.00	0.00	0.00	0.00
North-1	2.17	0.00	1.33	0.00	0.67
North-3	1.83	1.00	1.50	0.00	0.50
North-6	0.00	0.00	1.17	0.00	0.00
North-9	0.00	0.00	0.00	0.00	0.00
West-1	2.33	0.00	1.33	0.00	0.67
West-3	1.67	0.00	1.33	0.00	0.33
West-6	0.00	0.00	0.00	0.00	0.00
West-9	0.00	0.00	0.00	0.00	0.00

A clear pattern has emerged in response to easterly winds. As wind strength has increased from 0 (base case) to 6 Beaufort, exposure times at A1 and A3 have increased. However, when wind strength has increased further to 9 Beaufort, exposure times at these locations have strongly decreased to zero. This trend is illustrated in Figure 5.12a and 5.12b, which show the spatial difference in exposure time between the East-6 and East-9 scenarios.

(a) Difference in exposure times between East-6 and the base case.

(b) Difference in exposure times between East-9 and the base case.

Figure 5.12: Exposure time differences around measurement locations A1-A5 over one tidal cycle for scenarios East-6 and East-9 compared to the base case scenario.

The values from Table 5.1 confirm these observations for A1 and A3:

- **A1** has an exposure time of 2.33 hours in the base case, which increases slightly to 2.50 hours under East-6, and then drops to 0.00 hours under East-9.
- **A3** follows a similar trend, increasing from 1.33 hours (Base 0) to 2.67 hours East-6), before decreasing to 0.00 hours in the East-9 scenario.

A2, however, has remained fully submerged in nearly all scenarios. The only exception is under North-1, where it is exposed for 1.00 hour. This near-complete submergence of A2 is not clearly visible in Figure 5.12. In general, locations A2 and A4 have consistently displayed nearly zero exposure times across almost all wind scenarios, indicating that they are situated in relatively low-lying areas that remain wet throughout the tidal cycle.

These local effects, already noted in the broader maps, are more apparent at this smaller scale. Figure 5.12 highlights the exposure time differences for East-6 and East-9, and the results are confirmed by the values in Table 5.1.

For wind from the north and west, local exposure time differences also appear between 3 and 6 Beaufort. At 3 Beaufort, areas of both increased (red) and decreased (blue) exposure are observed, as shown in Figure 5.13. However, at 6 Beaufort, only areas with reduced exposure remain visible. These figures are provided in the appendix.
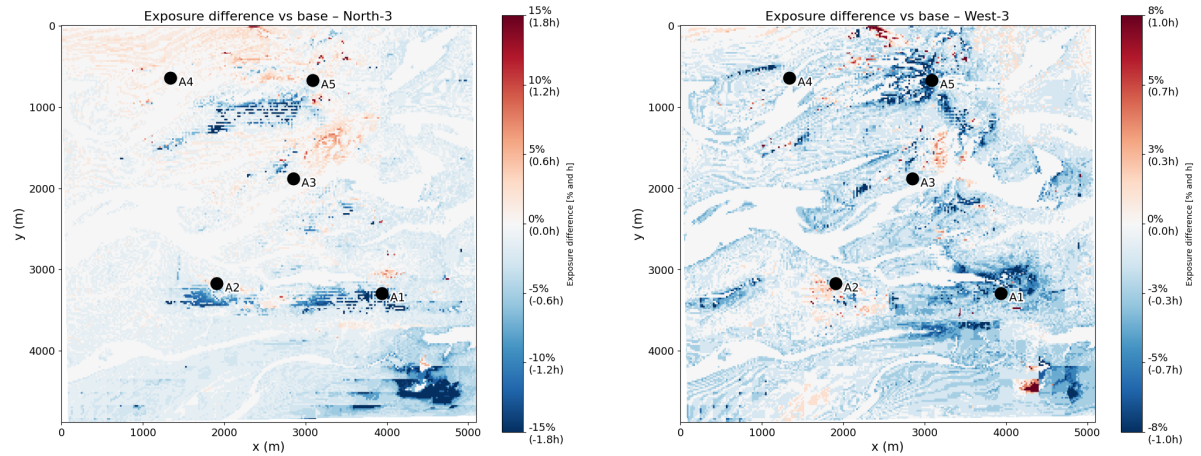
Figure 5.13: Exposure time differences around the measurement locations A1-A5 over one tidal cycle for scenarios North-3 and West-3.

Comparing 9 Beaufort scenarios from the north and west, the patterns near the measurement locations have been largely similar. A minor difference has appeared near A4, where the area to the west and north of A4 is less exposed under the westerly wind compared to the northerly wind.

5.2.4. Total exposed area
From the spatial exposure maps, it is also possible to quantify the total exposure areas across the entire Pinkewad. By comparing each wind scenario to the base case, relative differences in exposure area can be assessed. This approach provides insight into how varying wind directions and magnitudes have affected the extent and duration of intertidal exposure under different forcing conditions.

Table 5.2: Absolute exposure area and comparison to the base case.

Scenario	>0h [km²]	△ 0h [%]	>3h [km²]	△ 3h [%]	>6h [km²]	△ 6h [%]	>9h [km²]	△ 9h [%]
Base-0	135.09	0.00	90.44	0.00	39.46	0.00	24.17	0.00
East-1	135.17	0.06	90.54	0.11	39.56	0.25	24.22	0.21
East-3	136.64	1.15	92.47	2.24	40.46	2.53	24.67	2.07
East-6	141.42	4.69	108.79	20.29	50.05	26.84	28.99	19.94
East-9	139.92	3.58	122.03	34.93	78.80	99.70	56.41	133.39
North-1	134.79	-0.22	89.79	-0.72	39.15	-0.79	24.15	-0.08
North-3	133.21	-1.39	86.95	-3.86	37.04	-6.13	23.65	-2.15
North-6	102.31	-24.27	58.44	-35.38	26.12	-33.81	19.43	-19.61
North-9	40.60	-69.95	27.10	-70.04	7.22	-81.70	4.25	-82.42
West-1	134.98	-0.08	90.59	0.17	39.74	0.71	24.24	0.29
West-3	132.31	-2.06	87.45	-3.31	38.67	-2.00	24.02	-0.62
West-6	101.91	-24.56	60.72	-32.86	28.22	-28.48	21.32	-11.79
West-9	24.81	-81.63	20.05	-77.83	9.86	-75.01	4.73	-80.43

The results of Table 5.2 are presented in Figures 5.14 and 5.15, and clearly demonstrate the directional and magnitude-dependent impact of wind forcing on the exposure area. Under easterly winds, the total area exposed for >0 h remains almost unchanged, yet the surface is redistributed toward longer dry periods. In scenario East-9, the areas exposed for >6 h and >9 h increase by 100% and 133%, respectively, compared to the base case, and the mean exposure time rises non-linearly to 5.51 h (Figure 5.16 and Table 5.3).

Absolute exposure area vs wind speed
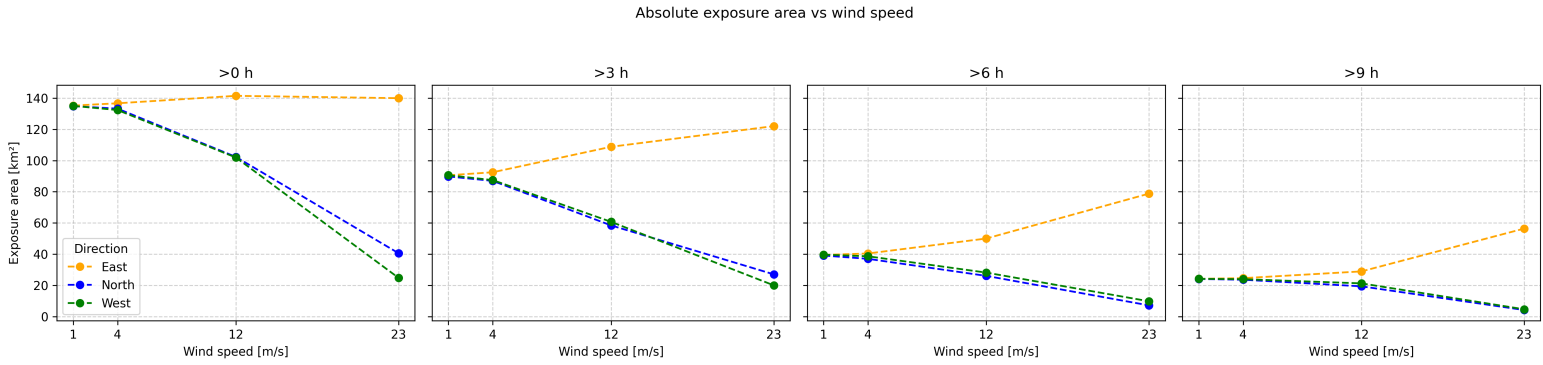
Figure 5.14: Absolute exposure areas for different wind scenarios.

Relative change of exposure area vs wind speed
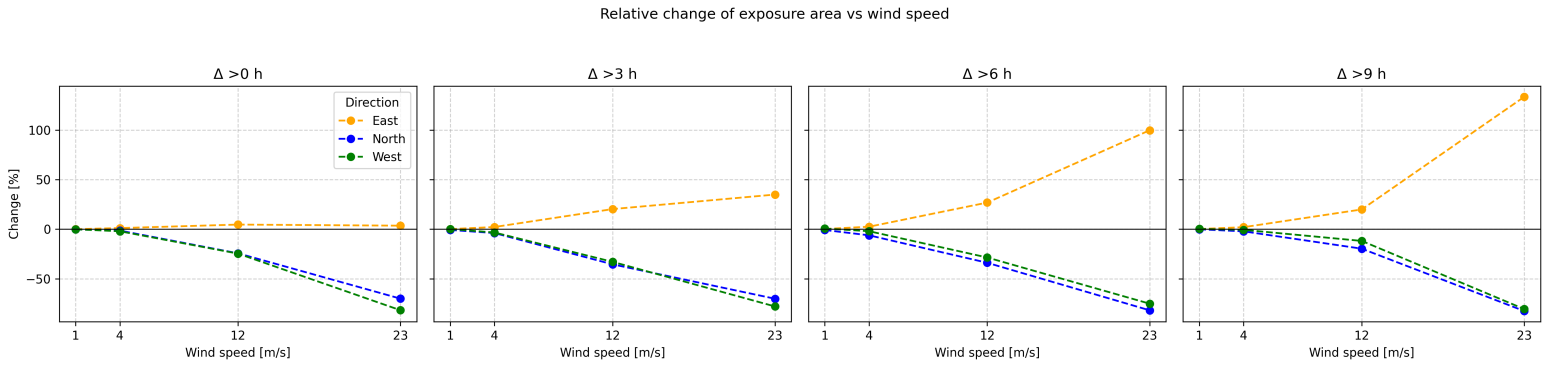
Figure 5.15: Relative exposure areas, compared to the base case, for the different wind scenarios.

Table 5.3: Average exposure time per scenario.

Scenario	Avg Exposure [h]
Base-0	3.67
East-1	3.67
East-3	3.74
East-6	4.24
East-9	5.51
North-1	3.65
North-3	3.55
North-6	2.55
North-9	0.95
West-1	3.67
West-3	3.58
West-6	2.66
West-9	0.77
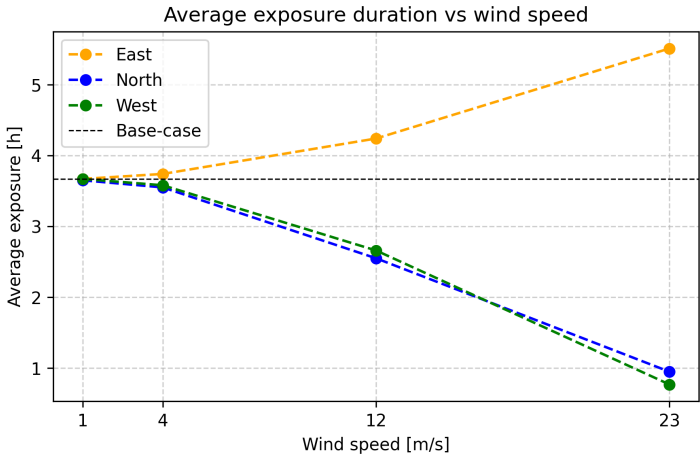
Figure 5.16: Average exposure times, for the different wind scenarios.

In contrast, northerly and westerly winds produce a nearly linear decline in exposure as wind speed increases. At 23 m/s (scenarios North-9 and West-9), the total exposed area is reduced by 70–82% across all duration classes, and the average exposure time drops to 0.95 h and 0.77 h, respectively. This confirms a significant inundation effect driven by wind set-up from these directions. It is remarkable that northerly and westerly winds have such a similar impact on exposure, despite their difference in direction. This suggests that both directions lead to comparable water level set-up across the basin.

At low wind speeds (East-1, North-1, West-1), changes are minor (less than 1%), confirming that modest winds do not lead to notable changes in set-up/set-down. Overall, the system exhibits a asymmetric behaviour: easterlies increase exposure duration, while northerlies and westerlies systematically reduce it, consistent with direction-specific wind set-up over the basin's bathymetry.

5.2.5. Ecological relevance

As stated in Chapter 2, the exposure time of 4% per year is the threshold between the sublittoral and littoral zones. The littoral zone, defined by exposure times above 4%, is further subdivided into four ecotopes: Low Littoral (4–25%), Middle Littoral (25–40%), High Littoral (40–85%), and Supralittoral (>85%). The absolute exposed area per ecotope in each of the twelve wind scenarios is provided in Table 5.4.

Table 5.4: Exposure times used for ecotope mapping as percentage of total Area. The first column, "Littoral > 4%" is subdivided into low littoral, middle littoral, high littoral and supralittoral, values are with respect to the total area.

Scenario	Littoral > 4% [%]	Low lit. [%]	Middle lit. [%]	High lit. [%]	Supralit. [%]
Base-0	69.83	24.72	18.52	15.47	11.12
East-1	70.10	24.65	18.60	15.68	11.17
East-3	70.67	24.48	19.13	15.84	11.21
East-6	73.47	18.75	22.38	20.38	11.96
East-9	72.86	10.45	15.51	24.01	22.89
North-1	69.66	24.84	18.43	15.29	11.10
North-3	68.79	25.41	18.30	14.14	10.94
North-6	52.53	23.57	12.36	8.40	8.20
North-9	20.98	7.45	7.80	3.96	1.77
West-1	69.79	24.61	18.43	15.61	11.13
West-3	68.29	24.67	17.62	14.97	11.03
West-6	52.35	22.11	12.65	8.03	9.57
West-9	12.88	2.65	3.46	4.99	1.78

The base case serves as the reference for all percentage changes discussed below. A positive change in the total littoral zone (areas exposed more than 4 % per year) is still confined to easterly wind scenarios. In particular, East-6 and East-9 increase the total littoral coverage from 69.83% to 73.47% and 72.86%, respectively. These gains are concentrated in the higher ecotopes. Under East-6, the High Littoral increases from 15.47% to 20.38% and the Supralittoral from 11.12% to 11.96%, while the Low Littoral decreases from 24.72% to 18.75%. East-9 shows an even stronger upward shift: the Supralittoral increases to 22.89% and the High Littoral to 24.01%, while the Low Littoral decreases to 10.45%. The Middle Littoral increases slightly under East-6 (from 18.52% to 22.38%) but decreases under East-9 (to 15.51%), indicating that the additional exposure under stronger easterlies is mainly concentrated at the highest elevations.

For northerly and westerly winds, the pattern reverses. Strong wind scenarios (North-9 and West-9) result in a decline across all ecotope classes: the Low Littoral decreases to 7.45% and 2.65%, the Middle Littoral to 7.80% and 3.46%, the High Littoral to 3.96% and 4.99%, and the Supralittoral

to 1.77% and 1.78%, respectively. These reductions reflect sustained inundation across the entire elevation gradient, caused by wind set-up from the north and west. Under low wind speeds (East-1, North-1, West-1), changes in ecotope distribution are minimal, typically remaining below 1% compared to the base case.

It should be noted that this study simulates exposure times over a single tidal cycle under varying wind conditions, whereas ecotope mapping is typically based on long-term exposure times averaged over a full year. In reality, wind conditions fluctuate considerably throughout the year, resulting in variable exposure durations that deviate from the average. The scenarios analysed here therefore represent idealised, spatially uniform wind cases that help isolate directional and magnitude effects, but they do not capture the full range of temporal variability observed in natural conditions.

5.3. Results on flow patterns

This section presents the results concerning flow patterns in the Pinke Wad. It begins with a visualisation of the flow at high water, where patterns under varying wind directions and wind strengths are compared. Following this, the residual current, defined as the average flow direction and velocity over a full tidal cycle of 12.5 hours, is analysed. The residual current is assessed both at fixed measurement locations (A1 to A5 and the channel near Nes), and across the full spatial domain.

5.3.1. Flow patterns at high water slack

The analysis begins with flow patterns at high water slack, the moment of flow reversal immediately following high tide. Figure 5.17 presents a quiver plot of the base case scenario. For visual clarity, the maximum depth is limited to 3 metres to highlight the intertidal flats. Inflow through the channels from the Ameland Inlet and outflow towards the Frisian Inlet are clearly visible. Flow velocities over the intertidal area south of the main Amelander channel (RDx = 177000, RDy = 599000) are relatively low. In contrast, north of this channel, around RDx = 175000 and RDy = 604000, the flow is directed oppositely.
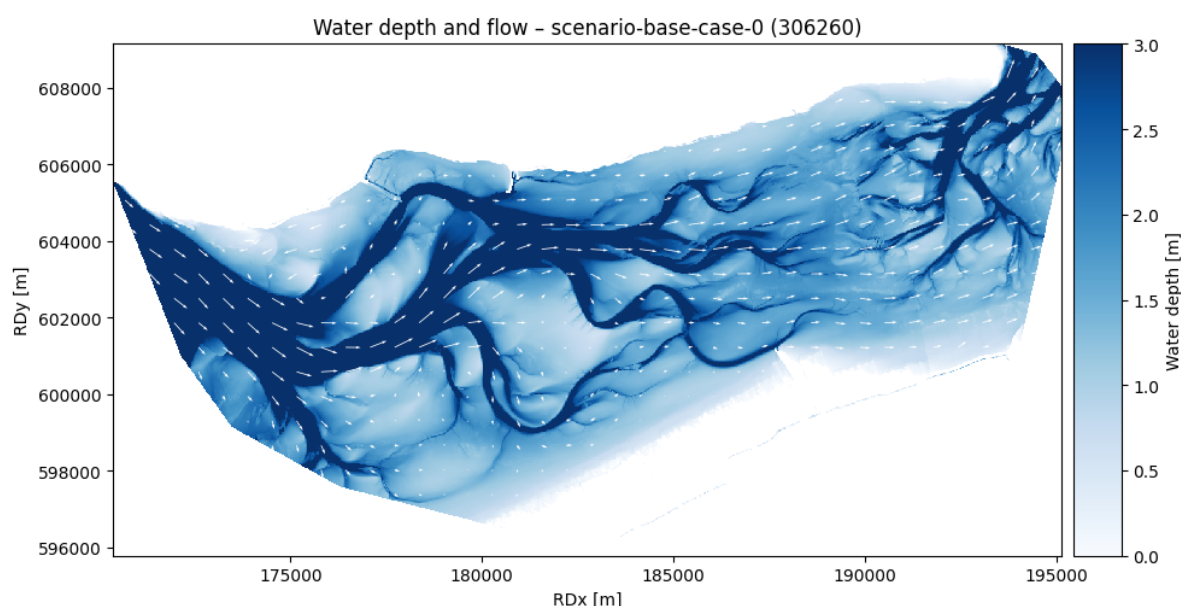

Figure 5.17: Quiver plot at HW slack for base case scenario at HW Slack at the tidal divide.

It is determined that flow reversal in the Ameland Inlet occurs approximately 30 minutes after high water at the tidal divide, where measurement locations A1 to A5 are situated. This time lag highlights spatial variability in slack water timing across the system.

### 5.3.2. Effect of wind on flow direction and magnitude

To evaluate wind effects, flow magnitudes under three wind directions are compared with the base case. For wind speeds of 1 Beaufort, quiver plots appear nearly identical to the base case for all wind directions. Since winds of 9 Beaufort from the south occur on average only once per year, results for both 1 and 9 Beaufort, along with directional comparisons for North, East, and West, are included in Appendix E.

At 3 Beaufort, flow in the main channel remains relatively stable, with only minor changes in strength. On the intertidal flats, flows under northerly and easterly winds appear stronger than in the base case, as shown by larger and more vividly coloured quivers. The West-3 scenario enhances eastward-directed flow around the tidal divide, which is visible as longer red arrows.
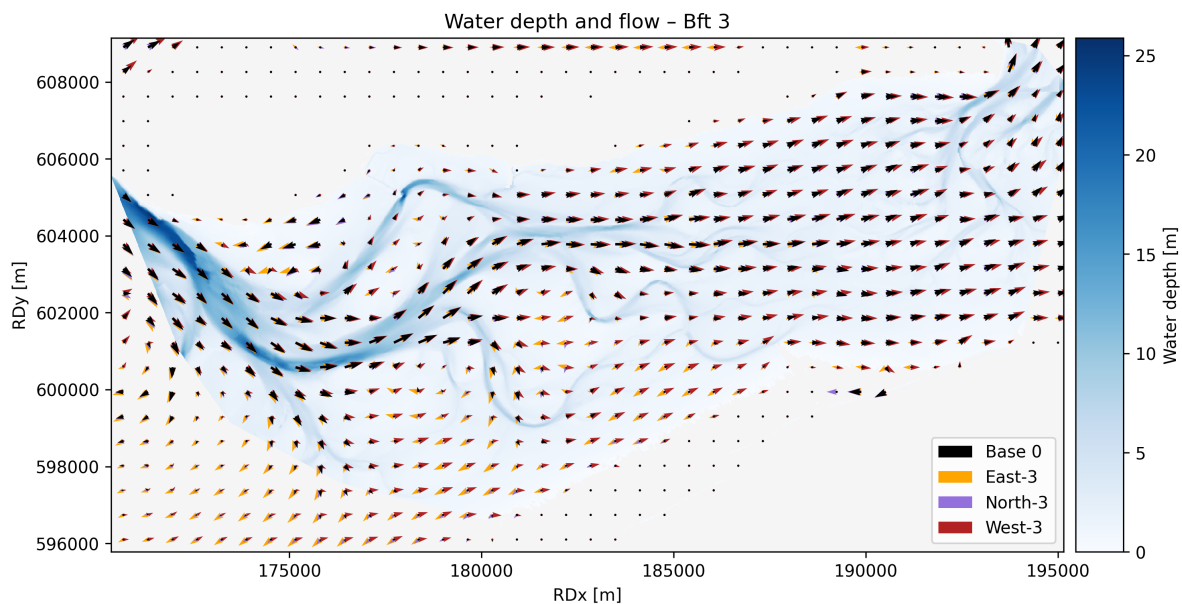
Figure 5.18: Quiver plot comparison Bft 3, water depth at HW as background.

Under 6 Beaufort conditions, flow patterns have differed significantly from lower wind scenarios. Quiver plots have shown increased velocities over both intertidal flats and channels. In East-6 and North-6, flow within the channels has decreased, while West-6 has resulted in stronger flow across most of the domain. Over the intertidal area, flow direction has also changed more markedly compared to 3 Beaufort. In North-6, flow extends onto the salt marshes (as discussed in section 5.2.1), and both East-6 and North-6 have shown opposite flow directions at the tidal divide relative to their 3 Beaufort counterparts.
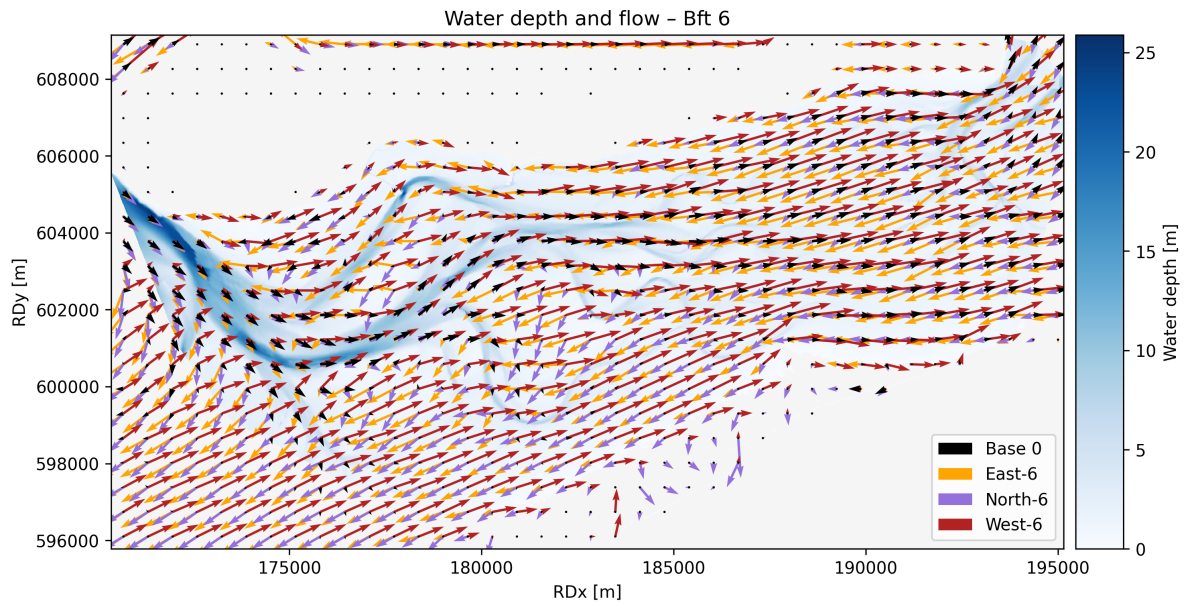
**Figure 5.19:** Quiver plot comparison Bft 6, water depth at HW as background.

5.3.3. Residual currents at fixed locations

To gain a more complete understanding of hydrodynamics, residual currents are computed for all wind scenarios at the fixed locations A1 to A5 and in the channel at Nes. Quivers in these plots have uniform lengths because the scales of the residual flows vary greatly. The actual magnitudes are annotated below each arrow.

A clear difference appears between East-1 and East-3 at the tidal divide. In East-3, the residual current direction shifts to nearly perpendicular, and in some locations becomes opposite to that in East-1 (see Figures 5.20 and 5.21). At Nes, the residual current slightly increases in East-3. In East-6, this effect is more pronounced: the residual current at Nes is 6.7 times greater than the base case, while at A1 to A5 it increases by factors ranging from 7.8 to 11.
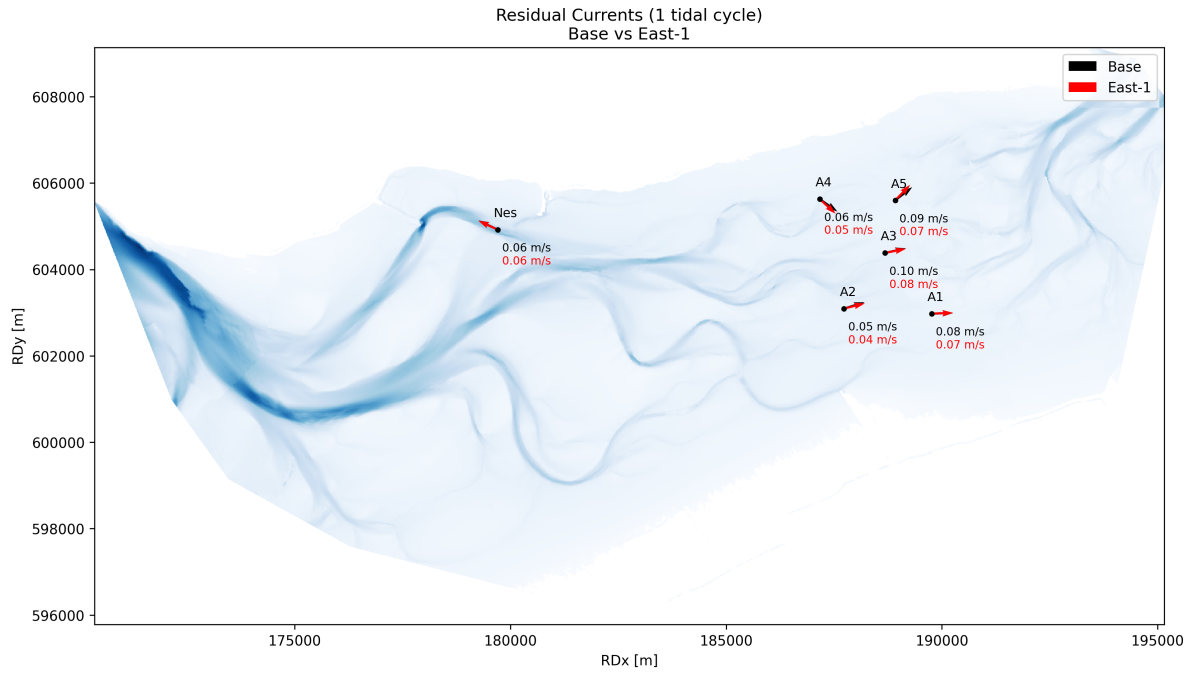
Figure 5.20: Residual currents for scenario East-1. Direction as arrows and magnitude annotated below each arrow.
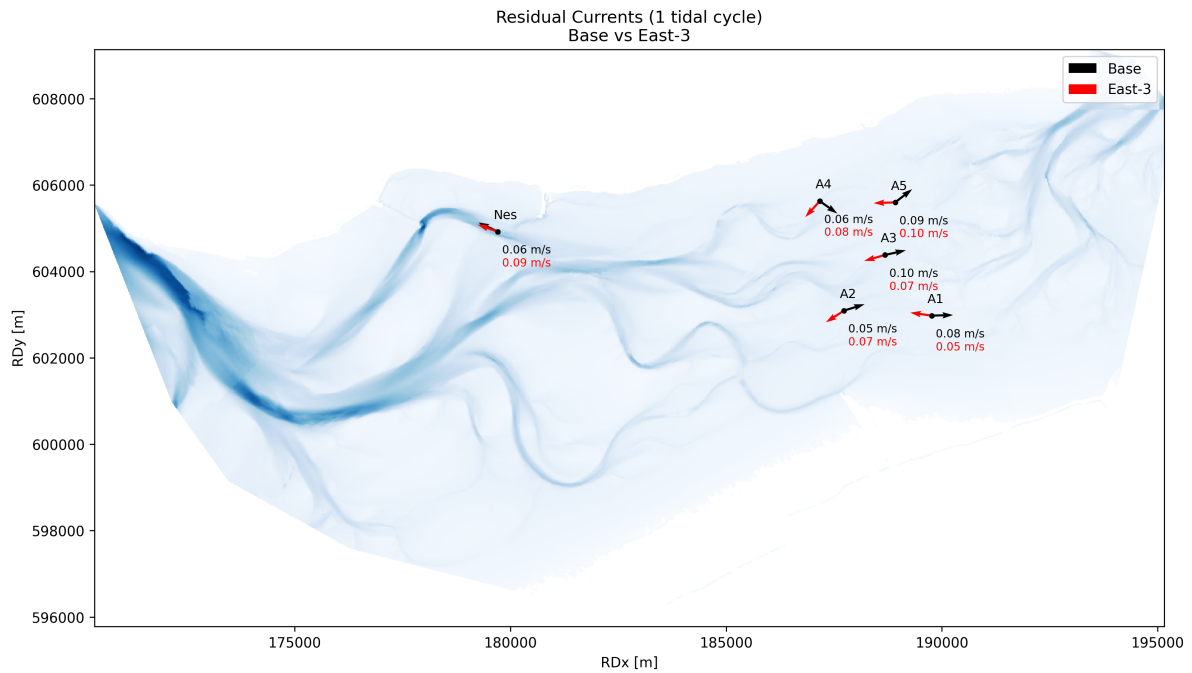
Figure 5.21: Residual currents for scenario East-3. Direction as arrows and magnitude annotated below each arrow.

A similar pattern is observed between the North-3 and North-6 scenarios (Figures 5.20 and 5.21). While North-1 shows a consistent flow direction, North-3 introduces directional changes. In North-6, flow directions shift by more than 90 degrees at most locations. The magnitude of the residual current increases to between 2.2 and 7.5 times the base case values at A1 to A5, and by a factor of 5.7 at Nes. Although the flow direction at Nes remains similar, at locations A1 to A5 it becomes nearly opposite.
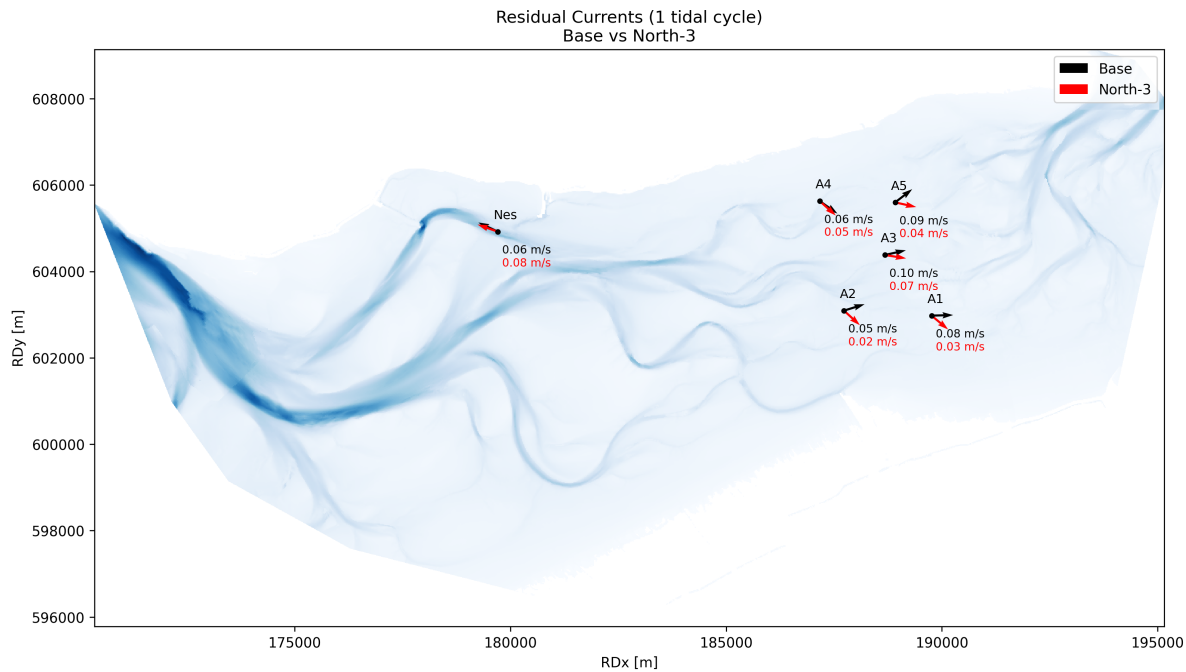
Figure 5.22: Residual currents for scenario North-3 at fixed locations.
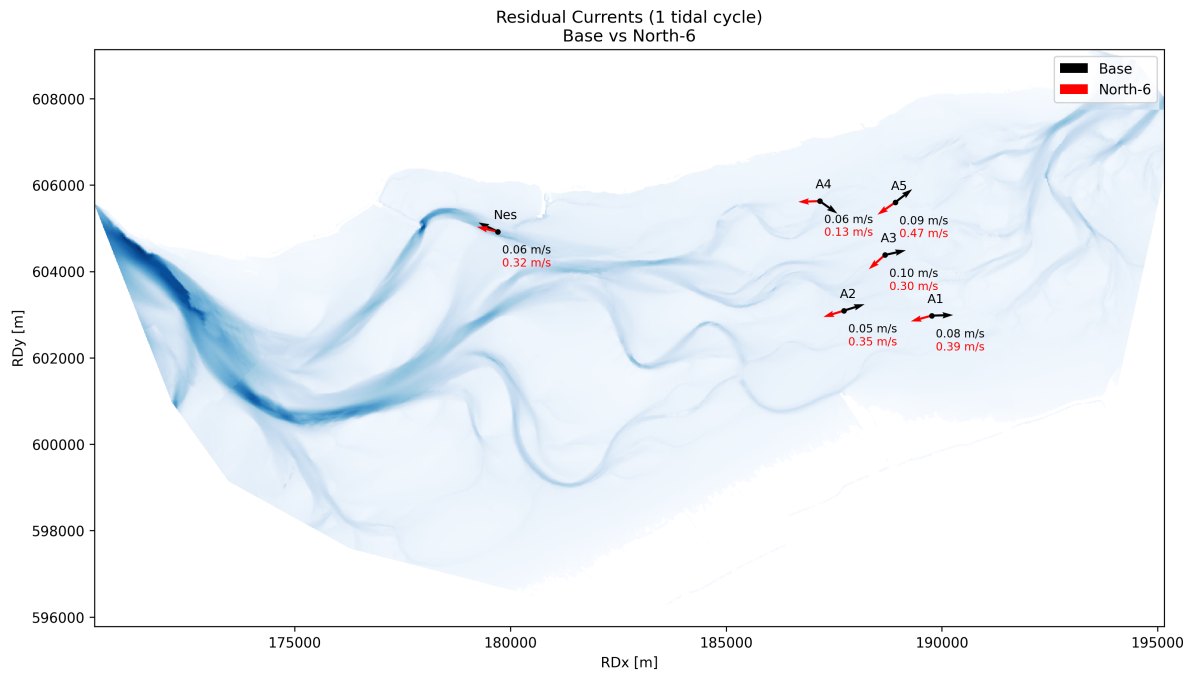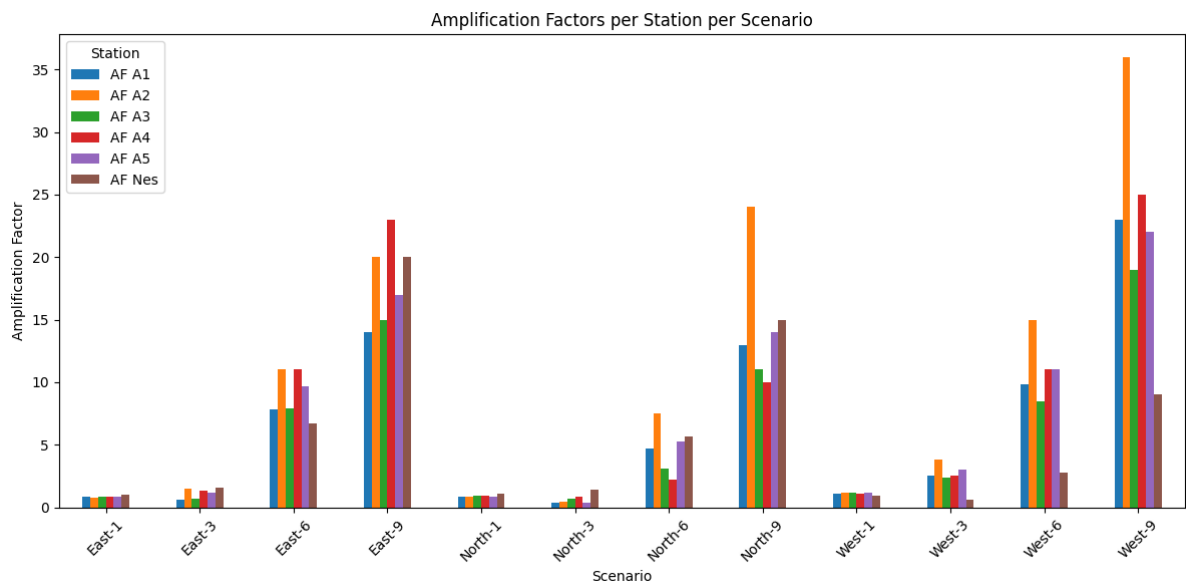

Figure 5.23: Residual currents for scenario North-6 at fixed locations.

Across all wind scenarios between 6 and 9 Beaufort, the direction of the residual flow remains relatively consistent, with variations occurring primarily in velocity. For westerly winds, the flow direction stays stable across scenarios, except at Nes, where a reversal occurs between West-1 and West-3. The amplification factor indicates how much the residual current increases compared to the base case. All amplification factors are summarised in Table 5.5, with directional changes greater than 90 degrees highlighted in grey. These results are also visualised in Figure 5.24.

Table 5.5: Amplification factors of the residual current per scenario. Values are shown in grey when the residual flow direction deviates by more than 90 degrees compared to the base case without wind.

Scenario	AF A1	AF A2	AF A3	AF A4	AF A5	AF Nes
East-1	0.86	0.77	0.84	0.85	0.85	1.00
East-3	0.61	1.50	0.69	1.30	1.20	1.60
East-6	7.80	11.00	7.90	11.00	9.70	6.70
East-9	14.00	20.00	15.00	23.00	17.00	20.00
North-1	0.86	0.89	0.93	0.93	0.84	1.10
North-3	0.34	0.46	0.69	0.88	0.40	1.40
North-6	4.70	7.50	3.10	2.20	5.30	5.70
North-9	13.00	24.00	11.00	10.00	14.00	15.00
West-1	1.10	1.20	1.20	1.10	1.20	0.94
West-3	2.50	3.80	2.40	2.50	3.00	0.58
West-6	9.80	15.00	8.50	11.00	11.00	2.80
West-9	23.00	36.00	19.00	25.00	22.00	9.00

Figure 5.24: Amplification factors of the residual currents compared to the base case scenario.

### 5.3.4. Spatial distribution of residual currents at the Pinke Wad

Residual current patterns across the entire Pinke Wad are visualised for selected wind scenarios. The base case, shown in Figure 5.25, has a mean velocity of 0.05 metres per second across the domain.
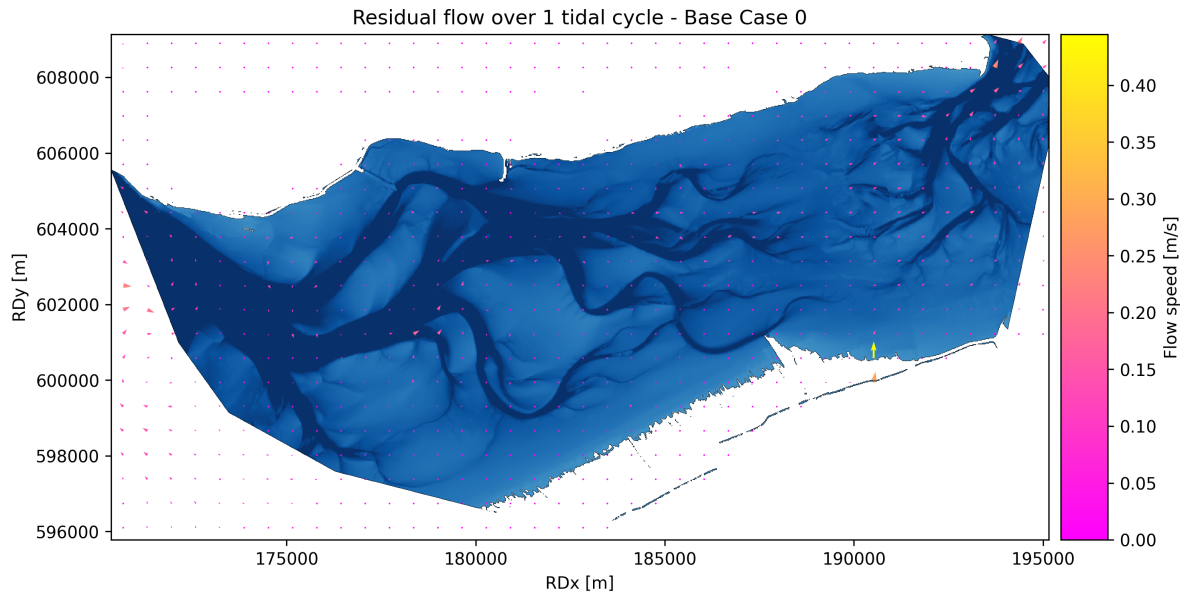
Figure 5.25: Residual flow over 1 tidal cycle for the base case scenario.

For 1 Beaufort, residual currents remain below 0.10 metres per second. Up to 3 Beaufort, most values stay below 0.20 metres per second for northerly and easterly winds, with a few exceptions: two values exceed 0.20 metres per second in West-1, three approach 0.20 metres per second in East-3, and one is observed near the Frisian Inlet in North-3. As the mean values for these scenarios are close to the base case, they are not shown in detail.

In the West-3 scenario, residual currents between 0.20 and 0.27 metres per second are observed around the tidal divide. These deviations are illustrated in Figure 5.26, where several values exceed 0.20 metres per second. Among the 3 Beaufort scenarios, West-3 exhibits the highest mean residual velocity. However, residual flow within the main channels remains close to zero.
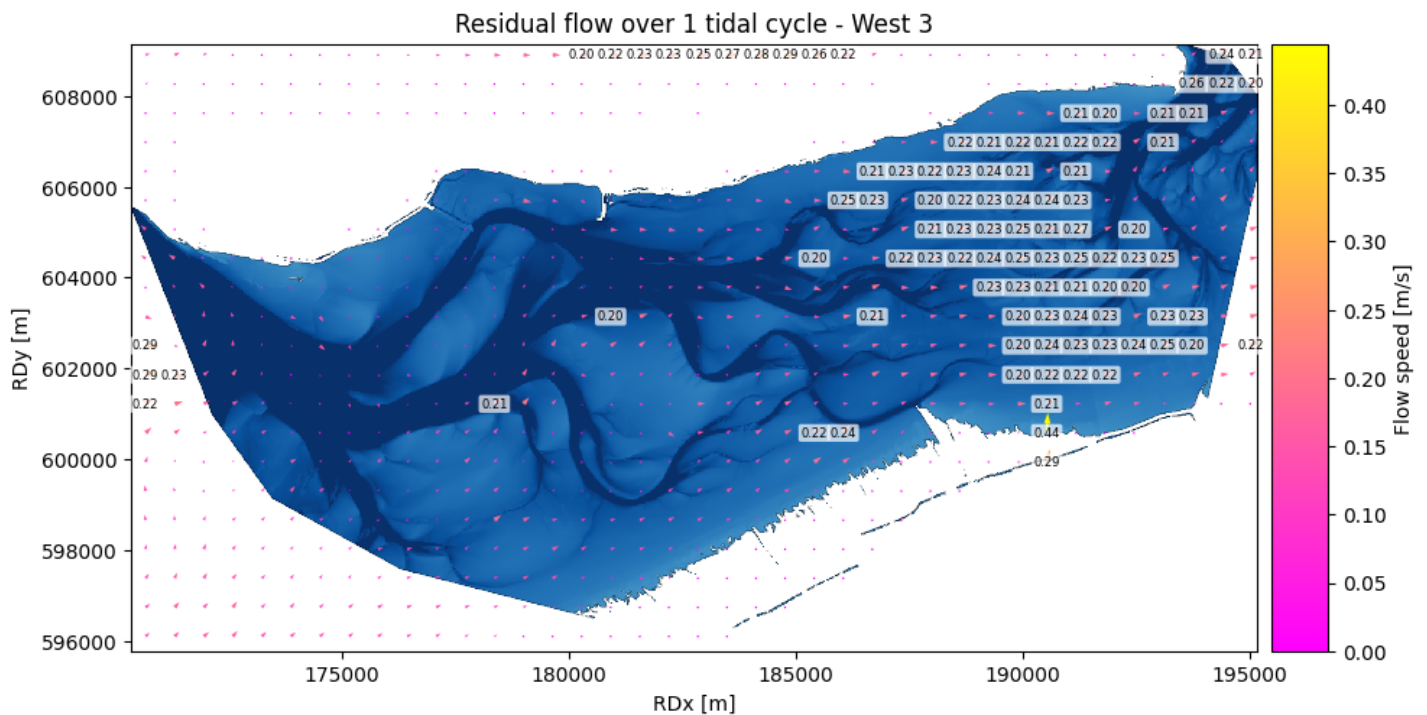
Figure 5.26: Residual flow over 1 tidal cycle for West-3 with flow velocities > 0.20m/s annotated.

Residual currents increase substantially under 6 and 9 Beaufort wind conditions. At 6 Beaufort, the mean residual velocities are 0.34 metres per second for easterly wind, 0.23 metres per second for northerly wind, and 0.44 metres per second for westerly wind. In the North-6 scenario, most values remain below 0.50 metres per second, although five outliers range between 0.53 and 0.66 metres per second. In the West-6 scenario, the majority of residual vectors exceed 0.50 metres per second. Nonetheless, in the channel extending from the Ameland Inlet towards Nes, flow magnitudes remain low and only increase after the channel branches. This pattern is clearly visible in the corresponding figures. Notably, the outflow from the Ameland Inlet is stronger under West-6 compared to both North-6 and East-6.
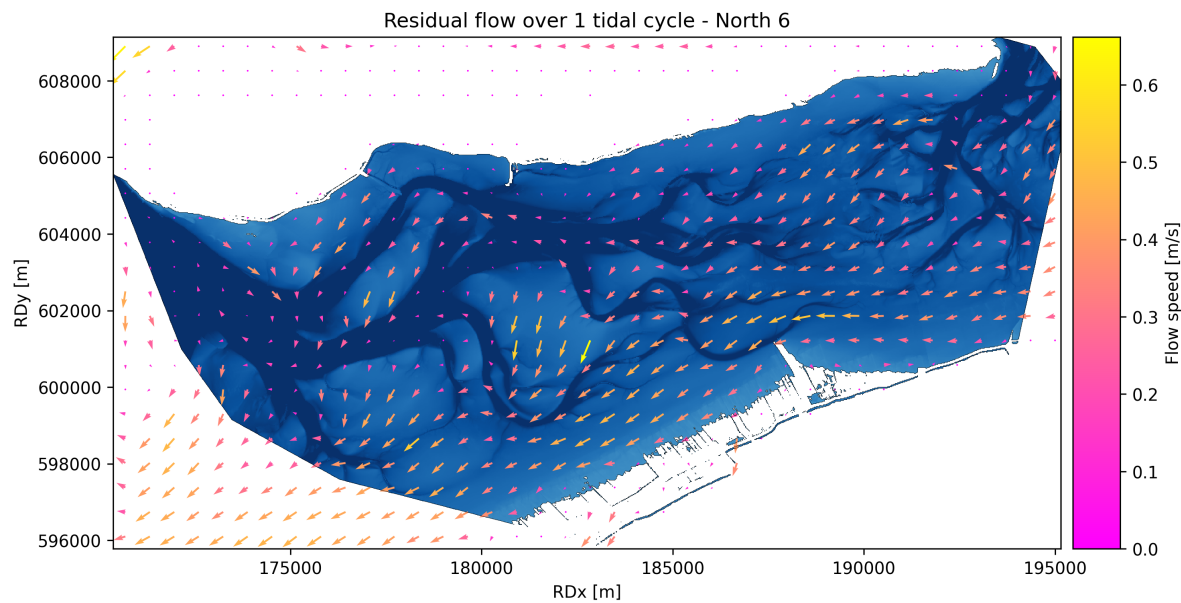
Figure 5.27: Residual flow over 1 tidal cycle for scenario North-6
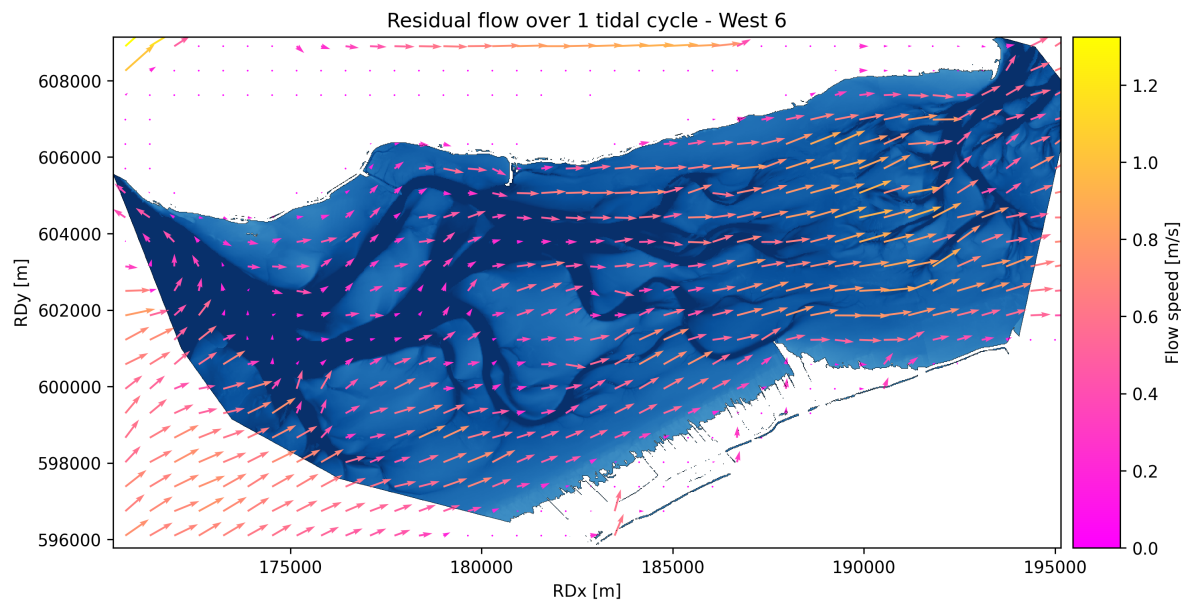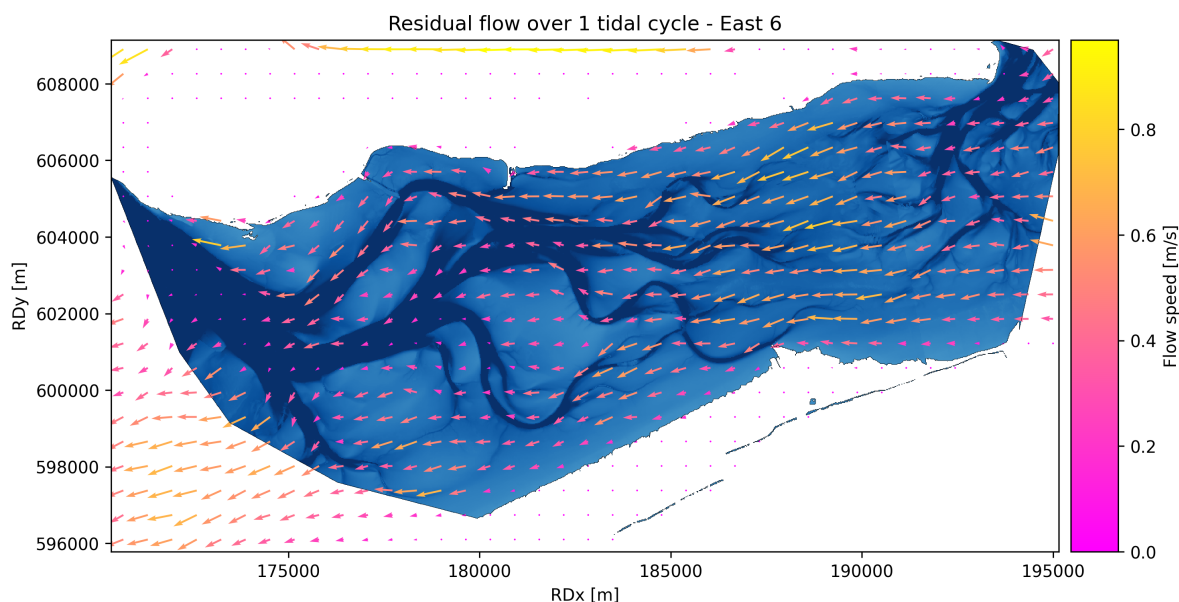

Figure 5.28: Residual flow over 1 tidal cycle for scenario West-6

Figure 5.29: Residual flow over 1 tidal cycle for scenario East-6

At 9 Beaufort, residual flow becomes increasingly dominant. The mean residual velocities are 0.55, 0.63, and 1.14 metres per second for easterly, northerly, and westerly winds, respectively. In the East-9 scenario, residual velocities exceeding 1.0 metres per second are found around the tidal divide and extend westward towards the channel at Nes. The North-9 scenario also shows values above 1.0 metres per second at the tidal divide, with flow continuing in a south-westward direction across the intertidal flats. The West-9 scenario exhibits the most extensive increase, with nearly the entire Pinke Wad displaying residual currents above 1.0 metres per second, except in the main channels.

An overview of all mean residual velocities per scenario is provided in Table 5.6.

Table 5.6: Mean residual current speed and direction per scenario.

Scenario	Mean Speed [m/s]	Mean Direction
Base Case 0	0.05	NE
East-1	0.05	N
East-3	0.08	W
East-6	0.34	W
East-9	0.55	W
North-1	0.05	NE
North-3	0.06	SW
North-6	0.23	SW
North-9	0.63	SW
West-1	0.05	NE
West-3	0.11	E
West-6	0.44	E
West-9	1.14	E

6

Discussion

This study demonstrates that wind direction and magnitude significantly influence exposure times, exposed areas, and flow dynamics on the intertidal flats of the Eastern Wadden Sea. Key findings include a quantified assessment of how exposure characteristics vary across different wind conditions, as well as the marked amplification of residual currents under stronger winds. These outcomes emphasise the pivotal role of wind-driven hydrodynamics in shaping ecotope-relevant parameters.

6.1. Discussion on data analysis

Data analysis indicates a trend in increasing water levels with higher wind speeds, particularly when the wind is blowing from the north to the south-west. In contrast, a decrease in water levels is associated with winds from the north-east to the south, particularly easterly winds. However, the correlation between magnitude and deviation is weaker for these winds from north-east to south. This relationship has only been observed at fixed locations: specifically at Nes and at measurement points A1 to A5. This dependence varies with location in the basin. However, it is not possible to determine the preceding wind and water levels for the individual points in the wind roses in Figures 3.3 and 3.4. It is possible that water levels were already influenced by prior wind patterns. These conditions may have caused water to accumulate or recede over an extended period. Consequently, higher deviations can occur even at lower wind speeds.

In addition, wind data is based on hourly observations, with each value representing the mean wind speed during the ten-minute period immediately preceding the observation time. The remaining fifty minutes of each hour are not considered, so the recorded wind speed may not accurately reflect the conditions over the whole hour. Although the measurement intervals for wind and water levels are not fully aligned, this is not expected to significantly affect the results. This is because water levels do not respond instantaneously to changes in wind speed or short-term gusts. However, this lag effect is not considered in this study when setting and resetting the values for certain wind speeds.

6.2. Discussion on model considerations

The Digital Elevation Model (DEM) is a crucial component of the 3Di model. It is important to note that the bathymetry of the Wadden Sea is highly dynamic and constantly changing due to natural morphological processes. As a result, although the DEM used provides a detailed and representative bathymetric profile, it may not fully reflect the actual state of the Wadden Sea at the time of writing. This is illustrated, for example, at measurement location A4 in Figure 4.7. The decision was made not to adjust the measurement locations to the corresponding bed levels in the DEM based on the positions measured at the time of AQD placement. This is because, in addition to the bed level, it cannot be confirmed whether the updated location accurately represents the original measurement site and its surrounding conditions at the time of data collection, because of the continuously shifting morphology.

Boundary conditions play a crucial role in the outcomes of hydrodynamic simulations. Various approaches are investigated to derive accurate water level time series at the model boundaries. In this

study, boundary water levels from the calibrated Dutch Continental Shelf Model (DCSM) (Deltares, 2022) are adopted. Nesting boundary conditions from a larger-scale model into a finer-scale model is a well-established methodology. However, a double-peak in the water level time series is observed at the western and southern boundaries. These inconsistencies resulted in deviations between simulated and observed water levels at Den Helder. For this study, two uniform Manning roughness coefficients are applied: 0.015 s/m$^{1/3}$ for the Western Wadden Sea and 0.010 s/m$^{1/3}$ for the rest of the model domain. This is different from the patched roughness map with varying roughness values used in the DCSM-model, which could be the reason for the observed discrepancies. Nonetheless, the chosen roughness distinction between the Western and Eastern Wadden Sea improved the calibration result in the 3Di model and resulted in useful model outcomes.

Validation of the DCSM-originating boundary conditions is performed by comparing the measurements of the gauge stations with the simulated water levels from the DCSM-model. An assumption is made that Mean Sea Level (MSL) is equal to Normaal Amsterdams Peil (NAP). The data from the gauge stations used in the calibration and validation phase are presented either in MSL or NAP, depending on the location of the station. The difference between MSL and NAP at sea is not constant and depends on local conditions such as tides and meteorological influences. The use of these boundary conditions in the 3Di model led to higher RMSE values (error values) in water level simulations at the gauge stations, even after calibration (Table 4.7). Notably, high water levels are consistently underestimated, and the west-boundary water level time series showed an anomalous double peak, which propagated towards Den Helder. This raises concerns about the use of these boundary conditions from one hydrodynamic model (e.g., Delft3D) in another (e.g., 3Di), especially when differences in defined roughness areas are not matched, as well as how the model deals with them. However, aligning roughness values alone is unlikely to resolve the discrepancies. It probably lies in the model schematisation setup. The models cannot be compared directly, but this was also not the aim of this study.

Regarding calibration and validation, this study focused exclusively on water levels and did not consider flow velocities or other hydrodynamic parameters. As such, it remains uncertain whether the model settings adequately represent flow dynamics. The calibrated model relied on unusually low Manning values (0.010–0.015 s/m$^{1/3}$), indicative of a hydraulically very smooth bottom. This is not representative of the Wadden Sea's seabed, which typically includes bedforms such as ripples. By comparison, DCSM-model employs roughness values ranging from 0.012 to 0.050 s/m$^{1/3}$, with typical values of 0.028 s/m$^{1/3}$ in the Western Wadden, 0.022 s/m$^{1/3}$ in the Middle, and 0.021 s/m$^{1/3}$ in the Eastern Dutch Wadden Sea (Deltares, 2022).

Calibration is also applied to the wind drag coefficient. The DCSM-model uses a wind drag formulation that varies with wind speed, based on meteorological forcing from ECMWF (Deltares, 2022). In contrast, the 3Di model uses a fixed drag coefficient. Earlier DCSM-model versions, which used HIRLAM forcing, applied a coefficient of 0.0025 [-]. The calibrated value in this study, 0.004 [-], is relatively high in comparison.

6.3. Discussion and interpretation of the results

In general, easterly winds increase exposure time and residual flow in a way that promotes drying of intertidal flats. This is particularly evident under stronger winds (6 and 9 Beaufort), where the reduction in water levels due to wind-induced set-down creates expansive and prolonged exposure, particularly in the higher ecotopes. Conversely, westerly and northerly winds increase water levels via wind set-up, leading to prolonged submergence and drastically reduced exposure.

Flow patterns over the intertidal flats began to diverge noticeably at 3 Bft and intensified by 6 Bft: northerly and easterly winds drove a net westward residual flow, whereas westerly winds produced an eastward residual current. It would be valuable in future studies to identify the exact wind direction and magnitude between north and west at which the residual current flips over during a single tidal cycle.

It is important to acknowledge that the model calibration resulted in a consistent underestimation of high water levels, particularly at the western boundary (see Section 4.3.3). This discrepancy likely caused exposure times and exposed areas to be overestimated in all wind scenarios. If the model had reproduced observed high water levels more accurately, the tidal range would be larger, with higher peaks during flood. Consequently, less of the intertidal area would become exposed, and the expo-

sure duration for many grid cells would have been shorter. This implies that the current estimates of ecotope area, particularly in the upper intertidal zones, are likely conservative. Future improvements in boundary forcing and roughness calibration would help refine these predictions, and better align the exposure-based ecotope maps with observed classifications. However, the comparison between wind directions and magnitude is relative and therefore the changes in set-up/set-down are still useful.

de Vet et al. (2018) stated: "Wind speeds of order 40 times the typical tidal flow velocity are sufficient to completely alter the flow direction and magnitude on an intertidal shoal. This has significant consequences for the sediment transport patterns." Although this study did not investigate a specific threshold value for altering the velocity signal on the tidal flats, the results (Figure 5.21) show that scenario East-3 modified the velocity signal at locations A1–A5 under a wind speed of 4 m/s. In our study, this resulted in residual flow velocities 40 to 66.7 times greater than the tidal velocity (averaged over 1 cycle) without wind, which is of the same order of magnitude as reported by de Vet et al. (2018).

The results in this research are focused on the last tidal cycle of the simulated period, approximately 2 days after spring tide. It is expected to have less exposed area if the period would be chosen around neap tide, since lower waters are higher. During spring tides the effect of the trough is larger than the crest of the tide. Therefore larger exposure times are expected. Sediment transport scales with a certain velocity power (Bosboom & Stive, 2023). Residual flow velocities tend to increase significantly from 3 to 6 Bft on the flats, influencing the sediment path particles dependent on the direction of the wind.

Combining the exposure time differences and quiver plots for East-6 and East-9, large residual currents are observed starting from the east-side Frisian inlet to the west, while the Ameland Inlet still shows very small to zero residual currents. This suggests that water is moving to the next sub-basin instead through the inlet, which may result in a set-down west of the tidal divide. The increasing set-up around and partly easterly of the tidal divide for stronger eastern winds can be a result of a larger water runoff westerly from the divide, see Figure 6.1. The bathymetry map confirms higher bed elevations at the tidal divide.
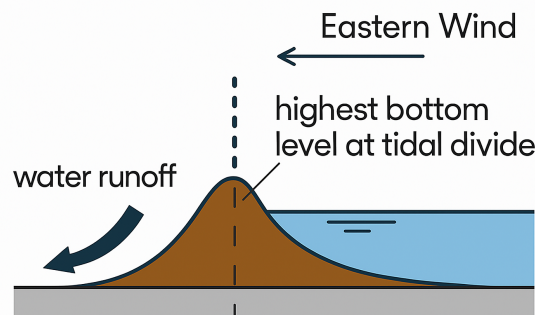
Figure 6.1: Interpretation of the water set-up at the tidal divide for stronger Eastern winds.

6.4. Climatological context of the modelled wind scenarios

Figures 6.2 and 6.3 show how frequently each wind sector and Beaufort class occurs in the long-term reference climate (1991–2020) and in a recent full year (2023) when the measurements were taken. The visual differences are quantified in Table 6.3, which reports the percentage-point change in each bin between the two periods. Additionally, Table 6.4 gives a compact comparison across four years (2021–2024), summarising changes in the occurrence of North, East, and West winds at selected Beaufort levels of the scenarios.
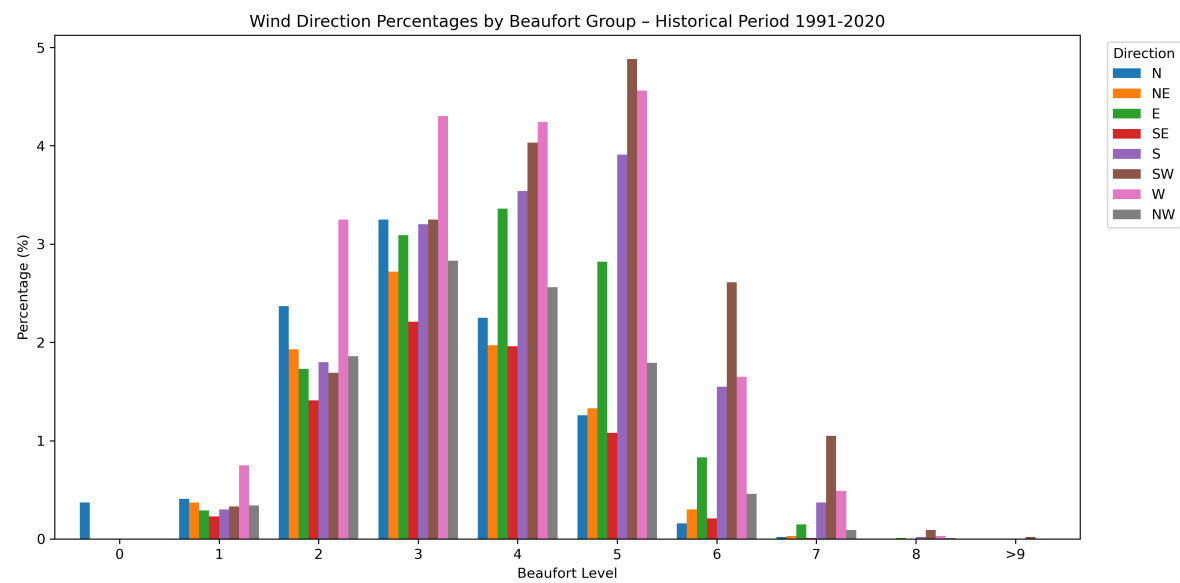
Figure 6.2: Wind direction percentages by Beaufort group for the historical period (1991–2020).
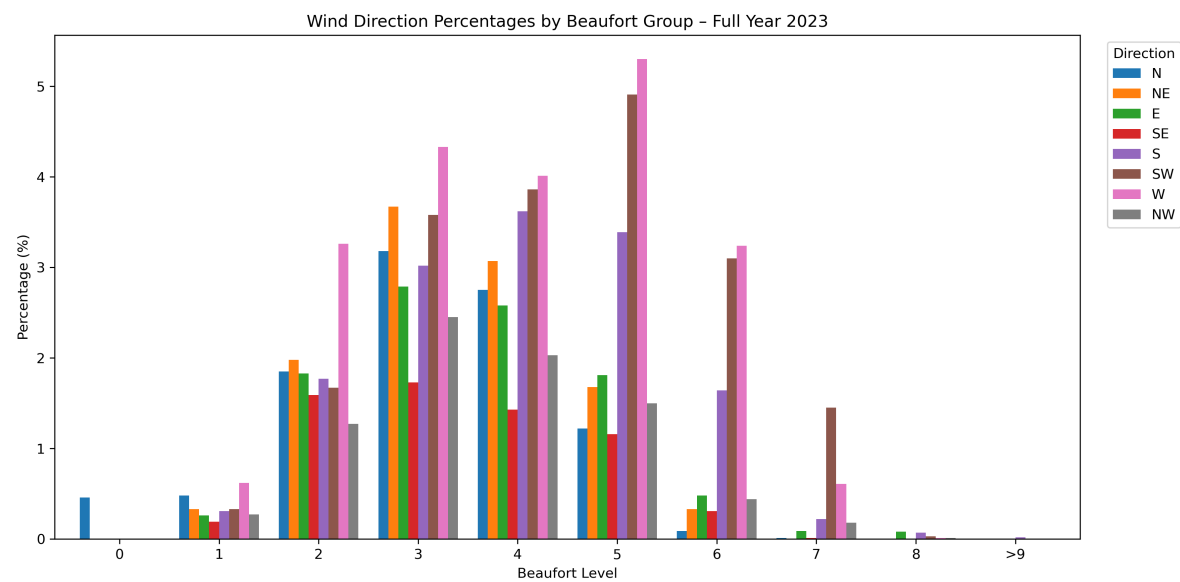

Figure 6.3: Wind direction percentages by Beaufort group for the full year 2023.

Table 6.1: Wind direction percentages by Bft group — Historical period

BFT Group	N	NE	E	SE	S	SW	W	NW
0	0.37	0.00	0.00	0.00	0.00	0.00	0.00	0.00
1	0.41	0.37	0.29	0.23	0.30	0.33	0.75	0.34
2	2.37	1.93	1.73	1.41	1.80	1.69	3.25	1.86
3	3.25	2.72	3.09	2.21	3.20	3.25	4.30	2.83
4	2.25	1.97	3.36	1.96	3.54	4.03	4.24	2.56
5	1.26	1.33	2.82	1.08	3.91	4.88	4.56	1.79
6	0.16	0.30	0.83	0.21	1.55	2.61	1.65	0.46
7	0.02	0.03	0.15	0.01	0.37	1.05	0.49	0.09
8	0.00	0.00	0.01	0.00	0.02	0.09	0.03	0.01
>9	0.00	0.00	0.00	0.00	0.00	0.02	0.00	0.00

Table 6.2: Wind direction percentages by Bft group — Year 2023

BFT Group	N	NE	E	SE	S	SW	W	NW
0	0.46	0.00	0.00	0.00	0.00	0.00	0.00	0.00
1	0.48	0.33	0.26	0.19	0.31	0.33	0.62	0.27
2	1.85	1.98	1.83	1.59	1.77	1.67	3.26	1.27
3	3.18	3.67	2.79	1.73	3.02	3.58	4.33	2.45
4	2.75	3.07	2.58	1.43	3.62	3.86	4.01	2.03
5	1.22	1.68	1.81	1.16	3.39	4.91	5.30	1.50
6	0.09	0.33	0.48	0.31	1.64	3.10	3.24	0.44
7	0.01	0.00	0.09	0.01	0.22	1.45	0.61	0.18
8	0.00	0.00	0.08	0.00	0.07	0.03	0.01	0.01
>9	0.00	0.00	0.00	0.00	0.02	0.00	0.00	0.00

Table 6.3: Change in wind direction percentages from historical to 2023 (2023 – historical)

BFT Group	N	NE	E	SE	S	SW	W	NW
0	+0.09	0.00	0.00	0.00	0.00	0.00	0.00	0.00
1	+0.07	−0.04	−0.03	−0.04	+0.01	0.00	−0.13	−0.07
2	−0.52	+0.05	+0.10	+0.18	−0.03	−0.02	+0.01	−0.59
3	−0.07	+0.95	−0.30	−0.48	−0.18	+0.33	+0.03	−0.38
4	+0.50	+1.10	−0.78	−0.53	+0.08	−0.17	−0.23	−0.53
5	−0.04	+0.35	−1.01	+0.08	−0.52	+0.03	+0.74	−0.29
6	−0.07	+0.03	−0.35	+0.10	+0.09	+0.49	+1.59	−0.02
7	−0.01	−0.03	−0.06	0.00	−0.15	+0.40	+0.12	+0.09
8	0.00	0.00	+0.07	0.00	+0.05	−0.06	−0.02	0.00
>9	0.00	0.00	0.00	0.00	+0.02	−0.02	0.00	0.00

Table 6.4: Change in North, East, and West wind percentages compared to the historical period.

Year	Direction	Δ BFT 1	Δ BFT 3	Δ BFT 6	Δ BFT >9	Δ Total
2021	North	+0.22	+2.00	−0.15	0.00	**+2.07**
	East	−0.04	−0.31	−0.46	0.00	**−0.81**
	West	+0.23	−0.22	−0.51	0.00	**−0.50**
2022	North	+0.02	+0.35	−0.02	0.00	**+0.35**
	East	0.00	−0.39	−0.29	0.00	**−0.68**
	West	+0.31	−0.49	−0.29	+0.06	**−0.41**
2023	North	+0.07	−0.07	−0.07	0.00	**−0.07**
	East	−0.03	−0.30	−0.35	0.00	**−0.68**
	West	−0.13	+0.03	+1.59	0.00	**+1.49**
2024	North	+0.07	−1.18	−0.09	0.00	**−1.20**
	East	0.00	−0.51	−0.09	0.00	**−0.60**
	West	+0.08	−0.10	−0.05	0.00	**−0.07**

A key finding is that strong easterlies (≥6 Bft), which in our model result in extensive drying and strong residual flows, are climatologically rare. They occur less than 1% of the time in both the historical dataset and in 2023. Thus, the modelled East-6 and East-9 scenarios represent high-impact but low-frequency events. The trend across recent years also shows a decline in the frequency of easterly winds (Table 6.4).

By contrast, strong westerly winds, especially at 6 Bft, became more frequent in 2023, showing a +1.59% increase relative to the long-term average. This aligns with a broader regime shift visible in Table 6.4, which confirms a recent decline in easterly occurrences and an increase in westerly wind energy. These results are consistent with projected increases in westerly storm frequency under climate change scenarios (Sterl et al., 2015). In our model, these westerlies lead to water level set-up, prolonged submergence, and reduced exposure time, particularly in the western and southern parts of the basin. This suggests that if the observed shift in wind direction persists, the intertidal flats may experience less frequent and shorter drying periods in the future.

Moderate winds (3–4 Bft) dominate the climatology. Their bars in Figures 6.2 and 6.3 are an order of magnitude taller than those of the storm-force winds. Although individual events at 3 Bft are relatively gentle, their frequent occurrence, approximately once every ten days, may give them a substantial cumulative impact. In the model, the first signs of residual current reversal appear between 3 and 6 Bft. This suggests that even under typical wind conditions, the direction and strength of residual currents on the flats are actively shaped by moderate wind forcing.

It is also remarkable that for increasing wind speeds from the north and west above 3 Bft, the exposure time and residual flow patterns increase almost linearly. This is unexpected, as wind stress scales with the square of wind velocity. A likely explanation is that the response is constrained by the basin's bathymetry or the dominant effect of friction.

Inter-annual variability, as highlighted in Table 6.4, may also influence yearly transport volumes. For example, in 2021, a strong increase in moderate northerlies was observed, which may have enhanced residual transport to the west in this basin. In contrast, 2024 saw a significant drop in northerly wind frequencies, potentially leading to a decrease in such transport.

Overall, these climatological insights help contextualise the modelled scenarios. The easterly cases illustrate rare but influential increased exposure, while the westerly cases reflect more common but submergence-dominated conditions. The dominant role of moderate winds reinforces the relevance of the 3 and 4 Bft simulations to everyday sediment dynamics in the Ameland basin. Future studies should extend this analysis with projected climate data to anticipate how changes in wind climatology may reshape intertidal exposure patterns for longer periods.

6.5. Discussion on ecotope mapping

According to the updated ecotope mapping methodology described by Rijkswaterstaat (2023a), flow velocities used as input for the current Wadden Sea ecotope map are derived from the Dutch Wadden Sea Model (DWSM), implemented in Delft3D Flexible Mesh (FM). A 2D version of this model with approximately $100 \times 100\,\mathrm{m}$ resolution is applied in the area of interest. Flow velocities are extracted from two representative spring-neap tidal periods and processed per grid cell using the 99th percentile of depth-averaged velocities, which is interpreted as the maximum flow speed. These values are interpolated onto a regular $100 \times 100\,\mathrm{m}$ output grid. Although this method provides relatively high spatial resolution, particularly shallow intertidal areas still suffer from inaccuracies due to unresolved small-scale bathymetric features. Likewise, the exposure-time maps, also essential for ecotope classification, are generated using the InterTides tool, which estimates water levels via interpolation across the domain. Although no comparison was made in this study between InterTides and a hydrodynamic approach, it may be valuable in future work to assess the potential of well-calibrated hydrodynamic subgrid models for exposure mapping. This is especially relevant as this study highlights strong temporal variability in exposure times and flow patterns due to wind effects. Such models could more accurately capture flooding and drying dynamics in shallow areas while maintaining relatively low computational costs, offering improved inputs for ecotope mapping.

7

Conclusions

This study examined the hydrodynamic response of the Wadden Sea's intertidal flats between Ameland and Holwerd to varying wind conditions, using a high-resolution subgrid hydrodynamic model, 3Di. The model was calibrated and validated using data from Aquadopp Profiler instruments and Rijkswaterstaat gauge stations. Results from twelve wind scenarios, along with one windless base case, provided insights into flow patterns, exposure times and areas, and the implications for ecotope mapping. The following conclusions are drawn for the different research questions:

How do varying wind conditions influence the hydrodynamics on the intertidal flats in the Wadden Sea?

Varying wind conditions have a substantial and spatially differentiated impact on the hydrodynamics of the Wadden Sea's intertidal flats. The direction and magnitude of wind forces directly influence water levels, residual currents, and exposure durations. Moderate to strong winds (≥3 Beaufort) induce pronounced shifts in flow direction and significantly increase residual current velocities by up to 36 times compared to windless conditions.

Easterly winds tend to lower water levels (set-down), leading to longer exposure times and drying of intertidal flats. However, near the tidal divide, increasing easterly winds did not cause a set-down. In contrast, westerly and northerly winds increased water levels (set-up), reducing exposure and enhancing submergence.

1. Which hydrodynamic parameters are essential for calibrating and validating a hydrodynamic model?

The calibration and validation of the 3Di model were based on absolute water level, high water level, low water level, tidal range, ebb duration, and flood duration. These indicators were derived from gauge stations in the channels and Aquadopp Profiler measurements on the intertidal flats. While flow velocities were not included in the calibration process, incorporating them in future efforts would improve the model's ability to represent dynamic system behaviour. Calibration reduced the average root mean square error (RMSE) for six different performance criteria from 0.34 to 0.25 across the domain, and from 0.35 to 0.20 for the eastern Wadden Sea gauge stations, corresponding to improvements of 26% and 43% respectively for the windless period. These improvements were achieved through model grid refinement and the application of two spatially distinct bottom roughness values. For a period with strong winds, calibration reduced the average RMSE from 0.33 to 0.29.

Although high water levels were underestimated, low water levels and tidal timing were accurately captured. The underestimation of high-water peaks may stem from the use of boundary conditions calibrated in another model or other model setup choices. Despite uncertainties in high water level predictions, the essential parameters for calibrating a hydrodynamic model are high/low water levels and flood and ebb durations to evaluate timing.

2. To what extent are flow patterns, exposure times, and areas significantly affected by variations in wind speed and direction spatially and temporally?

The effects of wind on exposure time and area depend on both wind strength and direction. Compared to the base case, the mean exposure time rises non-linearly under easterly winds, while it declines nearly linearly under westerly and northerly winds, which is a remarkable effect. In the strongest easterly scenario (East-9, $\approx$23 m s^{-1}), mean exposure time increases from 3.67 h to 5.51 h. In contrast, under equally strong northerly and westerly winds (North-9 and West-9), the average exposure time drops sharply to 0.95 h and 0.77 h, and total exposed area decreases by 70–82%. These trends indicate a nearly linear inundation response to increasing wind setup through the different scenarios from the north and west. At low wind speeds (1 Beaufort), changes remain minimal ($<$1%), confirming that modest winds exert little influence on exposure dynamics.

Significant changes in exposure time, ranging from 20–49% (2.6–6 h), occur under 6–9 Beaufort winds, particularly on higher tidal flats. Analysis of flow patterns during slack water and residual currents during full tidal cycles revealed that northerly and easterly winds induced net westward flow, whereas westerly winds caused eastward flow. From 3 Beaufort onward, the direction of the residual current on the flats changed. Easterly winds were especially influential, reversing flow direction at Aquadopp locations from 3 Beaufort and above. Westerly winds at 6 Beaufort produced the most pronounced residual flow compared to equivalent northerly or easterly winds. Overall, wind significantly amplified flow velocities over the intertidal flats, with the strongest increases observed under westerly winds.

3. What are the implications of varying wind conditions in terms of ecotope mapping?

Wind-driven changes in exposure time and changing flow patterns have clear implications for ecotope mapping. Although the results were observed over a single tidal cycle, they indicate that wind can cause shifts in the extent of the littoral zone under specific conditions. For example, longer exposure times caused by easterly winds increased the littoral zone by up to 4%. In contrast, prolonged submergence due to westerly and northerly winds can reduce the extent of exposed areas, potentially limiting the littoral zone.

These insights highlight the potential of using a (well-calibrated) hydrodynamic subgrid model in future ecotope mapping efforts, especially in shallow intertidal areas. Unlike the current method, which relies on interpolation between gauge stations, a hydrodynamic model like 3Di may offer a more detailed and physically consistent representation of flooding and drying processes. Although a direct comparison between modelling approaches was not conducted in this study, the enhanced spatial resolution and dynamic behaviour captured by subgrid models may provide a strong foundation for improving the accuracy and ecological relevance of inputs to ecotope mapping. Given the strong temporal variability in exposure times and flow patterns caused by wind, future research should assess the added value of a well-calibrated subgrid hydrodynamic model compared to the existing approach.

Concluding remarks

This research highlights the substantial and spatially nuanced role of wind in shaping hydrodynamic conditions on the Wadden Sea's intertidal flats. By linking variations in wind speed and direction to changes in residual flow and exposure patterns, the findings provide a better understanding of hydrodynamic-ecological interactions. Although the model does not perfectly replicate gauge observations of high water levels, it consistently captures the low water conditions and tidal timing required to assess relative scenario impacts. The use of a (well-calibrated) hydrodynamic subgrid model may offer a promising way forward for ecotope mapping.

8
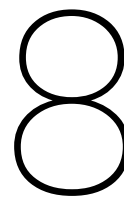
Recommendations

This study shows that wind direction and magnitude strongly influence exposure times, exposed areas, and residual flow on the Pinkewad flats. Future work should extend the calibrated model to cover neap–spring tides, include flow-velocity validation, and compute depth-averaged residual flows to better link hydrodynamics with sediment transport. Additionally, it is recommended to compute peak depth-averaged flow velocities and assess how residual velocity combined with local depth translates into flow rate, offering a stronger link between hydrodynamics and sediment transport processes.

It is recommended to calibrate and validate the model not only on water levels but also on flow velocities, which was outside the scope of this research. This would provide a more complete assessment of model performance, particularly in terms of capturing currents. Another recommendation is to deploy measurement instruments in shallow channels across the domain that remain continuously submerged. This allows for full application of the performance criteria used in this research, including tidal range, absolute water level, low water level, and ebb/flood durations.

To further investigate how flow patterns, exposure times, and exposed areas are affected by spatial and temporal variations in wind, it is advised to consider alternative boundary configurations. It would be valuable to investigate the use of model boundaries placed closer to the specific area of interest. Considering the deviating water levels along the western and southern boundaries, as described in Chapter 4, reducing the model domain and applying observed water levels at Den Helder could lead to improved boundary accuracy.

An even more promising option would be to configure the 3Di model without nested boundaries, using boundaries derived directly from gauge stations in the North Sea that are linked by spatial interpolation. This would remove dependence on an external model and may reduce inherited boundary anomalies. Furthermore, a comparison with the DCSM-model using the same patched roughness map would make it possible to evaluate the model results and to examine the influence of the western boundary on water levels at Den Helder within the DCSM-model. This approach could also improve the integration of different modelling systems through more effective boundary alignment.

Additionally, narrowing the wind spectrum and analysing more refined wind directions, such as southerly winds or those between the currently modelled scenarios, could help determine threshold values for changes in residual currents and exposed areas. This would contribute to a more detailed understanding of wind-driven effects on exposure times, flow patterns, and spatial anomalies across the domain.

Currently, exposure time maps used for ecotope mapping in the Wadden Sea are based on interpolated water level data from tide gauge stations using InterTides. For Rijkswaterstaat, it is recommended to also investigate the application of well-calibrated 2D depth-averaged hydrodynamic (subgrid) model outputs, converted to exposure time maps. This may reveal differences in the exposure maps, which would influence the classification of ecotopes.

Looking ahead, repeating model runs with regional climate-model wind ensembles will reveal whether favourable easterly storms are projected to decline or rebound, so the a calibrated model could be run to see what the implications are for the exposure times and flow patterns for future weather predictions.
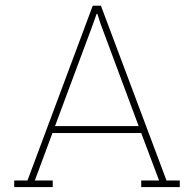
References

Baptist, M. J., van der Wal, J. T., Folmer, E. O., Gräwe, U., & Elschot, K. (2019). An ecotope map of the trilateral Wadden Sea. *Journal of Sea Research*, *152*. https://doi.org/10.1016/j.seares.2019.05.003

Bates, P. D. (2000). Development and testing of a subgrid-scale model for moving-boundary hydrodynamic problems in shallow water. *Hydrological Processes*, *14*(11-12), 2073–2088. https://doi.org/10.1002/1099-1085(20000815/30)14:11/12<2073::AID-HYP55>3.0.CO;2-X

Boorsma, R. (2024). *Tidally-and Wind-Driven Horizontal Flow Patterns on Intertidal Flats in the Wadden Sea An Assessment using Subgrid Modeling Technique* (tech. rep.).

Bosboom, J., & Stive, M. (2023, January). *Coastal Dynamics*. TU Delft OPEN Publishing. https://doi.org/10.5074/T.2021.001

Casulli, V. (2009). A high-resolution wetting and drying algorithm for free-surface hydrodynamics. *International Journal for Numerical Methods in Fluids*, *60*(4), 391–408. https://doi.org/10.1002/fld.1896

Chen, Z. L., & Lee, S. Y. (2022, May). Tidal Flats as a Significant Carbon Reservoir in Global Coastal Ecosystems. https://doi.org/10.3389/fmars.2022.900896

Christianen, M., van der Heide, T., Holthuijsen, S., van der Reijden, K., Borst, A., & Olff, H. (2017). Biodiversity and food web indicators of community recovery in intertidal shellfish reefs. *Biological Conservation*, *213*, 317–324. https://doi.org/10.1016/j.biocon.2016.09.028

Colosimo, I., de Vet, P. L., van Maren, D. S., Reniers, A. J., Winterwerp, J. C., & van Prooijen, B. C. (2020). The impact of wind on flow and sediment transport over intertidal flats. *Journal of Marine Science and Engineering*, *8*(11), 1–26. https://doi.org/10.3390/jmse8110910

Colosimo, I., van Maren, D. S., de Vet, P. L. M., Winterwerp, J. C., & van Prooijen, B. C. (2023). Winds of opportunity: The effects of wind on intertidal flat accretion. *Geomorphology*, *439*. https://doi.org/10.1016/j.geomorph.2023.108840

de Vet, P. L., van Prooijen, B. C., Colosimo, I., Steiner, N., Ysebaert, T., Herman, P. M., & Wang, Z. B. (2020). Variations in storm-induced bed level dynamics across intertidal flats. *Scientific Reports*, *10*(1). https://doi.org/10.1038/s41598-020-69444-7

de Vet, P. L., van Prooijen, B. C., Schrijvershof, R. A., van der Werf, J. J., Ysebaert, T., Schrijver, M. C., & Wang, Z. B. (2018). The Importance of Combined Tidal and Meteorological Forces for the Flow and Sediment Transport on Intertidal Shoals. *Journal of Geophysical Research: Earth Surface*, *123*(10), 2464–2480. https://doi.org/10.1029/2018JF004605

De Vet, P. L. M. (2020). Intertidal Flats in Engineered Estuaries On the Hydrodynamics, Morphodynamics, and Implications for Ecology and System Management. https://doi.org/10.4233/uuid:2b392951-3781-4aed-b093-547c70cc581d

Deltares. (2022). *Dcsm-fm 100m: A sixth-generation model for the nw european shelf — 2022 release* (tech. rep.) (Accessed: 2025-04-14). Deltares. https://www.deltares.nl/expertise/publicaties/dcsm-fm-100m-a-sixth-generation-model-for-the-nw-european-shelf-2022-release

Deltares. (2024). *Delft3D-FLOW User Manual* [Version 2024.02, accessed July 2, 2025]. Deltares. https://content.oss.deltares.nl/delft3d4/Delft3D-FLOW_User_Manual.pdf

Deltares. (n.d.). Faq metingen en scenario's zeespiegelstijging [accessed June 18, 2025]. *Deltares*.

Duran-Matute, M., Gerkema, T., De Boer, G. J., Nauw, J. J., & Gräwe, U. (2014). Residual circulation and freshwater transport in the Dutch Wadden Sea: A numerical modelling study. *Ocean Science*, *10*(4), 611–632. https://doi.org/10.5194/os-10-611-2014

Duran-Matute, M., Gerkema, T., & Sassi, M. G. (2016). Quantifying the residual volume transport through a multiple-inlet system in response to wind forcing: The case of the western Dutch Wadden Sea. *Journal of Geophysical Research: Oceans*, *121*(12), 8888–8903. https://doi.org/10.1002/2016JC011807

French, J. R. (2008). Hydrodynamic Modelling of Estuarine Flood Defence Realignment as an Adaptive Management Response to Sea-Level Rise. *Journal of Coastal Research*, *2*, 1–12. https://doi.org/10.2112/05-0534.1

Friedrichs, C. T., & Aubrey, D. G. (1988). *Non-linear Tidal Distortion in Shallow Well-mixed Estuaries: a Synthesisa* (tech. rep.).

Gong, W., Schuttelaars, H., & Zhang, H. (2016). Tidal asymmetry in a funnel-shaped estuary with mixed semidiurnal tides. *Ocean Dynamics*, *66*(5), 637–658. https://doi.org/10.1007/s10236-016-0943-1

Gräwe, U., Flöser, G., Gerkema, T., Duran-Matute, M., Badewien, T. H., Schulz, E., & Burchard, H. (2016). A numerical model for the entire Wadden Sea: Skill assessment and analysis of hydrodynamics. *Journal of Geophysical Research: Oceans*, *121*(7), 5231–5251. https://doi.org/10.1002/2016JC011655

Heip, C., Goosen, N., Herman, P., Kromkamp, J., Middelburg, J., & Soetaert, K. (1995). Production and consumption of biogenic particles in temperate tidal estuaries. *Oceanography and Marine Biology: an annual review. Vol. 33*, *33*.

Hope, J. A., Paterson, D. M., & Thrush, S. F. (2020, May). The role of microphytobenthos in soft-sediment ecological networks and their contribution to the delivery of multiple ecosystem services. https://doi.org/10.1111/1365-2745.13322

Horn, S., Schwemmer, P., Mercker, M., Enners, L., Asmus, R., Garthe, S., & Asmus, H. (2020). Species composition of foraging birds in association with benthic fauna in four intertidal habitats of the Wadden Sea. *Estuarine, Coastal and Shelf Science*, *233*, 106537. https://doi.org/10.1016/j.ecss.2019.106537

Jansen, S., Walpersdorf, E., Werner, U., Billerbeck, M., Böttcher, M. E., & de Beer, D. (2009). Functioning of intertidal flats inferred from temporal and spatial dynamics of O2, H2S and pH in their surface sediment. *Ocean Dynamics*, *59*(2), 317–332. https://doi.org/10.1007/s10236-009-0179-4

K. Korporaal. (2024, October). *Structuring the hydrodynamics of the Elbe estuary* (tech. rep.). University of Twente.

Laursen, K., Beusekom, J. E. v., Bregnballe, T., Kleefstra, R., Frikke, J., Günther, K., Hälterlein, B., Hornman, M., Ludwig, J., Meyer, J., Scheiffarth, G., Pedersen, C. L., & Møller, A. P. (2024). Climate and de-eutrophication affect abundance of benthos-feeding waterbirds in the Wadden Sea during stop-over. https://doi.org/10.21203/rs.3.rs-3716982/v1

Lu, S., Tong, C., Lee, D.-Y., Zheng, J., Shen, J., Zhang, W., & Yan, Y. (2015). Propagation of tidal waves up in <scp>Y</scp> angtze <scp>E</scp> stuary during the dry season. *Journal of Geophysical Research: Oceans*, *120*(9), 6445–6473. https://doi.org/10.1002/2014JC010414

Nauw, J., Philippart, C. J., Duran-Matute, M., & Gerkema, T. (2017). Estimates of exposure times in the Wadden Sea: A comparison of methods. *Journal of Sea Research*, *127*, 12–25. https://doi.org/10.1016/j.seares.2017.03.015

Nelen & Schuurmans. (2024). *3di documentation* [Accessed: 2025-06-23]. https://docs.3di.live/index.html

Nidzieko, N. J., & Ralston, D. K. (2012). Tidal asymmetry and velocity skew over tidal flats and shallow channels within a macrotidal river delta. *Journal of Geophysical Research: Oceans*, *117*(C3). https://doi.org/10.1029/2011JC007384

Oost, A. P., Hofstede, J., Weisse, R., Baart, F., Janssen, G., & Zijlstra, R. (2017). Wadden Sea Quality Status Report Climate change Wadden Sea Quality Status Report-Climate change 2. https://doi.org/10.5281/zenodo.15130584

Paree, A., Kers, A. S., Jentink, R., Hendriks, J.-R., & Baptist, M. J. (2017). *Toelichting op de zoute ecotopenkaart Waddenzee 2017* (tech. rep.).

Pearson, S. G. (2022). Sediment Pathways on Ebb-Tidal Deltas New Tools and Techniques for Analysis. https://doi.org/10.4233/uuid:c2fe811c-dc2e-4e1f-bb0c-dc43f11cd1eb

Postma, H. (2025, April). "vogels op het wad" [Accessed via "Doel: Samenwerken aan ruimte voor wadvogels en mensen" page, Waddenvereniging]. https://waddenvereniging.nl/verschil-maken/wadvogels/

Reise, K., Baptist, M., Burbridge, P., Dankers, N., Fischer, L., Flemming, B., Oost, A., & Smit, C. (2010). The wadden sea a universally outstanding tidal wetland. *Wadden Sea Ecosystem*, *29*, 7–24.

Ricklefs, K., Franken, O., Glorius, S., Mascioli, F., Nielsen, P., Reimers, H.-C., & Trampe, A. (2022). *Wadden Sea Quality Status Report Subtidal habitats* (tech. rep.).

Rijkswaterstaat. (2023a). *Toelichting op de zoute ecotopenkaart waddenzee: Eierlandse en amelander zeegat* (tech. rep.) (Versie oktober 2023). Ministerie van Infrastructuur en Waterstaat, Rijkswaterstaat. Nederland. https://open.rijkswaterstaat.nl/@285052/toelichting-zoute-ecotopenkaart/

Rijkswaterstaat. (2023b). Vaklodingen bathymetry request page [[Dataset]].

Sehili, A., Lang, G., & Lippert, C. (2014). High-resolution subgrid models: Background, grid generation, and implementation. *Ocean Dynamics*, *64*(4), 519–535. https://doi.org/10.1007/s10236-014-0693-x

Stelling, G. S. (2012). Quadtree flood simulations with sub-grid digital elevation models. *Proceedings of the Institution of Civil Engineers - Water Management*, *165*(10), 567–580. https://doi.org/10.1680/wama.12.00018

Stelling, G. S. (2022). Boosted robustness of semi-implicit subgrid methods for shallow water flash floods in hills. *Computers & Fluids*, *247*, 105645. https://doi.org/10.1016/j.compfluid.2022.105645

Sterl, A., M R Bakker, A., Brink, H. W. v. d., Haarsma, R., Stepek, A., Wijnant, I. L., & Winter, R. C. d. (2015). Large-scale winds in the southern North Sea region: the wind part of the KNMI'14 climate change scenarios. *Environmental Research Letters*, *10*(3), 035004. https://doi.org/10.1088/1748-9326/10/3/035004

UNESCO. (2009). https://whc.unesco.org/en/list/1314/

van Rijn, L. (2017). *Note: Deposition/dredging of tidal ferry channel in Dutch Wadden Sea* (tech. rep.). www.leovanrijn-sediment.com

van Weerdenburg, R. (2021). *Modelparameters Ecotopenkaart Waddenzee 2021* (tech. rep.).

van Weerdenburg, R., Pearson, S., van Prooijen, B., Laan, S., Elias, E., Tonnon, P. K., & Wang, Z. B. (2021). Field measurements and numerical modelling of wind-driven exchange flows in a tidal inlet system in the Dutch Wadden Sea. *Ocean and Coastal Management*, *215*. https://doi.org/10.1016/j.ocecoaman.2021.105941

Van Goor, M. A., Zitman, T. J., Wang, Z. B., & Stive, M. J. (2003). Impact of sea-level rise on the morphological equilibrium state of tidal inlets. *Marine Geology*, *202*(3-4), 211–227. https://doi.org/10.1016/S0025-3227(03)00262-7

Van Weerdernburg R & Hanssen J. (2023). *Modellering van droogvalduur in de Waddenzee met D-Flow FM* (tech. rep.).

Volp, N. (2017). Subgrid is Dancing with Sediment A Full Subgrid Approach for Morphodynamic Modelling. https://doi.org/10.4233/uuid:271c4360-e242-42aa-8974-72fe012365ee

Volp, van Prooijen, B. C., Pietrzak, J. D., & Stelling, G. S. (2016). A subgrid based approach for morphodynamic modelling. *Advances in Water Resources*, *93*, 105–117. https://doi.org/10.1016/j.advwatres.2015.07.013

Volp, Van Prooijen, B. C., & Stelling, G. S. (2013). A finite volume approach for shallow water flow accounting for high-resolution bathymetry and roughness data. *Water Resources Research*, *49*(7), 4126–4135. https://doi.org/10.1002/wrcr.20324

Vroom, J., van Weerdenburg, R., Smits, B. P., & Herman, P. (2020). *Modellering slibdynamiek voor de waddenzee* (tech. rep.). Deltares.

Waddenvereniging. (n.d.). https://waddenvereniging.nl/verschilmaken-wereldbelang-werelderfgoed/

Waddenvereniging. (2022, September). Luchtfoto wadplaat zwarte haan [Photograph of the tidal flat "Zwarte Haan"]. https://waddenvereniging.nl/wp-content/uploads/2022/09/18981-luchtfoto-wadplaat-zwarte-haan-hp-1920x800.jpg

Wang, Z. B., Hoekstra, P., Burchard, H., Ridderinkhof, H., De Swart, H. E., & Stive, M. J. (2012). Morphodynamics of the Wadden Sea and its barrier island system. *Ocean and Coastal Management*, *68*, 39–57. https://doi.org/10.1016/j.ocecoaman.2011.12.022

Yin, K., Xu, S., & Huang, W. (2016). Modeling sediment concentration and transport induced by storm surge in Hengmen Eastern Access Channel. *Natural Hazards*, *82*(1), 617–642. https://doi.org/10.1007/s11069-016-2200-9

Zijl, F., Veenstra, J., & Groenenboom, J. (2018). *The 3d dutch continental shelf model - flexible mesh (3d dcsm-fm): Setup and validation* (tech. rep. No. Report 1220339-000-ZKS-0042). Deltares.

A

Examples of other numerical models

| Model	Characteristics	Advantages	Disadvantages
Delft3D	(Un)structured-grid hydrodynamic model; modules for sediment transport, morphology, and water quality.	• Proven reliability with extensive validation. • Structured and unstructured grid possible, using flexible mesh (FM). • Widely used in coastal and estuarine modeling.	• No live-view for first impression (compared to 3Di). • Computationally intensive for high-resolution simulations. • Licensing costs for some modules.
3Di	Structured-grid model; subgrid technique for high-resolution simulations; real-time interactive simulations; water quality.	• High spatial resolution through subgrid modeling. • Real-time simulation capabilities. • Efficient cloud-based computing. • GIS-based model setup.	• Subscription-based licensing. • Internet dependency for cloud operations. • Learning curve for new users.
TELEMAC	Open-source suite with unstructured mesh; modules for hydrodynamics, sediment transport, and wave dynamics.	• Completely open-source and customizable. • Unstructured mesh allows for detailed bathymetric representation. • Active international user community.	• Steep learning curve for non-experts. • Limited integrated GUI; often requires third-party tools for pre- and post-processing. • Computationally intensive.
MIKE FM	Flexible mesh model supporting unstructured grids; includes modules for hydrodynamics, waves, and sediment transport.	• High flexibility with unstructured grids. • Efficient for modelling complex coastal and estuarine systems. • Strong graphical user interface.	• Licensing costs may be prohibitive. • High computational requirements for large-scale or high-resolution models. • Proprietary software limits customization.

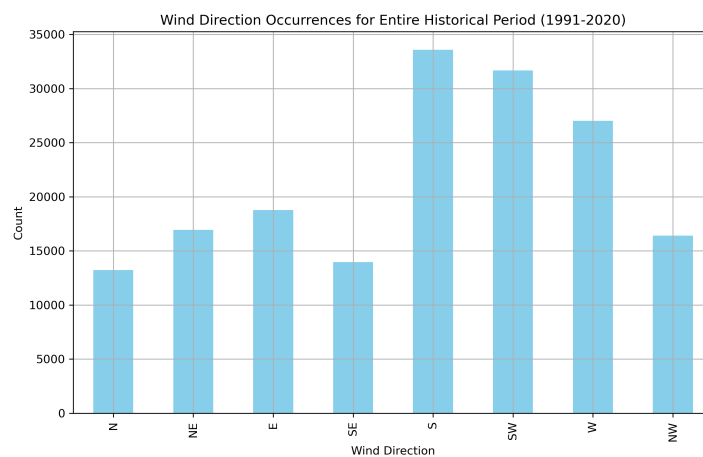**Table A.1:** Comparison of hydrodynamic models: Delft3D, 3Di, TELEMAC, and MIKE FM.

B

Wind histograms
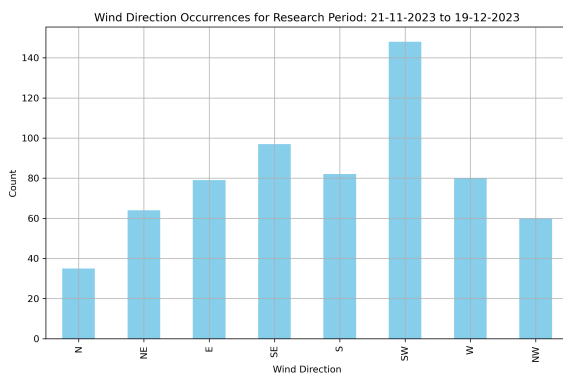
Figure B.1: Wind occurrences per direction for research period data points per hour.
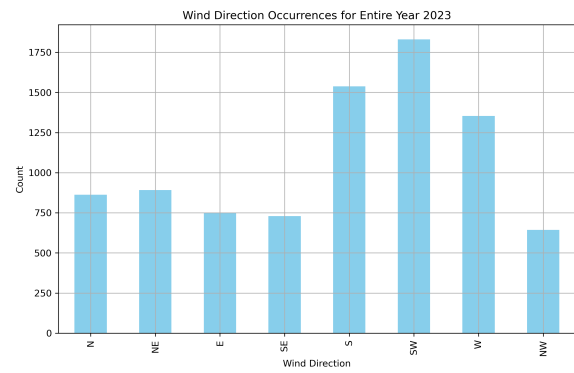
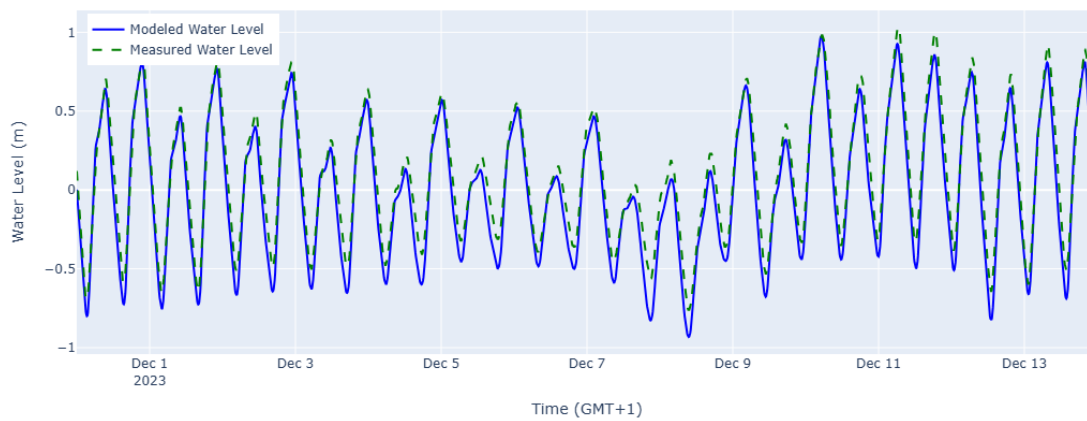**Figure B.2:** Wind occurrences per direction for 2023, data points per hour.

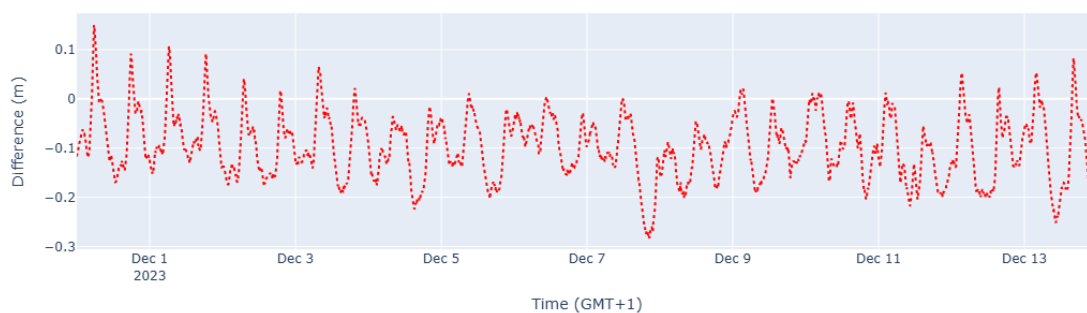**Figure B.3:** Wind occurences per direction for 1991-2021, data points per hour.

C

Boundary conditions

Water Levels at bc_west_045 (2023-11-30 to 2023-12-14)

Difference at bc_west_045 (2023-11-30 to 2023-12-14)

Figure C.1: Comparison between model boundary point BC_West_45 and RWS measuring platform K14 from November 30 to December 14, 2023. Top: water levels; bottom: water level difference (modeled minus measured). The difference resulted in a RMSE of 0.118m for this period.
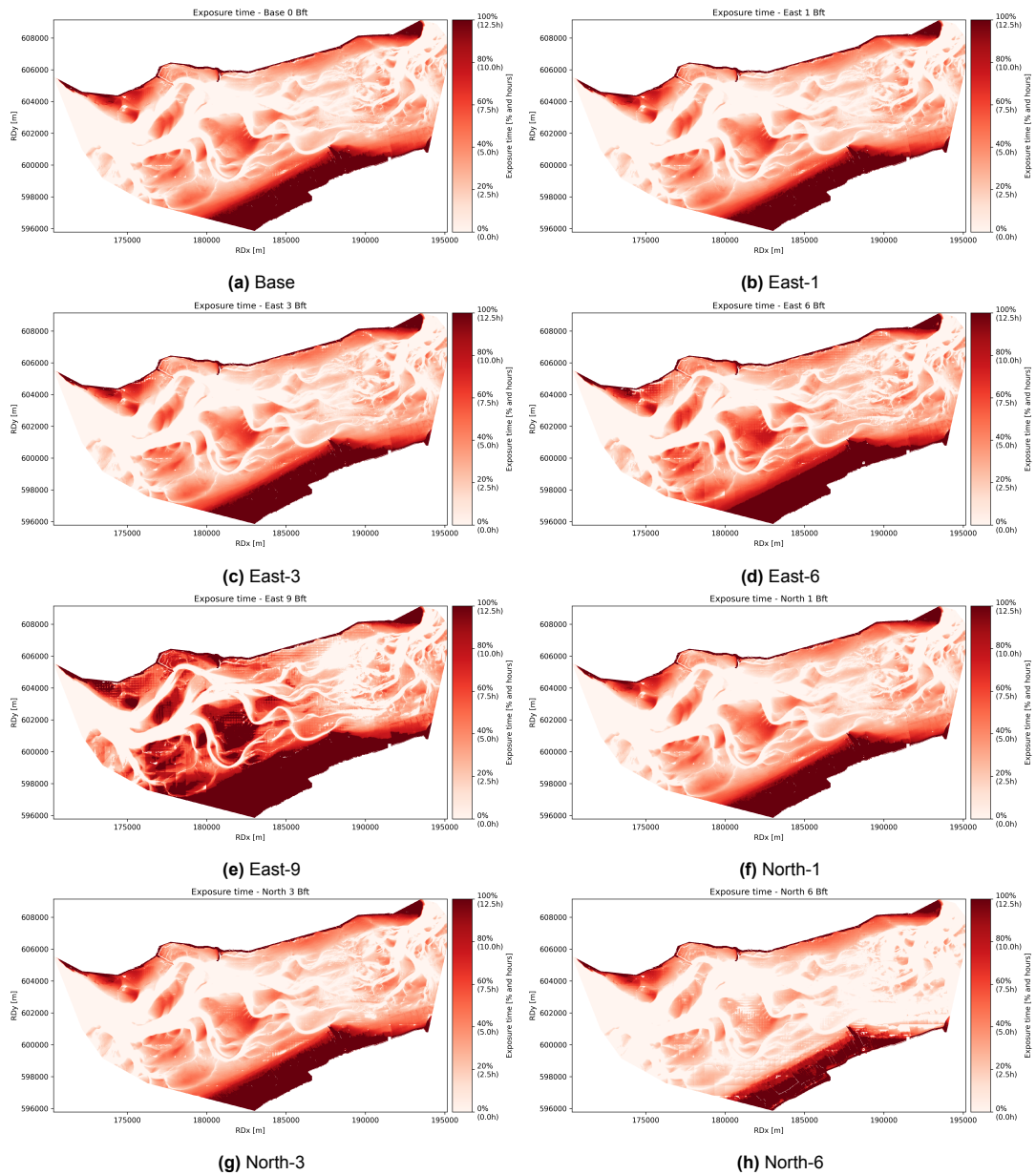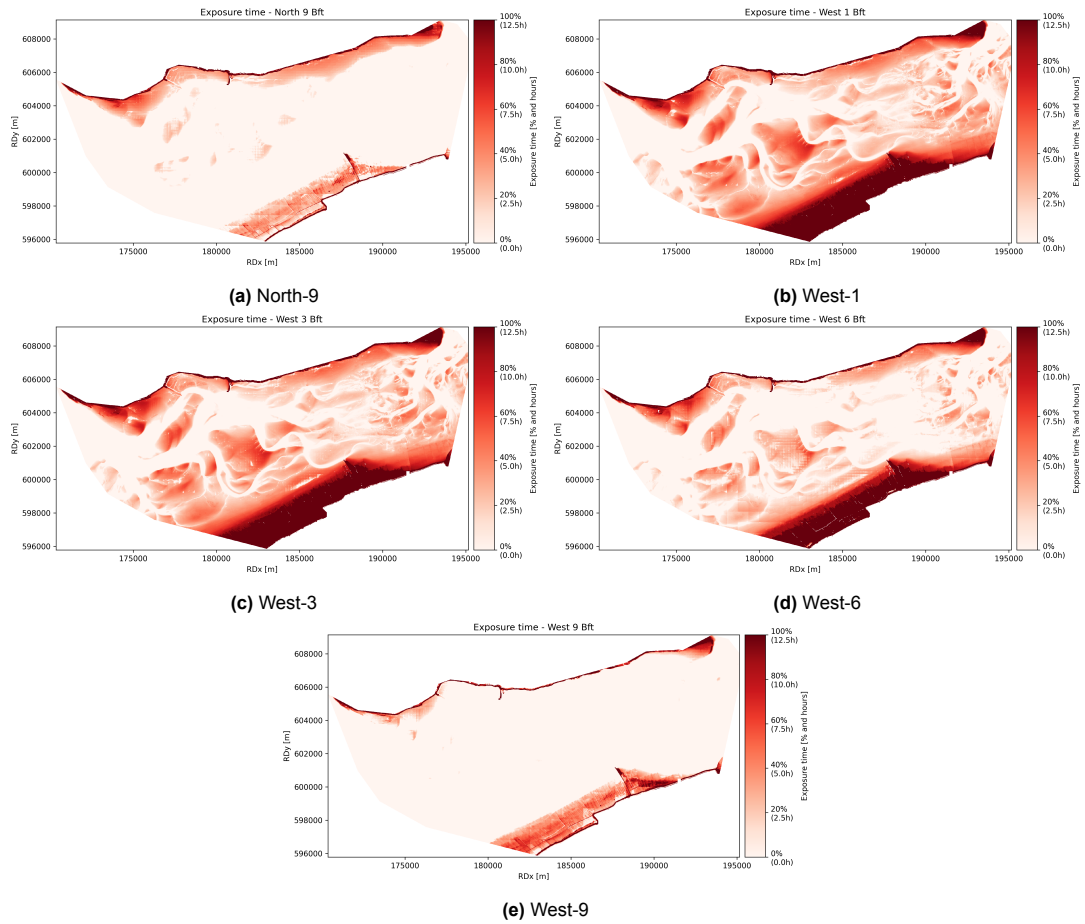
D

Exposure times

(a) Base

(b) East-1

(c) East-3

(d) East-6

(e) East-9

(f) North-1

(g) North-3

(h) North-6

Figure D.1: Exposure time maps (Set 1 of 2)

(a) North-9

(b) West-1

(c) West-3

(d) West-6

(e) West-9

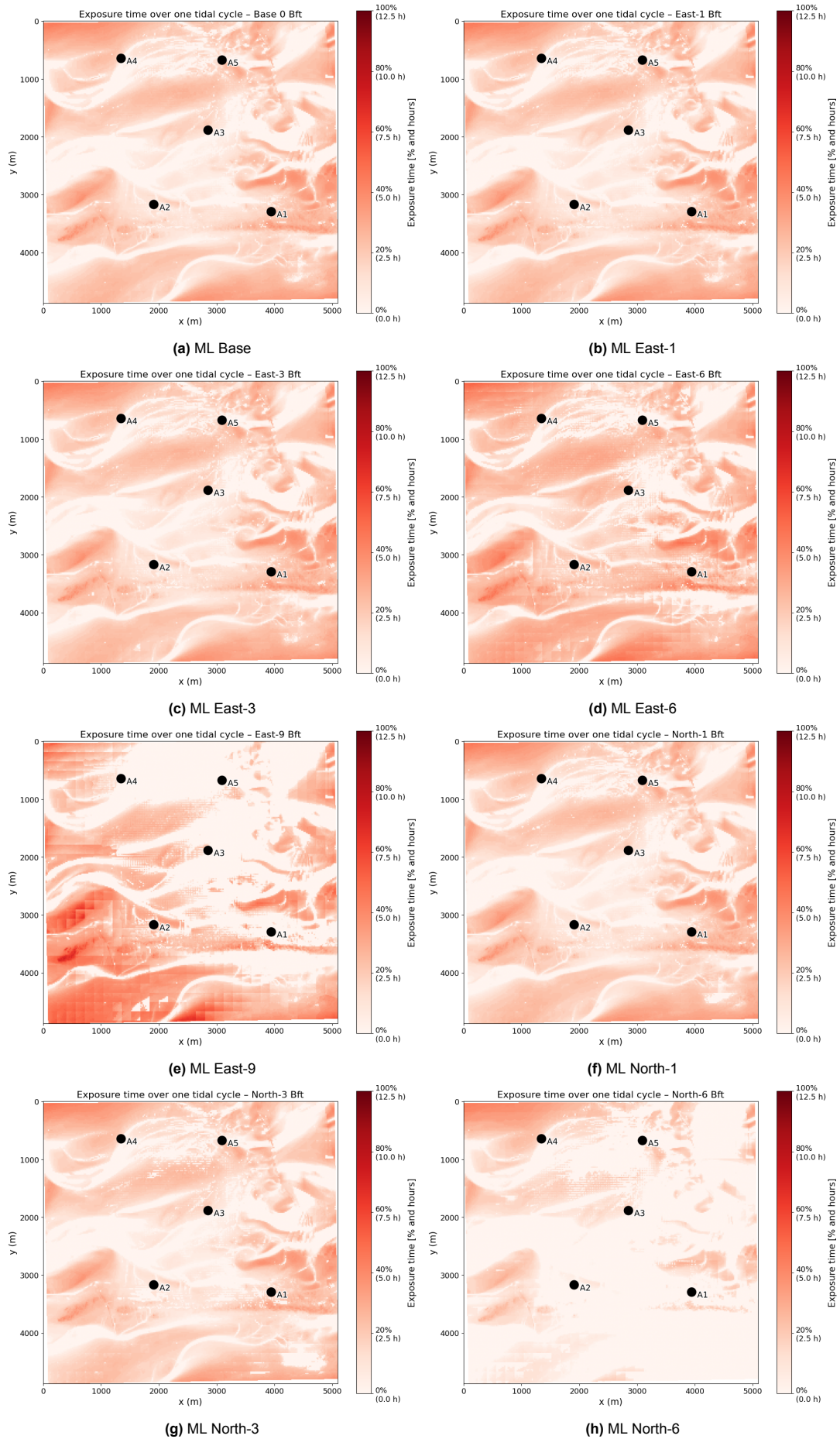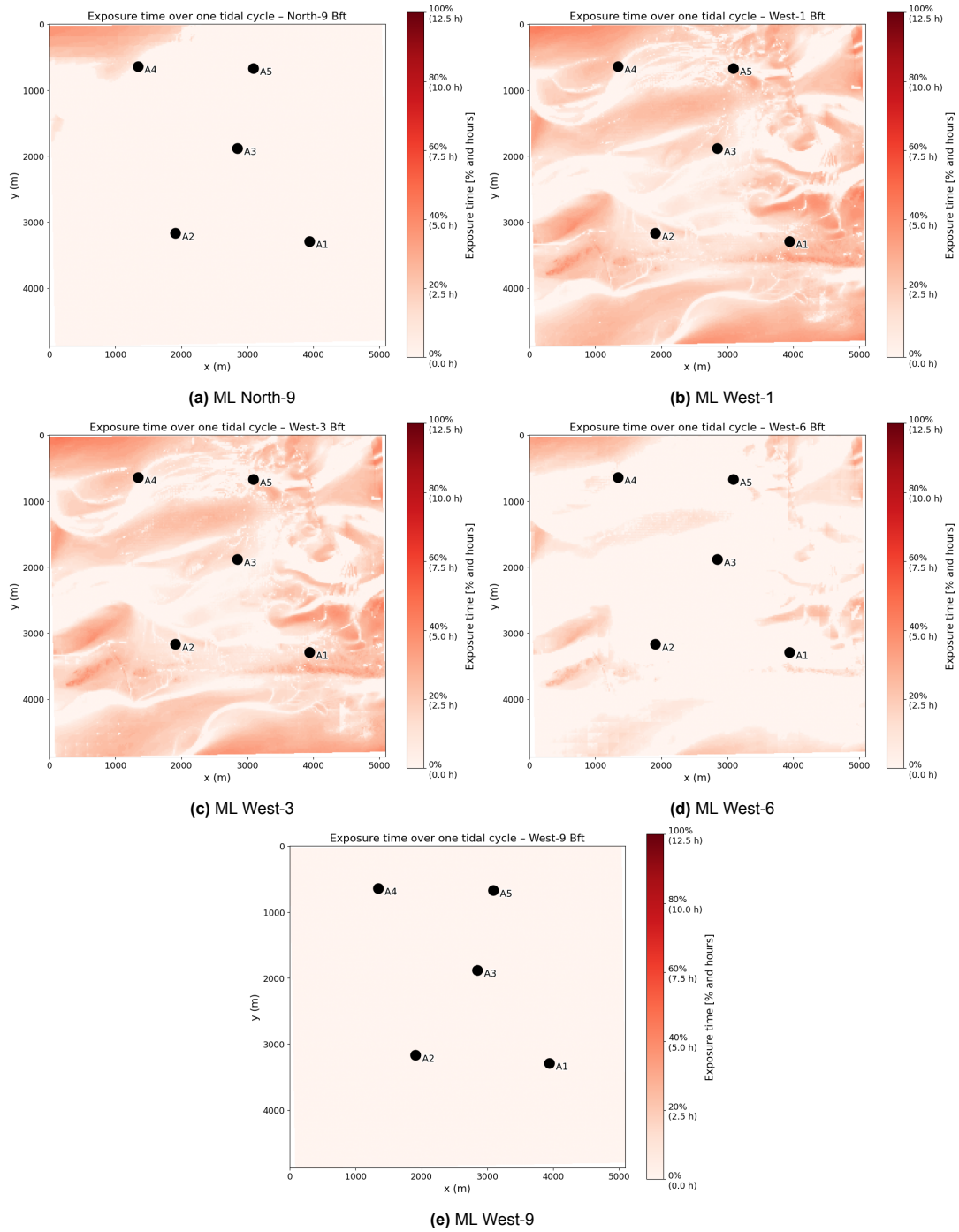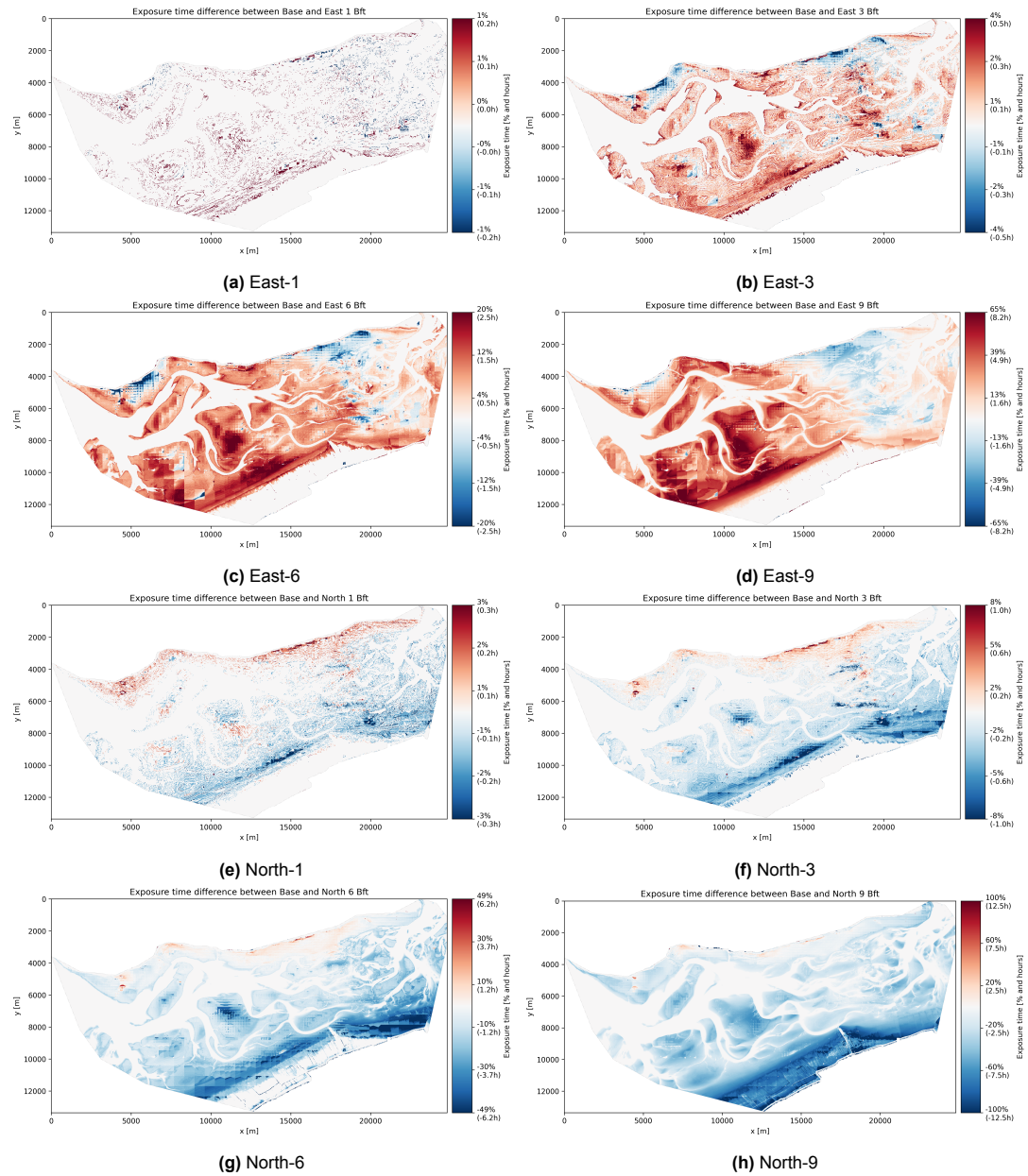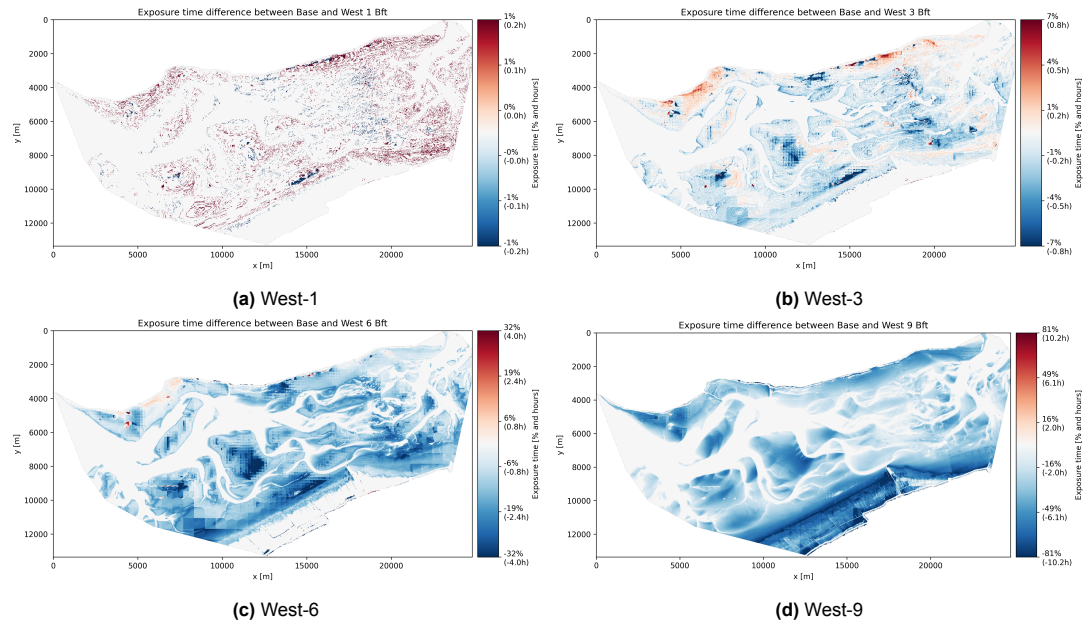**Figure D.2:** Exposure time maps (Set 2 of 2)

Figure D.3: Exposure maps at measurement locations (ML), (Set 1 of 2)

Figure D.4: Exposure maps at measurement locations (ML), (Set 2 of 2)

(a) East-1

(b) East-3

(c) East-6

(d) East-9

(e) North-1

(f) North-3

(g) North-6

(h) North-9

Figure D.5: Absolute exposure time differences (Set 1 of 2)

(a) West-1

(b) West-3

(c) West-6

(d) West-9

Figure D.6: Absolute exposure time differences (Set 2 of 2)

(a) East-1

(b) East-3

(c) East-6

(d) East-9

(e) North-1

(f) North-3

(g) North-6

(h) North-9
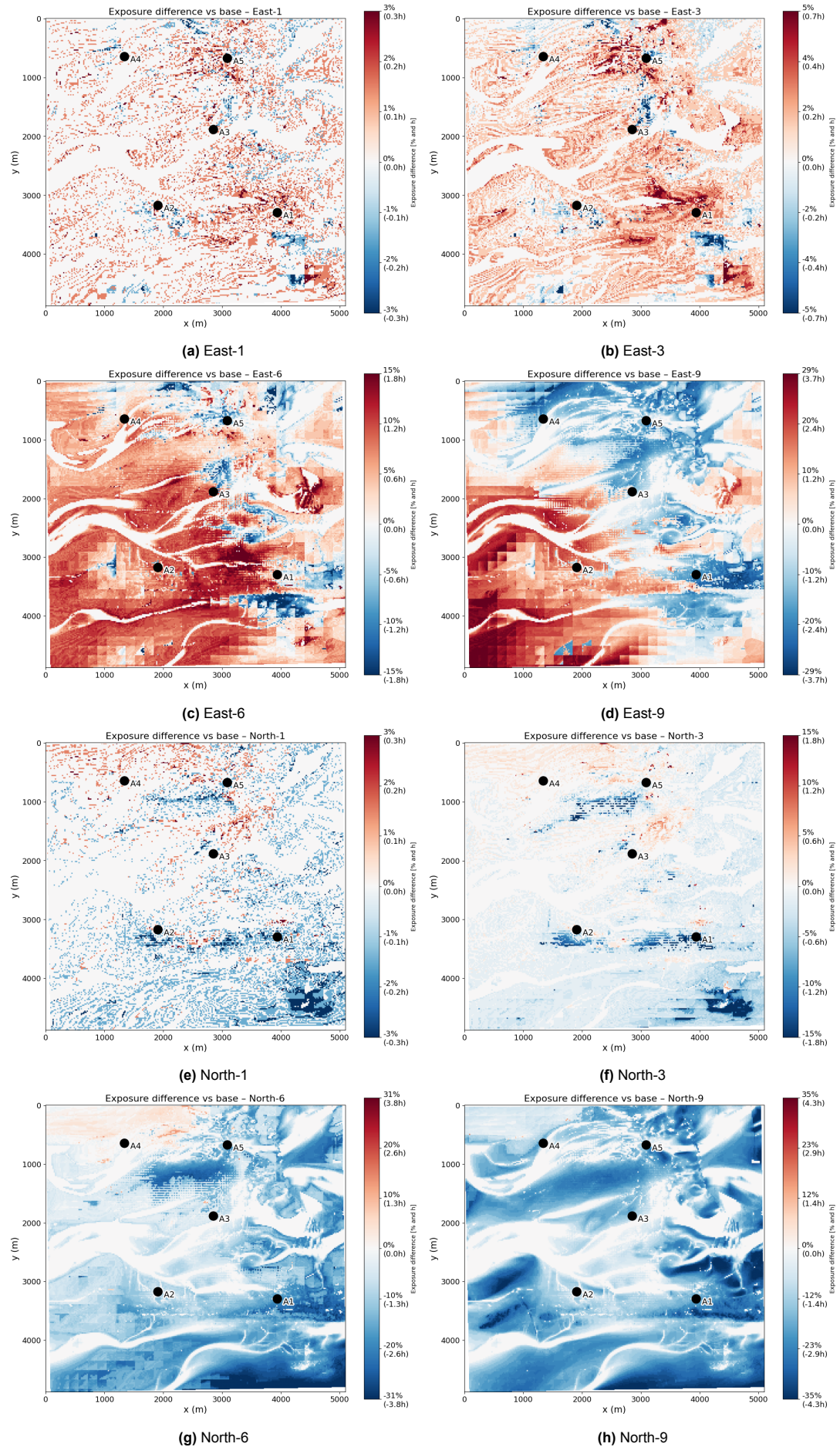
Figure D.7: Exposure time differences for easterly and northerly wind scenarios (Set 1 of 2)

(a) West-1

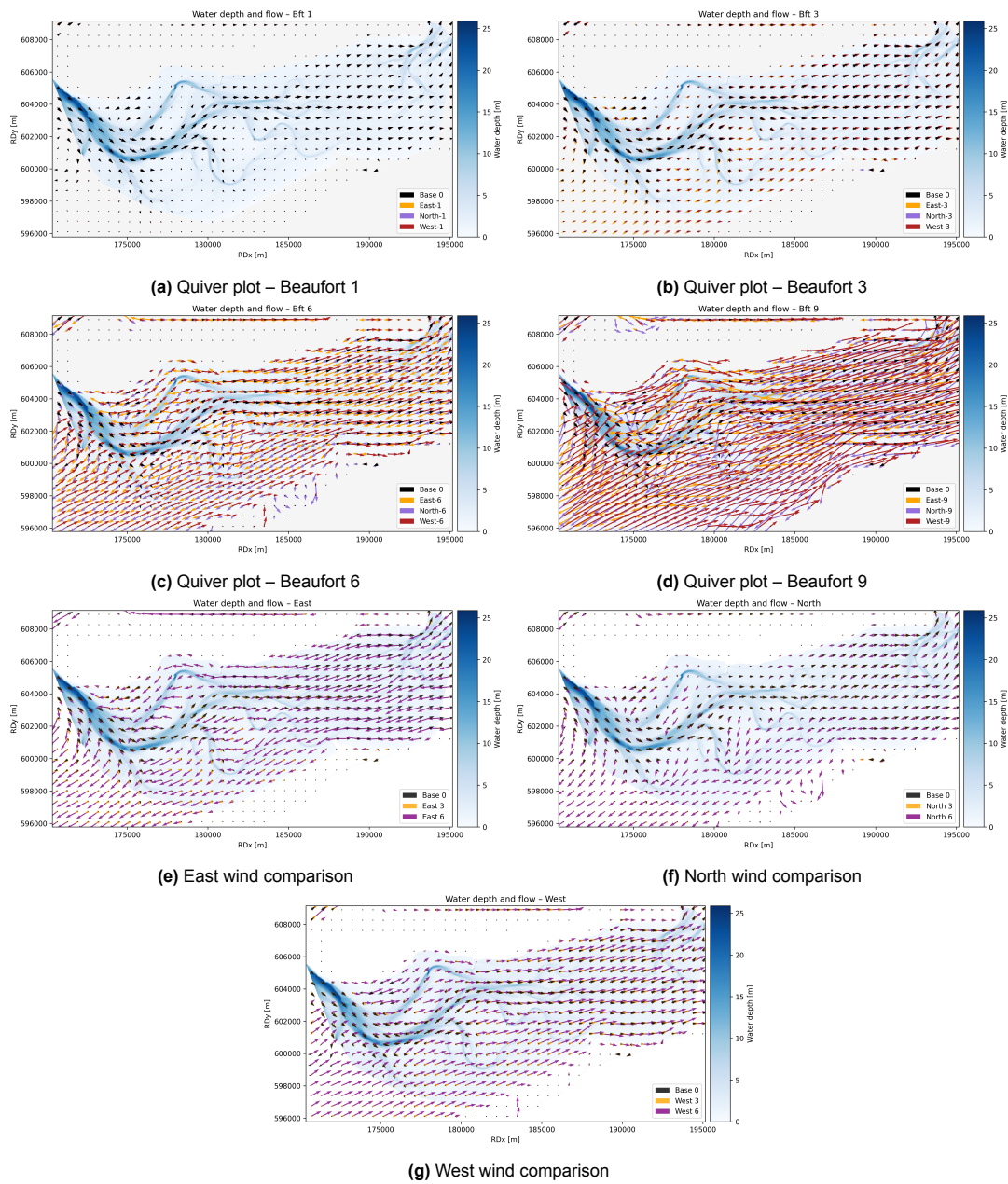**(b)** West-3

(c) West-6%

(d) West-9%
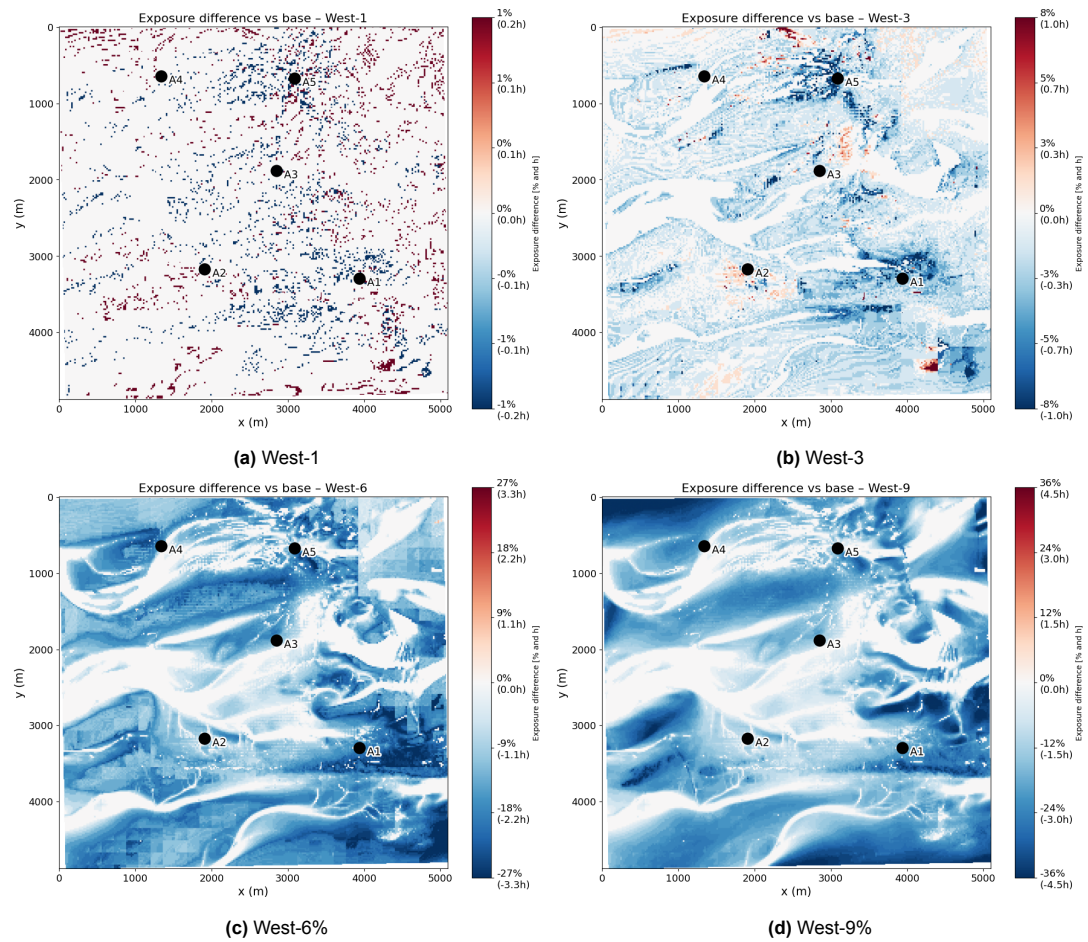
Figure D.8: Percentage exposure time differences for westerly wind scenarios (Set 2 of 2)

E

Quiver plots

(a) Quiver plot – Beaufort 1

(b) Quiver plot – Beaufort 3

(c) Quiver plot – Beaufort 6

(d) Quiver plot – Beaufort 9

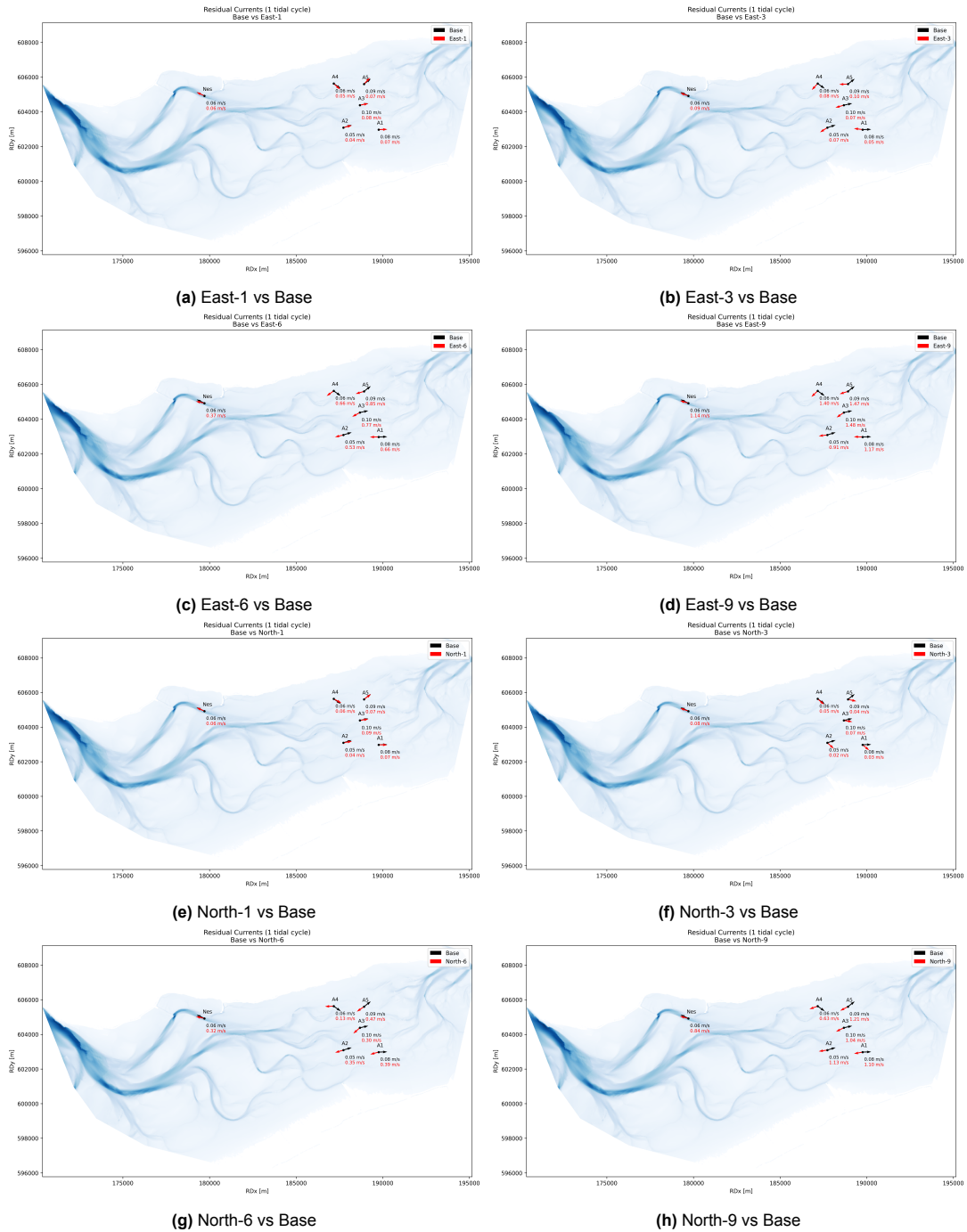**(e)** East wind comparison

(f) North wind comparison

(g) West wind comparison

Figure E.1: Quiver plot comparisons by wind force and direction

(a) East-1 vs Base

(b) East-3 vs Base

(c) East-6 vs Base

(d) East-9 vs Base

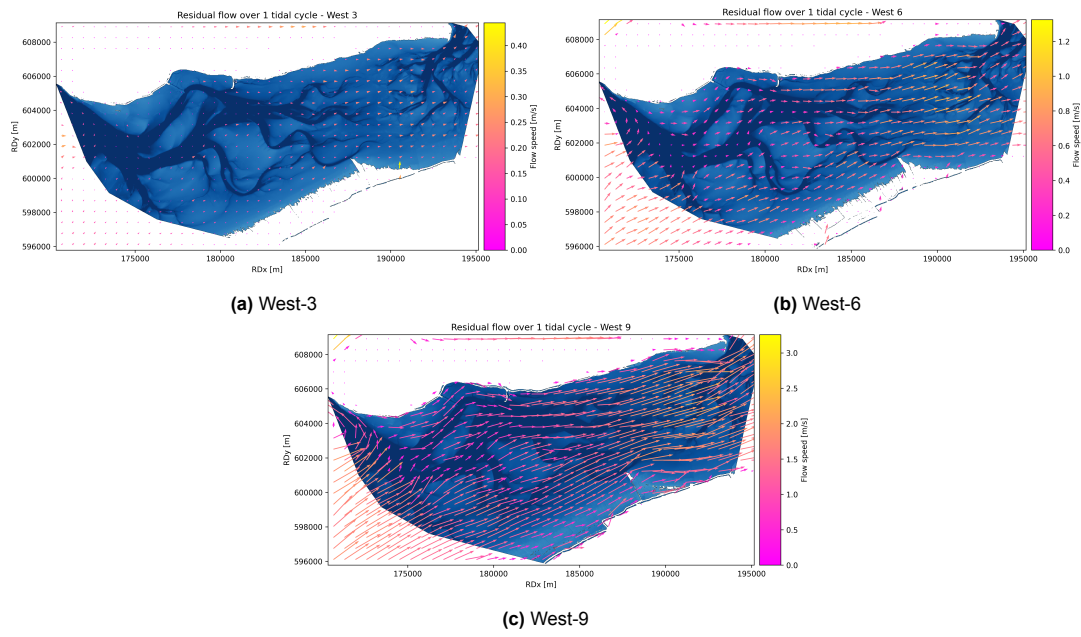**(e)** North-1 vs Base

(f) North-3 vs Base

(g) North-6 vs Base

(h) North-9 vs Base

Figure E.2: Residual flow comparison at fixed locations for easterly and northerly winds (Set 1 of 2)

(a) West-1 vs Base

(b) West-3 vs Base

(c) West-6 vs Base

(d) West-9 vs Base
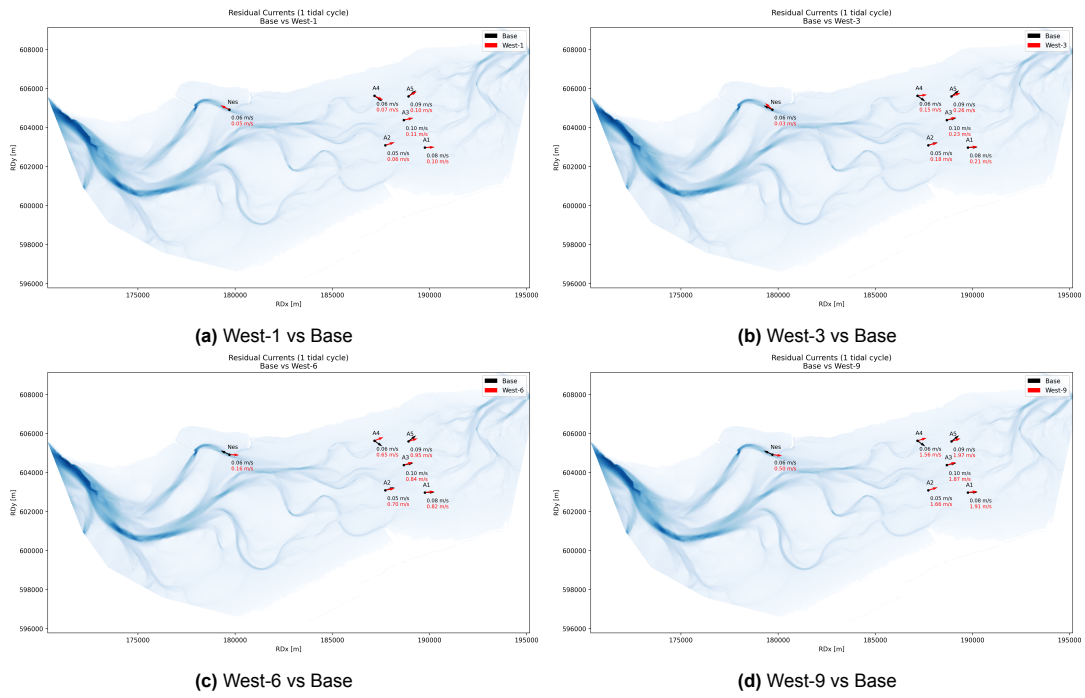
Figure E.3: Residual flow comparison at fixed locations for westerly winds (Set 2 of 2)

(a) Base Case

(b) East-1

(c) East-3

(d) East-6

(e) East-9

(f) North-1

(g) North-3

(h) North-6

(i) North-9

(j) West-1
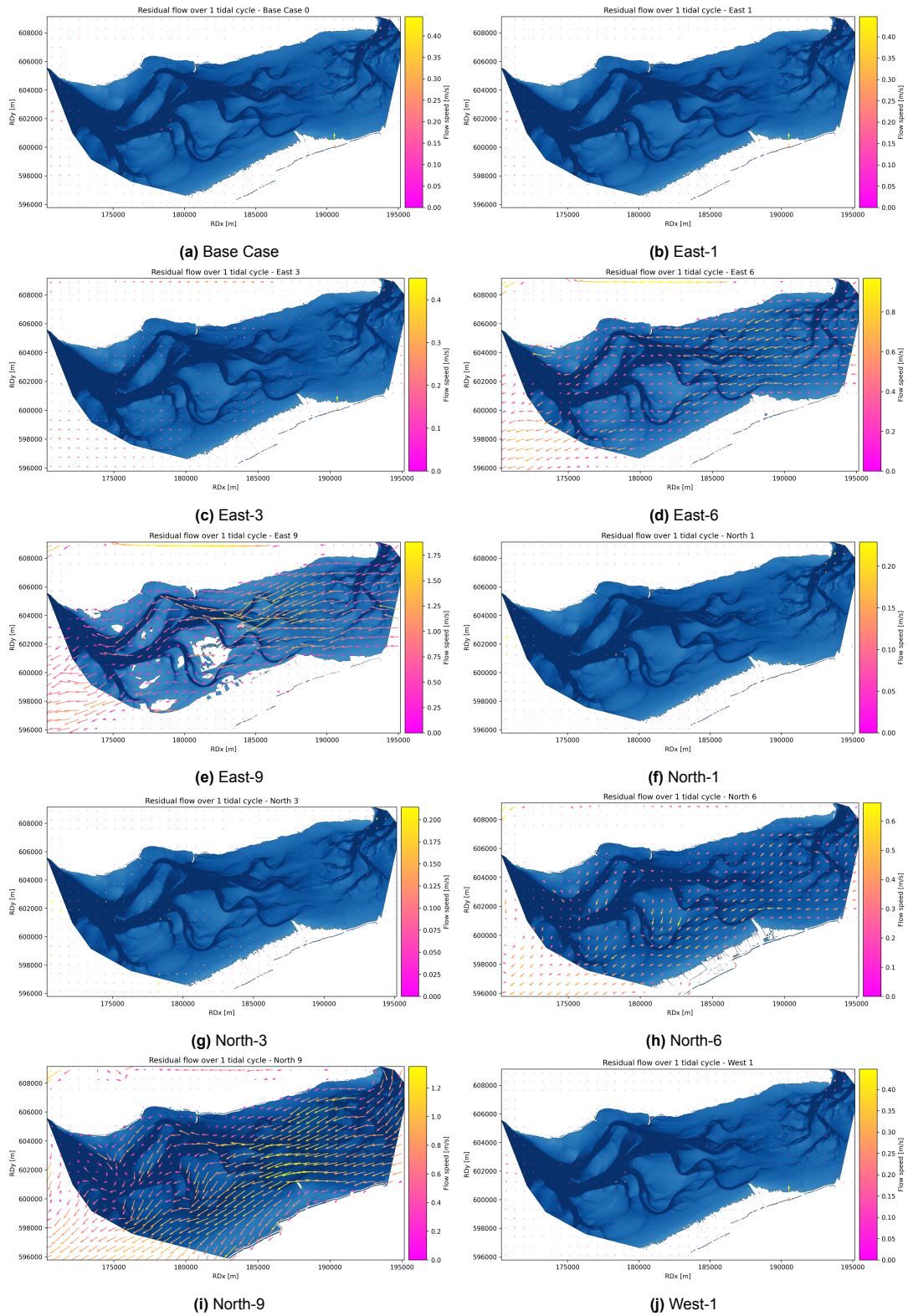
Figure E.4: Residual flow quiver plots (Set 1 of 2)

(a) West-3

(b) West-6

(c) West-9

Figure E.5: Residual flow quiver plots (Set 2 of 2)